COMPUTATION OF HIGH-SPEED REACTING FLOWS

By

JAMES KEITH CLUTTER

A DISSERTATION PRESENTED TO THE GRADUATE SCHOOL
OF THE UNIVERSITY OF FLORIDA IN PARTIAL FULFILLMENT
OF THE REQUIREMENTS FOR THE DEGREE OF
DOCTOR OF PHILOSOPHY

UNIVERSITY OF FLORIDA

1997

To my wife, Paula

My family has provided endless support whether it be emotional or dropping in to help with the kids during times of peak studying and work. I can not thank my mom and my mother-in-law enough as well as my father-in-law, Richard Cooper, who recently passed away. I must thank my father, the eternal student and consummate mechanic, for instilling in me a desire to learn how things work and the moxie to take them apart. My children, Courtney and Cooper, are without a doubt the finest children in the world and have been immensely understanding and patient. They have also proven to be delightful distractions and have helped keep me focused on what is truly important.

Finally, there is my wife, Paula, whose strength and encouragement are immeasurable. She has never ceased to support me whether it meant her understanding in me quitting my job to return to school or balancing her career and graduate school along with mine. I will never be able to express all she means to me.

TABLE OF CONTENTS

Abstract of Dissertation Presented to the Graduate School
of the University of Florida in Partial Fulfillment of the
Requirements for the Degree of Doctor of Philosophy

COMPUTATION OF HIGH-SPEED REACTING FLOWS

By

JAMES KEITH CLUTTER

May 1997

Chairperson: Dr. Wei Shyy
Major Department: Aerospace Engineering, Mechanics and Engineering Science

A computational study has been conducted for high-speed reacting flows relevant to munition problems, including shock-induced combustion and gun muzzle blast. The theoretical model considers inviscid and viscous flows, multi-species, finite rate chemical reaction schemes, and turbulence. Both the physical and numerical aspects are investigated to determine their impact on simulation accuracy.

A range of hydrogen and oxygen reaction mechanisms are evaluated for the shock-induced combustion flow scenario. Characteristics of the mechanisms such as the induction time, heat release rate, and second explosion limit are found to impact the accuracy of the computation. On the numerical side, reaction source term treatments, including logarithmic weighting and scaling modifications, are investigated to determine their effectiveness in addressing numerical errors caused by disparate length scales between chemical reactions and fluid dynamics. It is demonstrated that these techniques can enhance solution accuracy.

Computations of shock-induced combustion have also been performed using a k-ε model to account for the turbulent transport of species and heat. An algebraic model of the temperature fluctuations has been used to estimate the impact of the turbulent effect on the chemical reaction source terms. The turbulence effects when represented with the current models are found to be minimal in the shock-induced combustion flow investigated in the present work.

For the gun system simulations, computations for both a large caliber howitzer and small caliber firearms are carried out. A reduced kinetic scheme and an algebraic turbulence model are employed. The present approach, which accounts for the chemical reaction aspects of the gun muzzle blast problem, is found to improve the prediction of peak overpressures and can capture the effects produced by small caliber firearm sound suppressors.

The present study has established the numerical and physical requirements for simulating high-speed reacting flows. Also, key parameters useful in quantifying the roles of these aspects have been assessed.

CHAPTER 1
INTRODUCTION

In the present work, a computational capability is developed to analyze high speed reacting flows arising in munition problems. The particular problems focused on are a munition concept and the occurrence of gun muzzle blast. These problems are difficult to analyze given the fact many physical and chemical processes are involved. First a description of each problem is presented to highlight these various processes and frame the motivation of the current research. During these descriptions the phenomenological issues such as the fluid dynamics, chemical reactions, and turbulence are highlighted. This is followed by a description of how the time and length scales of these various aspects impact computational models. Finally, the specific scope of the present thesis is defined and the approach adopted to solve these problems is presented.

1.1 Reactive Munition

The first munition problem of interest is a weapon concept dependent on the mixture of fuel and oxidizer and shock initiation and is similar to the concepts discussed by Gore et al. (1993). This class of weapons differs from conventional munitions in the manner by which they derive their destructive force. This destructive force has to be generated by some energy source and in typical munitions, such as general purpose bombs, the source is a condensed phase explosive. This explosive contains the chemical compounds needed to generate the force once initiated by a fuse. Alternate munition concepts are based on the idea of generating the destructive force from alternative means. This may be done to enhance the energy source beyond that which is carried to the target but another focus is to use materials on target as energy sources. This is highly attractive for munitions to be launched from both ships and aircraft given the fact that the less material that must be carried to the target, the

lighter and smaller the munitions system must be. This directly impacts logistic concerns such as storage as well as factors such as the fuel required to deliver the munitions.

This current study is part of an effort to study the various physical and chemical phenomena which directly impact the effectiveness of new munition concepts. Another facet of the effort is to quantify the modeling tools needed to simulate this class of weapons and to aid in the development of engineering codes useful in design and evaluation of these various concepts. The range of concepts and targets which fall in this category is quite extensive and a complete review is beyond the scope of this document. Therefore, one target and one munition concept are highlighted here. However, it should be noted that the underlying physical and chemical processes to be presented in the current context are common to all targets and munition concepts.

As mentioned, one of the premises of various new munitions is to take advantage of materials on target which can be compromised and used to defeat the target. One component common to all air vehicles whether missiles or aircraft is on-board fuel. Given the particular vehicle, the fuel can be stored in various states. For brevity, here we consider an air vehicle carrying fuel in a fluid state. For example, most aircraft contain numerous fuel cells in the wings and fuselages. Depending on the stage in the mission, the fuel cells contain some level of liquid fuel as well as fuel vapor. Therefore, the munition concept used to help define the important physical and chemical phenomena to be studied centers around using the on-board fuel in a combustion process as the source of energy to generate the destructive force.

Even though there can be an ample supply of fuel on target and an ample supply of oxidizer, the ambient air, if the required conditions are not achieved, the munition-target system can remain in a fuel or oxidizer rich state and no effective combustion is initiated. One plausible system concept to attack the fuel cells is a weapon that generates a "cloud" of objects designed to penetrate and destroy the fuel cells. The focus of the current project is to study various key phenomena to aid in the development of an engineering level model with which to quantify the destruction output once this "cloud" intercepts the fuel cell.

Continuing with the concept of attacking the fuel cell, the target can be thought of as a control volume bounded by a solid wall with specific characteristics such as material and thickness. In the context of the larger issue of weapon effectiveness, criteria which need to be quantified and are dependent on output from any model of the munition-target interaction are factors such as whether the walls are damaged such that this damage is rapidly transferred throughout the entire air vehicle. Two tragic examples of such a process are the recent Valujet and TWA Flight 800 accidents. In the first case, the predominant theory is that the damage was initiated by the failure of one or several oxygen generators (McKenna, 1996). In the TWA case, as of this writing, it is still unknown whether the damage to the aircraft had been initiated by an explosive device or a system malfunction. Regardless of the initiation process, damage in both cases had been tremendous due to the fact that conditions were such that the destruction process was sustainable. In any combustion process, which both these cases entailed, sustainment is dependent on the correct supply of fuel and oxidizer as well as the required system settings. The first goal of this effort is to better understand the relationship between such system settings and the physical and chemical phenomena which conspire together to generate global effects such as the destructive force output. The second goal of the present work is to quantify the attributes of the computational model required to simulate these phenomena.

Our fuel cell scenario is depicted in Figures 1.1 and 1.2 and the steps leading to destruction are as follows. The fuel cell contains some amount of liquid fuel (F_l) as well as fuel vapor (F_v). At stage 1, the projectile intercepts the fuel cell with a shock front (S_f) due to the projectile flight through the ambient region which is composed of air, an oxidizer (O). After the projectile enters the fuel cell, the structure of the established shock (S_f) changes somewhat due to the properties of the fuel. There may also be a precursor compression (S_p) wave initiated by the impact of the projectile with the fuel cell wall. The strengths of the established shock in stage 2 and precursor compression wave depend on the characteristics of the wall. If the wall is relatively thin, then the momentum transfer from the projectile to the

wall is negligible before the projectile penetrates. On the other hand, for a stronger wall, the momentum transfer will be larger and the velocity of the projectile will decrease substantially during penetration. This would result in a stronger precursor compression wave and dramatically weaken the shock already established by the projectile.
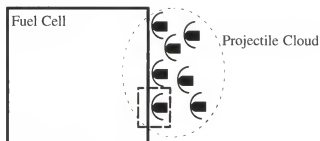
Figure 1.1. Fuel cell scenario showing projectile cloud. Single projectile highlighted in Figure 1.2.

After penetration, as the projectile and shock proceed through the cell, the heat from the shock can vaporizes any liquid fuel. This fuel vapor mixes with the oxidizer (O) which has penetrated into the fuel cell and the mixing is enhanced by the wake of the projectile. The projectile may be constructed out of an ablative material formulated to enhance the reaction process. In that case, the projectile changes phase from a solid (M_s) to eventually a gas (M_g). This compound reacts with the fuel vapor (F_v) and oxidizer (O) to produce a final product (P). The final step leading to destruction is for the reaction to reach a state such that it will progress through the fuel cell and combine with the same process initiated by the other projectiles.

The overall effectiveness of this or any weapon concept is a function of the target and weapon system parameters. The target parameters here include primarily the fuel chemical composition, phase, and state which directly impact key aspects such as how much total energy is needed to compromise the fuel volume. These aspects are controlled by a combination of detailed phenomena such as chemical time scales. The second of the target

(1) – Projectile intercepts fuel cell.
– Shock (S_f) due to flight through ambient air.
– Fuel cell contains some level of liquid fuel (F_l) and fuel vapor (F_v)

(2) – Precursor (S_p) generated during penetration
– Heat release behind shock (S_f) produces fuel vapor (F_v)
– Oxidizer (O) penetrates cell

(3) – Solid projectile (M_s) ablates producing gas (M_g)
– Fuel vapor (F_v), catalysis (M_g) and oxidizer (O) mix and react producing product (P)

(4) – Reaction front (R_f) proceeds through cell

Figure 1.2.   Sequence of events surrounding an individual projectile.

parameters is the container characteristics such as wall material and thickness. In this example, these parameters enter into the analysis process somewhere between the modeling of the munition-target interaction assessment and a larger lethality model. Essentially, some sort of effective destruction power is generated and the effectiveness of this power in damaging the fuel cell wall and surrounding structures has to be quantified and this damage output is fed into a higher level lethality model.

The second class of parameters is those associated with the munition. The particular munition concept used in the current discussion is a scenario where the fuel cell is infiltrated by a certain number of projectiles. Therefore, the munition parameters are first the number of projectiles and their dispersion pattern. Next are the parameters of the individual projectiles such as their size, shape, material composition and velocity. The importance of these parameters on the system effectiveness is manifested in how they drive the important detailed physical and chemical phenomena. From an application context, the quantities of interest are the global effects such as the destructive force generated during the munition-target interaction. In the fuel cell scenario one key global effect is whether combustion is achieved and sustained. The correlation between system parameters and these global effects is controlled by the detailed physical and chemical phenomena.

It is clear from the description of the fuel cell problem that among the key physical phenomena is the mixing of the fuel and oxidizer. Given the flow scenario, turbulence plays a key role in the mixing as well as the transport of heat. Among the processes of interest are phase change and the reactions between the fuel and oxidizer. The modeling of these various phenomena is the focus of the present work.

1.2 Gun Muzzle Blast

The second munition problem used in the current study is the simulation of gun muzzle blast. This problem contains many of the same physical and chemical processes discussed in the description of the reactive munition problem and requires much of the same modeling tools. However, here computational efficiency is paramount given the desire to

develop an engineering tool useful in the design of muzzle devices. The primary concern in this problem is the reduction of the pressure levels generated when a conventional gun is fired. In the case of large caliber systems, the reduction is sought to alleviate loads the support vehicle must sustain. In small caliber guns, the concern is the associated hearing loss from repeated use and the ability to go undetected for certain applications.

This problem has been studied by several investigators. The primary tool of investigation has been experiments with a limited computational effort. A literature review is provided in a later chapter. Here the problem is described to highlight the need for further research. The ballistic process determining blast is depicted in Figure 1.3 and can be divided into two domains. The first is the interior ballistic cycle where the solid propellant in the rounds is ignited and burned. This results in a build-up of chamber pressure which accelerates the projectile down the barrel. Following the projectile is a volume of gun gas which is created from the spent propellant. This gas is characterized by both high pressures and temperatures as well as some level of particle loading. The point in the barrel where the particle loading is not changing and the solid propellant has been combusted to essentially an equilibrium state can be considered as the boundary between the interior ballistic cycle and the launch cycle (point A in Figure 1.3). This is the point where the current code imposes specific boundary conditions.

The launch cycle encompasses various physical occurrences such as the projectile exiting the barrel and the progression of the precursor and main blast wave from the barrel into the ambient environment. The precursor blast wave denotes the shock created by the fly-out of the projectile while the main blast wave denotes the high pressure gun gas which exits the muzzle with the projectile. The level of blast experienced is also directly related to parameters such as the particular propellant used in the rounds.

Another physical phenomenon which often occurs when a conventional gun is fired is muzzle flash. The occurrence of muzzle flash is a result of further combustion of the gun gas with the ambient air. This chemical reaction process not only generates flash but also
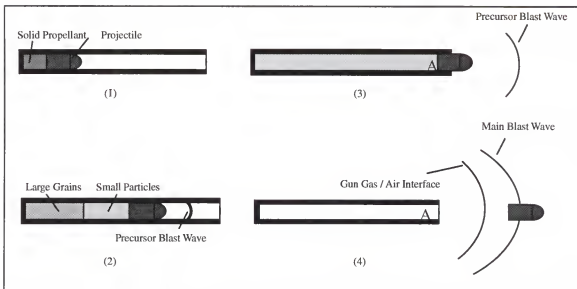
Figure 1.3.   Interior ballistic and launch cycle of a typical conventional gun.

alters the overpressure signature. Even though the focus here is on the overpressure, it is worthwhile describing the mechanics of the occurrence of flash to obtain a full appreciation of the problem.

The gun gas which is discharged during the launch cycle is always high in temperature, always contains some level of solid particle loading, and is typically rich in hydrocarbons which can react with the oxygen in the ambient air. Flash associated with conventional guns can be classified in three main regions; primary, intermediate, and secondary flash. These regions not only occur at different stages in time after the gun firing, but also in different spatial regions of the field downstream of the gun muzzle. These regions are represented in Figure 1.4. The primary flash is located at the exit of the muzzle and encompasses a small spatial region and is low in intensity. However, the intermediate flash is a more extensive region of greater intensity and occurs just downstream of the shock disk which forms some distance from the muzzle exit. The location of the intermediate flash region is a direct result of the fact that it is the heating of the gun gas by the shock disk which initiates the combustion producing the flash. Another influence of the shock disk is the

reduction in the velocity of the gas which increases the residence time of the gas and promotes the initiation of the chemical reactions.

In addition to the heating from the shock disk and the reduction in the gun gas velocity as it crosses the shock, a certain level of oxygen must be mixed with the gun gas before the flash occurs. This is why there is typically a delay between the firing of the gun and the occurrence of the intermediate flash. This delay is directly dependent on the time it takes to entrain oxygen from the ambient air and to mix it through the volume of gun gas toward the line of fire. The entrainment process is highly dependent on the turbulent processes which operate along the interface between the gun gas and ambient air. Therefore, any alteration to the gun system such as the addition of a muzzle device will impact the mixing process and in turn the intermediate flash.

The level of flash generated from the intermediate region is typically repeatable from firing to firing for a given gun system, i.e. gun caliber, ammunition, and muzzle device. The caliber of the gun and the ammunition fired determine the volume of the gas discharged as well as the gas properties when it exits the muzzle. These gas properties set the characteristics of the shock disk as well as the conditions upstream of the disk such as the fuel richness. Along with the influence of any muzzle device mentioned earlier, these parameters determine the level of flash in the intermediate region.

Secondary flash is the final and typically the largest and most intense region of the three. Like the intermediate flash, the secondary flash is initiated by the mixing of the oxygen rich air and gun gas and also requires a source of energy to initiate the reaction. And as before, the residence time of the mixture must be such to allow combustion to initiate and progress. In the case of the intermediate flash, the shock disk provides the energy source as well as reduced the velocity of the gas to ensure a high enough residence time. In the case of secondary flash, it has been found (Klingenberg and Heimerl, 1992) that if the temperature in the intermediate flash region does not reach a certain level, dependent on the ammunition, then secondary flash does not occur. This supports the theory that the heat released in the
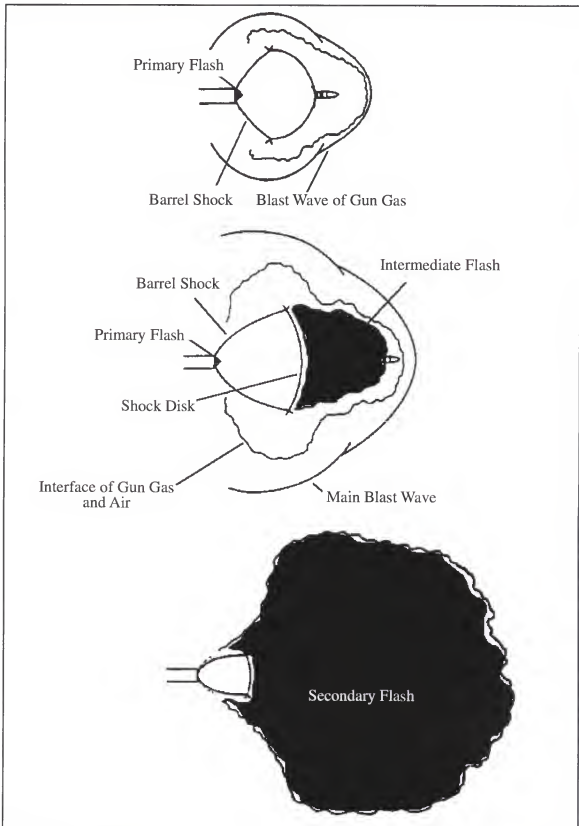
Figure 1.4. Depiction of flash regions and the development of muzzle blast and flash.

intermediate flash is the energy source for initiating the secondary flash which occurs some time after the intermediate flash and further downstream. The residence time criterion is met by the ever increasing volume of gun gas. As the cloud of gas grows larger, the velocity throughout the cloud is reduced. Therefore, as depicted in Figure 1.4, the secondary flash covers a larger area of the field. Secondary flash from shot to shot is not as repeatable as intermediate flash. This is due to the difference in the initiation process. In the case of intermediate flash, the initiation is driven by the shock disk which is less influenced by small perturbations in both the ambient field and the particular round fired. The initiation of secondary flash is much more dependent on the transport of both species and heat in a much larger region, further from the gun muzzle. This makes it more accessible to ambient influences such as winds.

To simulate all the intricacies of flash requires a detailed model of the chemical composition of the gun gas. Some modeling efforts have been carried out and these are reviewed later. Since the focus of the current study is to predict the overpressure in regions somewhat removed from the gun system, the key phenomenon associated with the reactions which cause flash that must be reproduced is the energy released from the combustion. This is due to the fact that the combustion occurs behind the main blast wave. This deposition of energy behind this wave helps sustain the magnitude of the main blast wave as it progresses out into the field. This is key since the peak pressure at any location in the field is a function of the main blast wave magnitude. Therefore, the current model employs a reduced reaction mechanism in an attempt to better reproduce the blast levels without greatly increasing the computational requirements. However, the characteristics of the flash processes are to prove advantageous in evaluating the model.

1.3 Phenomenological Scales

The description of the problems above makes it clear that there are a multitude of physical and chemical processes key in high-speed, chemically reacting flows. Associated with this myriad of mechanisms are multiple time and length scales. The time and length

scales refer to the characteristic time and length over which effects due to certain physical and chemical mechanisms occur. Consequently, it is difficult to investigate this class of problems both theoretically and experimentally. Therefore, computational models are routinely used to study reacting flows and this is the methodology of the current work.

Any models used to simulate the various detailed phenomena involved must correctly reproduce all phenomena and their corresponding scales, or at the least the role the phenomena play in the larger problem. As for the numerical aspects of such models, the requirement to resolve a wide range of scales determines simulation parameters such as the computational time and computer memory needed to carry out a useful simulation. This is due to the fact that when solving a problem using computational models, the governing equations are usually solved at discrete points in time and space. Therefore, the temporal and spatial discretization must be done with both the time and length scales of interest in mind.

A key parameter of chemically reacting flows is the flow speed or the fluid dynamic time scale relative to the chemical processes. A nondimensional parameter useful in classifying problems is the Damköhler number defined as the ratio between the fluid dynamic and chemical time scales, $\mathfrak{D} = \tau_f/\tau_c$. For low-speed flows, the chemical processes typically occur orders of magnitude faster than the fluid dynamic processes. This implies $\mathfrak{D} \gg 1$ and adds validity to modeling assumptions such as local chemical equilibrium or thin flame zones. From a modeling standpoint, such assumptions allow the use of a simplified chemical reaction model. For instance, as a result of the equilibrium assumption, the finite rate chemical processes can be ignored and the presence of intermediate species may be neglected. Even if the flow is not in chemical equilibrium but the reactions can be considered fast, either a partial equilibrium (Correa and Shyy, 1987) or a progress variable (Libby and Williams, 1994) concept can be adopted. For the case of high-speed flows as in the case of shock-induced combustion, such assumptions are generally not valid and a model of the finite rate chemical reactions accounting for the detailed distribution of intermediate species is needed. This has direct implications as to the complexity of the computational model.

Many combustion problems have to address the issue of turbulence. This is due to the fact that the mixing characteristics of turbulence are routinely present with high Reynolds number flows. Also, in many cases turbulence is used in reactive systems to enhance the mixing and subsequently the combustion process. As in all turbulent flows, the aspects due to turbulence must first be compared to the mean flow and with the addition of reactions, the relative scales of the turbulence to the chemical processes are important. Turbulence is known to possess a multitude of scales, particularly the large scale eddies which contain what is labeled the turbulent kinetic energy (k) and the small scale eddies which work to dissipate this energy. The dynamics of turbulence consist of various processes by which the large eddies break down into small eddies and thereby transfer energy between the large and small eddies.

Depending on the relationship between the large and small scales of turbulence and those of the chemical reaction some conclusions can be drawn as to the impact of turbulence on the combustion process. A parameter useful in the analysis process is the ratio of the large-eddy time scale to the chemical time scale, the large-eddy Damköhler number ($\mathcal{D}_l = \tau_l/\tau_c$). The large-eddy time scale, $\tau_l = l/\sqrt{k}$, is defined using the characteristic length scale (l) and velocity ($\sqrt{k}$) of the eddy. Using this parameter, the regime of interest runs from slow chemistry, small $\mathcal{D}_l$, to fast chemistry, large $\mathcal{D}_l$. For the case of slow chemistry, the turbulent processes are working on a scale smaller than the chemical process. This produces enhanced mixing of reactants or even intermediate species resulting in the reaction zone being distributed in the flow field. In this case, the impact of turbulence on mass and thermal diffusion must be considered. For the case of fast chemistry the reactions take place on a scale much smaller than the large eddies. This results in distinct thin flame fronts which lie within the large eddies and are transported and strained by the turbulence. Such cases can be modeled using the laminar flamelet concept which is reviewed by Libby and Williams (1994). For the high-speed flows to be studied here, it is probable that the

turbulent and chemical time scales are comparable. Therefore, one goal of the current study is to incorporate the effects of turbulence on the chemical processes in the computation.

1.4 Summary

Here the problems to be studied have been described to identify the important physical and chemical processes which must be modeled. Given the high-speed nature of the flows, many assumptions used to reduce the complexity of models employed in low-speed combustion are not applicable. Some of the length and time scales have been identified and how these impact the numerical aspects of the model is discussed later. The first primary focus of the current effort is to quantify the complexity of the models needed to accurately simulate the munition problems of interest. The second focus is to identify the impact both the phenomenological and numerical aspects of these models have on the accuracy of these simulations. The remainder of this document describes the specific models and computations to be carried out.

Chapter 2 describes in detail a shock-induced combustion scenario to be used as a representation of the munition problem consisting of the fuel cell scenario. This is done in part due to the availability of experimental data associated with the particular scenario. Also, this scenario has been studied by previous investigators using a wide variety of physical, chemical, and numerical models. A literature review of these earlier works is given to help draw clear comparisons between these efforts and the current study. Using the code developed here, many of these various models can be tested within a single computational framework to ascertain the correlation between these various models and simulation accuracy. This not only allows judgments to be made as to the validity of the various models but also aids in quantifying the fidelity needed in a computational tool for the munition concepts of interest.

The governing equations of the current class of munition problems are presented in Chapter 3 along with a detailed description of the computational code developed here. It is to become evident that there exist numerous modeling options for the various facets of the

code from both a phenomenological and numerical point of view. Where appropriate these options are discussed. The assumptions which drive the model selection are detailed as well as compelling reasons for the current model selection based on both the physical and chemical aspects of the problems to be solved and the computational requirements the solution process must meet. Also discussed in Chapter 3 are the various numerical techniques used in the present computational code.

Chapter 4 describes the turbulence model used in the current effort as well as the various terms which are impacted by the turbulence aspects of the flow scenarios. The model selection for the representation of turbulence is driven in a large part by the computational requirements of the code developed here. Various model modifications for addressing attributes of the high-speed flows to be solved are also discussed.

Results for the shock-induced combustion scenario are presented in Chapter 5. Among the data reviewed is analysis as to how the chemical model and numerical aspects of the code impact accuracy. Computations using both inviscid and turbulence fluid dynamic models are presented to both test the current code but also the ascertain to what extent the turbulence aspects of the flow impact the combustion scenario. The current results are reviewed in the context of previous findings both to support the conclusion of the present effort and to fill in those aspects of solving this class of flows not directly addressed in earlier studies.

A literature review of pertinent work in the area of gun muzzle blast is provided in Chapter 6. Many of the conclusions and findings of these earlier efforts have helped steer the development of the current code used to simulate this munition problem. It is to be made evident that the models to date have ignored some of the physical and chemical processes and it is the focus of the present effort to quantify the impact these processes have on the generation of muzzle blast. This is followed in Chapter 7 by a description of how the model discussed in Chapter 3 is used to simulate the muzzle blast scenario. Chapter 7 also presents

results using a computational model analogous to those used in earlier efforts and compares these simulations to results from the current model.

Finally, Chapter 8 summarizes the findings of the present study into both the shock-induced combustion and gun muzzle blast problems. The accuracy of the code developed here is discussed as well as the computational requirements. Areas into which more focus is needed are identified in the context of the munition problems of interest. Also, in a more general sense, those issues in need of more attention to increase the capability of simulating high-speed reacting flows for full scale engineering problems are identified and some suggestions for the future direction are made.

CHAPTER 2
SHOCK-INDUCED COMBUSTION

The fuel tank scenario described earlier contains a multitude of physical and chemical processes. The predominate processes are the shock dynamics, mixing, phase change, and chemical reactions between the fuel and oxidizer. For the current look into this class of problems, a premixed combustion scenario is studied. The shock dynamics are explicitly present and the mixing aspects are manifested in the importance of the distribution of intermediate species and heat. The chemical processes are represented by the chemical reactions between the fuel and oxidizer. Aspects also important to the phase change process are present. These include the competition between the fluid dynamics and chemical time scales and the dependence of the process on local field properties.

The combustion scenario to be used in the present research for studying the reactive munition problem is the shock-induced combustion scenario studied experimentally by Lehr (1972). In his experiments, Lehr shot projectiles into stoichiometric hydrogen and air mixtures as well as hydrogen and oxygen mixtures. Projectiles of various geometries have been used but here only data from shots using hemispherically nosed projectiles are studied. Lehr's primary findings are that the flow field features generated by the shock-induced combustion can either be one of steady combustion or a situation in which unsteady combustion occurs. The case of unsteady combustion can be further subdivided into low and high frequency regimes. The regime achieved is found to be directly related to the ratio of the projectile velocity to the detonation velocity of the mixture. The data available from Lehr's study are qualitative in nature and are in the form of shadowgraphs. A representative image from the three regimes has been provided by Lehr (personal communication, 1995)

and is shown in Figure 2.1. The shock in all three images is visible as is a second front due to the chemical reactions and labeled the energy release, or reaction front. All three of these cases are for a stoichiometric mixture of hydrogen and air at a temperature of 293 K and a pressure of 320 Torr.

As is clear by the images in the figure, for those cases where the velocity of the projectile is lower than that of the detonation velocity of the mixture (V_D), an instability is seen in the reaction front. As the velocity approaches the detonation velocity, the frequency of the instability increases until the combustion becomes stable at velocities greater than V_D. It should be noted that at the other end of the velocity spectrum, for low Mach numbers, no

$V_P = 1685$ m/s
$V_P/V_D = .82$
$M = 4.18$
freq = 150 kHz

$V_P = 1931$ m/s
$V_P/V_D = .94$
$M = 4.79$
freq = 720 kHz

$V_P = 2605$ m/s
$V_P/V_D = 1.27$
$M = 6.46$
freq = steady
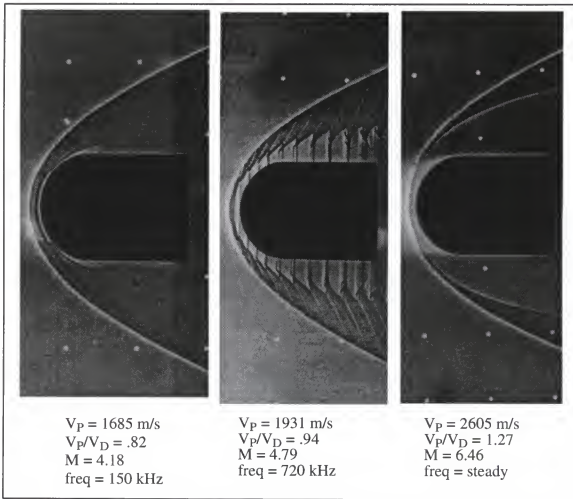
Figure 2.1. Example shadowgraphs from Lehr's Experiments.

combustion is initiated. Several investigators have proposed theories as to the important phenomena driving the instability and have supported their theories with computations. Among these is the work of McVey and Toong (1971), Alpert and Toong (1971), Matsuo et al. (1993), and Matsuo and Fujiwara (1993). There is also some question among the investigators as to when the actual transition from unsteady to steady occurs. Sussman (1994) presents arguments that the transition does not occur exactly at $V_P/V_D = 1$.

Many investigators have simulated the cases presented in Figure 2.1 and a review is provided in the next section. However, here some general comments are needed on the experimental data themselves as well as any computational effort to simulate these shock-induced combustion cases. The shadowgraph from Lehr for M=6.46 is shown in Figure 2.2 with points used to denote the shock and reaction fronts. It has been verified (Lehr, personal communication, 1995) that hemispherically nosed projectiles with cylindrical bodies have been used in the experiments. However, in the image the nose of the projectile does not appear to be a true hemisphere. One possible source for this alteration is that the projectile is simply yawed. Such a yawing would also be evident in a corresponding change to the projectile's baseline seen in the images and this is not the case. There is a slight alteration to the baseline in the images but not nearly on the order of the alteration of the nose. After consultation with Lehr it has been verified that the alteration is due to the optical system (Lehr and Maurer, 1969) and he cautions against using the data for precise measurements. However, the data can be used qualitatively to benchmark the computational models to see if the flow field features are being captured. And given the fact the current study is focused on the interplay of the fluid dynamics and chemical processes, Lehr's experiments offer a solid set of data in which the scales of each of these aspects are comparable.

As is evident by now, the successful simulation of a flow scenario such as Lehr's experiments (Lehr, 1972) or the reactive munition problem requires a multitude of models for the various phenomenological aspects. Each model not only embodies the particular
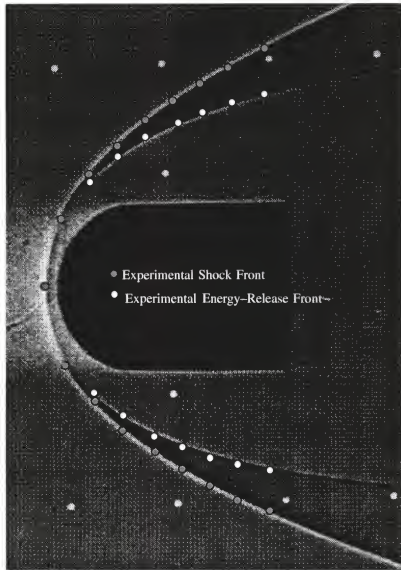
Figure 2.2. Shadowgraph for M=6.46 with the shock and reaction front denoted.

phenomenology framework used to represent either the physics or chemistry but also their numerical traits. For instance, the reaction process between hydrogen and oxygen in reality occurs through countless intermediate processes. However, to represent this phenomenon with a numerical model, a distinct number of reaction steps must be selected and reaction rates for these steps must be specified. The selection of a particular model, i.e. the number of steps and rates, inherently specifies the chemical scales produced by the model. These

scales may or may not match those which exist in reality. If a discrepancy exists between the computation and experimental data, the model can be altered until a good match is made. This can increase the confidence in the ability of the model to reproduce key phenomenological characteristics such as the chemical time scales in the case of the reaction model. However, such alteration should be done with caution. For example, many computations have been carried out by previous investigators for the shock-induced combustion scenario captured by Lehr (1972). In these earlier studies, several reaction mechanisms have been used as well as a variety of grids. In most cases, an individual study uses a single reaction mechanism and the grid is adapted or other numerical aspects are altered until good agreement with experimental results is achieved. The accuracy of the computation is dependent not on a single model but the combination of all models. It is to become clear that for this class of problems, the phenomenological and numerical aspects must be considered in conjunction.

2.1 Reaction Mechanisms for Hydrogen and Oxygen

One of the predominate differences among the earlier computational studies into the shock-induced combustion scenario is the representation of the chemical reactions. Therefore, here a description of various reaction mechanisms used for hydrogen and oxygen is provided. As detailed earlier, the chemical processes in the problems of interest have time scales such that a finite rate chemistry model is needed. The chemical reaction processes involved are incorporated into the governing equations by way of the source terms to be defined later.

There have been many reaction mechanisms proposed for the reaction between hydrogen and air. Here, just those used in the previous computational studies to be reviewed and those used in the current study are presented. They range in complexity from a 2-step global model proposed by Rogers and Chinitz (1983) to a 32-step model proposed by Jachimowski which is based on his original 33-step model (Jachimowski, 1988) but incorporates a slight modification he and others suggest (Oldenborg et al., 1988). These

mechanisms are presented in Tables 2.1 through 2.7. The constants are used to calculate the rate of the individual reaction using the Arrhenius expression

$$k_n = A_n T^{b_n} \exp\left[\frac{-Ea_n}{R_u T}\right] \tag{2.1}$$

which is discussed in more detail later. In the review, a 19-step mechanism is mentioned. This mechanism is composed of the first 19 steps of the Jachimowski. Note, the two 8-step mechanisms presented use the same steps but different rate constants.

Table 2.1. Two-step hydrogen-oxygen reaction mechanism from Rogers and Chintz (1983).

n	Reaction	A_n	b_n	Ea_n / Ru
1	$H_2 + O_2 = 2OH$	$(8.917\phi + 31.433/\phi - 28.950) \times 10^{47}$	-10	2449.77
2	$H_2 + 2OH = 2H_2O$	$(2.0 + 1.333/\phi - 0.833\phi) \times 10^{64}$	-13	21400.87

ϕ = equivalence ration, set to 1 in current computations

Units are moles, seconds, centimeters, and Kelvin

Table 2.2. Seven-step hydrogen-oxygen reaction mechanism used by Shang et al. (1995) based on eighteen–step mechanisms from Drummond et. al. (1986).

n	Reaction	A_n	b_n	Ea_n / Ru
1	$H_2 + O_2 = 2OH$	1.7×10^{13}	0	24233.
2	$H + O_2 = OH + O$	1.42×10^{14}	0	8254.
3	$H_2 + OH = H + H_2O$	3.16×10^{7}	1.8	1525.
4	$O + H_2 = OH + H$	2.07×10^{14}	0	6920.
5	$2OH = H_2O + O$	5.5×10^{13}	0	3523.
6	$H + OH + M = H_2O + M$	2.21×10^{22}	-2	0.
7	$2H + M = H_2 + M$	6.53×10^{17}	-1	0.

Units are moles, seconds, centimeters, and Kelvin

<u>2.2 Previous Computational Studies of Lehr's Experiments</u>

Both steady and unsteady combustion cases captured in shadowgraphs by Lehr (1972) have been studied by several investigators using numerical techniques. The actual

Table 2.3. Eight-step hydrogen-oxygen reaction mechanism from Moretti (1965).

n	Reaction	A_n	b_n	Ea_n / Ru
1	$H + O_2 = OH + O$	3.0×10^{14}	0	8810.
2	$O + H_2 = OH + H$	3.0×10^{14}	0	4030.
3	$H_2 + OH = H + H_2O$	3.0×10^{14}	0	3020.
4	$2OH = O + H_2O$	3.0×10^{14}	0	3020.
5	$H_2 + M = 2H + M$	1.85×10^{17}	-1	54000.
6	$H_2O + M = OH + H + M$	9.66×10^{18}	-1	62200.
7	$OH + M = O + H + M$	8.0×10^{16}	-1	52200.
8	$O_2 + M = 2O$	5.8×10^{16}	-1	60600.

Units are moles, seconds, centimeters, and Kelvin

Table 2.4. Eight-step hydrogen-oxygen reaction mechanism from Moretti (1965) with rate constants proposed by Evans and Schexnayder (1980).

n	Reaction	A_n	b_n	Ea_n / Ru
1	$H + O_2 = OH + O$	1.2×10^{17}	$-.91$	8315.
2	$O + H_2 = OH + H$	7.5×10^{13}	0	5586.
3	$H_2 + OH = H + H_2O$	2.0×10^{13}	0	2600.
4	$2OH = O + H_2O$	5.3×10^{12}	0	503.
5	$H_2 + M = 2H + M$	5.5×10^{18}	-1	51987.
6	$H_2O + M = OH + H + M$	5.5×10^{18}	-1.5	59386.
7	$OH + M = O + H + M$	8.5×10^{18}	-1	50830.
8	$O_2 + M = 2O$	7.2×10^{18}	-1	59340.

Units are moles, seconds, centimeters, and Kelvin

parameter range studied by Lehr exceeds that presented by Lehr (1972) and these additional data have been provided by Lehr (personal communication, 1995). Here a brief review of previous numerical studies is provided. In addition to the impact the reaction mechanism has on the computed results, the numerical aspects including solution method and grid resolution strongly affect the computed flow fields. Therefore, a description of these facets of each study is included in the review along with key results.

Yungster et al. (1989) have computed the M=6.46, hydrogen-air case captured by Lehr (1972) as well as the shots into hydrogen and oxygen presented by Lehr (1972). The 8-step reaction mechanism for hydrogen and air presented in Table 2.4 by Moretti (1965) is used but the rate constants are replaced by values given by Evans and Schexnayder (1980).

Table 2.5. Eighteen-step hydrogen-oxygen reaction mechanism from Drummond et al. (1986) used by Ahuja and Tiwari (1993).

n	Reaction	A_n	b_n	Ea_n / Ru
1	$O_2 + H_2 = 2OH$	1.70×10^{13}	0	24245.93
2	$O_2 + H = OH + O$	1.42×10^{14}	0	8258.22
3	$H_2 + OH = H_2O + H$	3.16×10^{7}	1.8	1525.76
4	$H_2 + O = OH + H$	2.07×10^{14}	0	6923.81
5	$2OH = H_2O + O$	5.50×10^{13}	0	3524.85
6	$OH + H + M = H_2O + M$	2.21×10^{22}	-2	0.
7	$2H + M = H_2 + M$	6.53×10^{17}	-1	0.
8	$H + O_2 + M = HO_2 + M$	3.20×10^{18}	-1	0.
9	$HO_2 + OH = H_2O + O_2$	5.00×10^{13}	0	503.55
10	$HO_2 + H = H_2 + O_2$	2.53×10^{13}	0	352.48
11	$HO_2 + H = 2 OH$	1.99×10^{14}	0	906.39
12	$HO_2 + O = OH + O_2$	5.00×10^{13}	0	503.55
13	$2HO_2 = H_2O_2 + O_2$	1.99×10^{12}	0	0.
14	$HO_2 + H_2 = H_2O_2 + H$	3.01×10^{11}	0	9416.39
15	$H_2O_2 + OH = H_2O + HO_2$	1.02×10^{13}	0	956.75
16	$H_2O_2 + H = H_2O + OH$	5.00×10^{14}	0	5035.50
17	$H_2O_2 + O = HO_2 + OH$	1.99×10^{13}	0	2970.95
18	$H_2O_2 + M = 2OH$	1.21×10^{17}	0	22911.53

Units are moles, seconds, centimeters, and Kelvin

The governing equations are solved using a fully coupled equation set and the total variation diminishing (TVD) algorithm by Yee and Shinn (1989), also known as the "point implicit TVD MacCormack." Grids of resolution 42x44 and 32x32 are used with the only difference reported between the solutions being the "thickness of the captured shocks." Good agreement between the computed shock and reaction front location and the experimental value is reported. However, only a limited region encompassing the nose is modeled.

Lee and Deiwert (1989) have computed the M=6.46 case using the F3D code by Ying (1986) which is based on the implicit flux vector splitting method. The governing equations are solved in a loosely-coupled approach which assumes that in the Jacobians of the fluxes, the effective specific heat ratio and pressure are not affected by the changes in species mass fractions. The reaction mechanism used is the same as that of Yungster et al. (1989). Some of the calculations are carried out with the rate coefficients reduced one and two orders of magnitude in an effort to quantify the impact of reaction rates on the flow field. They do find

Table 2.6. Nineteen-step hydrogen-oxygen reaction mechanism used by Oldenborg et al. (1990).

n	Reaction	A_n	b_n	Ea_n / Ru
1	$O_2 + H_2 = H + H_2O$	2.16×10^8	1.51	1726.
2	$H + O_2 = O + OH$	1.91×10^{14}	0.	8273.
3	$O + H_2 = H + OH$	5.06×10^4	2.67	3166.
4	$H + HO_2 = H_2 + O_2$	2.50×10^{13}	0.	349.
5	$H + HO_2 = 2OH$	1.50×10^{14}	0.	505.
6	$O + HO_2 = OH + O_2$	2.00×10^{13}	0.	0.
7	$OH + HO_2 = H_2O + O_2$	2.00×10^{13}	0.	0.
8	$H + O_2 + M = HO_2 + M$	8.00×10^{17}	$-.8$	0.
9	$H + OH + M = H_2O + M$	8.62×10^{21}	$-2.$	0.
10	$2H + M = H_2 + M$	7.30×10^{17}	$-1.$	0.
11	$H + O + M = OH + M$	2.60×10^{16}	$-.6$	0.
12	$2O + M = O_2 + M$	1.14×10^{17}	$-1.$	0.
13	$2OH = O + H_2O$	1.50×10^9	1.14	0.
14	$2OH + M = H_2O_2 + M$	4.73×10^{11}	1.	$-3206.$
15	$OH + H_2O_2 = H_2O + HO_2$	7.00×10^{12}	0.	722.
16	$O + H_2O_2 = OH + HO_2$	2.80×10^{13}	0	3220.
17	$H + H_2O_2 = H_2 + HO_2$	1.70×10^{12}	0	1900.
18	$H + H_2O_2 = H_2O + OH$	1.00×10^{13}	0	1800.
19	$2HO_2 = H_2O_2 + O_2$	2.00×10^{12}	0	0.

Units are moles, seconds, centimeters, and Kelvin

that the slower rates do impact both the computed shock location and the temperature field behind the shock. Their results are discussed further in the context of the results from the current study. A grid of resolution 57 x 41 over the nose region is used and the results are reported to be very similar to those by Yungster et al. (1989).

Wilson and MacCormack (1990) compute the steady combustion cases at M=5.11 and 6.46 using the 32-step reaction mechanism given in Table 2.7. The mechanism, as presented by Wilson and MacCormack (1990), is in a slightly different order and there is a typographical error in the pre-exponential constant for reaction 21. The constant A_n for reaction 10 is different than that used by Jachimowski (1988). Wilson (personal communication, 1997) reports this alteration has been made based on the rate information available in other sources such as the work of Warnatz (1984). In the current study, the rate for step 10 as defined by Wilson and MacCormack (1990) is used to facilitate comparisons. A fully-implicit flux-splitting technique based on the work by MacCormack (1985) and

Table 2.7. Hydrogen-oxygen reaction mechanism from Jachimowski (1988).

n	Reaction	A_n	b_n	Ea_n / Ru
1	$H_2 + O_2 = HO_2 + H$	1.0×10^{14}	0	28198.8
2	$H + O_2 = OH + O$	2.6×10^{14}	0	8459.64
3	$O + H_2 = OH + H$	1.8×10^{10}	1	4481.6
4	$OH + H_2 = H + H_2O$	2.2×10^{13}	0	2593.28
5	$2OH = O + H_2O$	6.3×10^{12}	0	548.87
6	$H + OH + M = H_2O + M$	2.2×10^{22}	-2	0.
7	$2H + M = H_2 + M$	6.4×10^{17}	-1	0.
8	$H + O + M = OH + M$	6.0×10^{16}	$-.6$	0.
9	$H + O_2 + M = HO_2 + M$	2.1×10^{15}	0.	-503.55
10	$2O + M = O_2 + M$	6.0×10^{13}	0.	-906.39
11	$HO_2 + H = 2 OH$	1.4×10^{14}	0.	543.83
12	$HO_2 + H = H_2O + O$	1.0×10^{13}	0.	543.83
13	$HO_2 + O = O_2 + OH$	1.5×10^{13}	0.	478.37
14	$HO_2 + OH = H_2O + O_2$	8.0×10^{12}	0.	0.
15	$2HO_2 = H_2O_2 + O_2$	2.0×10^{12}	0.	0.
16	$H + H_2O_2 = H_2 + HO_2$	1.4×10^{12}	0.	1812.78
17	$H_2O_2 = OH + HO_2$	1.4×10^{13}	0.	3222.72
18	$OH + H_2O_2 = H_2O + HO_2$	6.1×10^{12}	0.	720.08
19	$H_2O_2 + M = 2OH + M$	1.2×10^{17}	0.	22911.53
20	$2N + M = N_2 + M$	2.8×10^{17}	$-.75$	0
21	$N + O_2 = NO + O$	6.4×10^{9}	1	3172.36
22	$N + NO = N_2 + O$	1.6×10^{13}	0	0
23	$N + OH = NO + H$	6.3×10^{11}	.5	0
24	$H + NO + M = HNO + M$	5.4×10^{15}	0	-302.13
25	$H + HNO = NO + H_2$	4.8×10^{12}	0	0
26	$O + HNO = NO + OH$	5.0×10^{11}	.5	0
27	$OH + HNO = NO + H_2O$	3.6×10^{13}	0	0
28	$HO_2 + HNO = NO + H_2O_2$	2.0×10^{12}	0	0
29	$HO_2 + NO = NO_2 + OH$	3.4×10^{12}	0	-130.92
30	$H + NO_2 = NO + OH$	3.5×10^{14}	0	755.33
31	$O + NO_2 = NO + O_2$	1.0×10^{13}	0	302.13
32	$M + NO_2 = NO + O + M$	1.16×10^{16}	0	33234.3

Units are moles, seconds, centimeters, and Kelvin
Third-body efficiencies : (6) $H_2O = 6.0$. (7) $H_2O = 6.0$, $H_2 = 2.0$, (8) $H_2O = 5.0$, (9) $H_2O = 16.0$, $H_2 = 2.0$, (19) $H_2O = 15.0$

Candler (1988) is used along with Steger-Warming flux splitting (Steger and Warming, 1981). The governing equations also include vibrational nonequilibrium effects; however, Wilson (personal communication, 1996) reports these effects to be negligible. The study evaluates increasing the induction delay by changing the reaction rate for $H + O_2 \leftrightarrows OH + O$, step 2 in Table 2.7. The rates

$$
\begin{align}
\text{(a)} \quad k_{f2} &= 2.60 \times 10^{14} \exp(-8459.64/T) \\
\text{(b)} \quad k_{f2} &= 1.91 \times 10^{14} \exp(-8277.35/T) \\
\text{(c)} \quad k_{f2} &= 1.2 \times 10^{17} T^{-.91} \exp(-8315.12/T)
\end{align}
\tag{2.2}
$$

are evaluated and it is determined choice (c), the rate suggested by Warnatz (1984) gives the best match for Lehr's experiments at M=5.11. This same rate is used to compute the M=6.46 case resulting in a good match of both computed shock and reaction front to the experiments. The M=6.46 case is computed on a 321 x 65 adapted mesh. In the current study, the 32-step mechanism with the rates per Warnatz is labeled the modified 32-step model. Wilson and MacCormack also evaluate altering the time of reaction by changing the rate constants for $H + OH + M \leftrightarrows H_2O + M$, step 6 in Table 2.7. This alteration affects the heat release rate and the time required to reach the peak temperature. Reducing the original rate per Jachimowski (1988) by a factor of 4 and using choice (a) above for $H + O_2 \leftrightarrows OH + O$ produces no significant change in shock and reaction front location.

Ahuja and Tiwari (1993) use an 18-step mechanism, given in Table 2.5, to compute the M=6.46 case. The mechanism is reported to be based on the work of Jachimowski (1988) and matches the mechanism used in Drummond's work (1988) except for inconsistencies in steps 9 and 10 given by Ahuja and Tiwari (1993) which are believed to be simply typographical errors. The rate constants are not provided by Ahuja and Tiwari (1993) but are presented here based on the data available from Drummond (1988). The equations are solved using MacCormack's method and a Lax-Wendroff type scheme is used for the fluxes. The grid resolution used is 197x152 over a domain comprising a quarter sphere. The computed flowfield is reported to show a shock and reaction front but it is difficult to make a detailed comparison to experiments given the limited computational domain.

Matsuo et al. (1993) use a 19-step reaction mechanism based on 32-step used by Wilson and MacCormack (1990). In the 19-step mechanism the nitrogen reactions are neglected and as mentioned, the specific reactions used are steps 1 through 19 of Table 2.7. The governing equations are integrated explicitly, and the chemical reaction source term is treated in a linearly point-implicit manner. Yee's non-MUSCL TVD upwind explicit scheme is used and computations have been carried out for the M=4.18 and 4.79 cases captured by Lehr (1972; personal communication, 1995). A grid of resolution 161x321 over a quarter

sphere domain is used. For the M=4.79 case, computations show the frequency of the unsteadiness to be 725 kHZ where the reported experimental frequency is 712 kHZ. For the M=4.18 case, a frequency of 159.8 kHz is computed where the experiments of Lehr (1972) report a frequency of 150kHz. Also important in this study is their characterization of the chemical time scales which is discussed later.

Sussman (1993) develops a source term modification scheme for use in combustion computations. Using a model problem, the error associated with the representation of the reaction source term is estimated. A scaling factor based on this error estimation is used in computing both a quasi-one dimensional shock-induced combustion scenario as well as the M=6.46 case captured by Lehr. This source term modification is discussed in detail in a later chapter and is evaluated in the current study. The 19-step reaction mechanism presented in Table 2.6 (Oldenborg et al., 1990) is used. The fluid dynamic terms are solved explicitly using the Harten-Yee (Yee, 1989) TVD algorithm and the source terms are integrated using a point implicit method. A grid resolution of 44x49 is used. In the quasi-one dimensional case, the source term modification results in a reduction in the number of grid cells needed to resolve the induction zone. This same scheme when used in Lehr's problem does not give improved results without the addition of a grid adaptation technique.

Wilson and Sussman (1993) use the 32-step mechanism as in Wilson and MacCormack (1990) with the rate suggested by Warnatz (1984). A logarithmic form of the species conservation equations is used for which a description is provided later. A comparison between Steger-Warming flux-vector splitting (Steger and Warming, 1981) based on work by MacCormack (1985) and Candler (1988) and Harten-Yee (Yee, 1989) upwind TVD scheme is made. The convective terms have been treated explicitly and source terms implicitly. Both steady and unsteady cases have been computed. For the steady case of M=6.46, a 52x52 grid is used with the logarithmic form of the equations. The computed shock and reaction fronts from both flux schemes compare well with experiments. For the unsteady case of M=4.79, a 375x161 grid is used but the standard form of the species

conservation equations is solved. The frequency of the unsteadiness is calculated to be 530 kHz where experiments are reported to be 720 kHz. The reported experimental value is slightly different from the value of 712kHz reported by Matsuo et al. (1993). The computations are repeated using the original rate for $H + O_2 \leftrightarrows OH + O$ per Jachimowski and the frequency is computed to be 820 kHz. Matsuo et al. (1993) cite a private communication with Wilson and Sussman that after running the computation for a longer time, the results match the experimental frequency better than the 820 kHz cited. The findings that a different rate for the $H + O_2 \leftrightarrows OH + O$ reaction are needed for the unsteady and earlier reported steady cases is one area of concern regarding the available reaction mechanisms.

Matsuo and Fujiwara (1993) compute the unsteady shock-induced combustion flow using the conditions from Lehr's experiments for M=4.18. The diameter of the nose is changed to generate different cases. A two-step mechanism using progression variables is used and the parameters are based on shock-tube data for $2H_2 + O_2 + 7Ar$. No direct comparison to Lehr's data is made but the computations are used to help explain the phenomena causing the instabilities. The solution scheme used is the same as in Matsuo et al. (1993). No details on the grid resolution are given.

Sussman (1994) presents results of computations for both the low and high frequency cases studied by Lehr. The equations are solved using the technique of Wilson and Sussman (1993) including the logarithmic form of the species governing equations. All computations are performed on a 192x252 grid over a quarter sphere domain and the 19-step mechanism of Table 2.6 (Oldenborg, et al., 1990) is used. Excellent agreement between the computed and experimentally measured frequencies is reported for all cases except at the lowest and highest projectile velocities. The discrepancy at the lowest frequency case is attributed to the fact that the energy release front is closest to the body at this velocity and either a finer grid in that region is needed or the neglect of the viscous effects is most prevalent here. The discrepancies at the high frequency end of the spectrum are suspected to be due to the difficulty in measuring the scales from the experimental results given their small amplitude.

Also of interest in Sussman's study is the discussion of the mechanism determining the instabilities. Sussman reports finding an instability for projectile velocities of 2119 m/s where Lehr (1972) found no evidence of unsteadiness. Sussman finds that this transition point from an unsteady to a steady combustion scenario it directly related to the point at which the induction time of the reaction becomes smaller than the energy release time. This criterion is different from the projectile-to-detonation velocity criterion mentioned earlier. The frequency of the instabilities is directly related to the induction time and given the fact that the computed values compare well with the experiments over the majority of the velocity regime, Sussman deduces that this aspect of the chemical process is being adequately modeled by the reaction mechanism being used. However, since the transition point from unsteady to steady combustion is over predicted, the energy release rate produced by the model is greater than that in the actual experiments. This conclusion that the ratio of energy release time, or reaction time, to the induction time is a key parameter is in agreement to the findings of Matsuo et al. (1993) and those of McVey and Toong (1971). Sussman also presents detailed computations of a one-dimensional shock-induced combustion scenario and demonstrates the advantages of solving the logarithmic form of the species equations.

Yungster and Radhakrishanan (1994) computed the unsteady cases captured by Lehr at M=4.18, 4.48, and 4.79. The 19-step mechanism of Matsuo et al. (1993) is used with the original rates per Jachimowski. The governing equations are solved fully coupled using Yee's 2nd order TVD scheme (Yee, 1989) and a grid resolution of 220x220 over half the hemispherical nose region. Good agreement between computed frequencies of instabilities and those measured by Lehr are achieved. No computation of the steady case is performed.

Shang et al. (1995) compute Lehr's M=6.46 case using the FDNS code (Chen et al., 1993), a pressure based finite difference code using the TVD scheme of Chakravarthy and Osher (1985). An operator-splitting scheme is used where the chemical kinetics source terms are integrated implicitly with an ODE solver in a predictor step and then coupled with the fluid dynamics in a corrector step (Rhie et al., 1993). The M=6.46 case is computed on a

uniform (87x97) and adapted grid (44x49) using a 7-step mechanism, presented in Table 2.2, based on the 18–step mechanism by Drummond et al. (1986) presented in Table 2.5. This mechanism is also documented in other work by Drummond (1988, 1990). Various interpolation techniques for defining the species concentrations in the predictor step are evaluated. Good comparisons with experimental results are achieved when either an adapted grid or a high order interpolation is used. These interpolation techniques are discussed in detail later and are evaluated in the current study.

Matsuo and Fujii (1995) compute unsteady cases using the conditions from experiments of Lehr for M=4.79. The same solution scheme of Matsuo et al. (1993) and a 2-step reaction model similar to that of Matsuo and Fujiwara (1993) are used. The 19-step mechanism (Matsuo et al., 1993) is used to perform a time integration of a reduced equation for the species conservation with no convection or diffusion. Different activation energies for the exothermic reaction of the 2-step mechanism are evaluated to generate different heat release rates or time of reaction. Results show the reaction time directly impacts the flowfield. Of the three activation energies evaluated, the one with a slow and the one with a medium heat release rate generate periodic unsteady results. A rapid release (E_a=0) produces a larger, more random disturbance.

Matsuo and Fujii (1996a) perform computations using the experimental conditions of Lehr (1972) and Ruegg and Dorsey (1962). A grid resolution of 401x401 is used to represent a quarter sphere domain and the 19-step mechanism used by Matsuo et al. (1993) is used. The pressure, temperature and velocities of the experiments are used but the diameter of the projectile is altered to generate steady, low frequency unsteady, and high frequency unsteady cases. A zero-dimension time integration of the governing equations is used as in Matsuo and Fujii (1995) to determine correlation between a defined Damköhler parameter and the resulting combustion situation. The integration uses the conditions along the stagnation line and assumes internal energy and total density are constant. This results in a

temporal profile depicted in Figure 2.3. The definition used for the Damköhler parameter is

$$\mathcal{D} = t_f/t_c$$
$$= [d/a_2]/\left[T_2/(dT/dt)_{max}\right] \tag{2.3}$$

where d is the projectile diameter and the quantities with subscript 2 denote values behind the shock. Based on their results, a critical value of $\mathcal{D} = 80$ is defined below which the unsteadiness is of a high frequency and above which it is a low frequency instability. No universal parameter to classify steady as well as unsteady cases is found. Such classification may require using the parameter defined in Matsuo and Fujii (1996a) as well as the critical parameter of V_P/V_D as determined by Lehr (1972) where V_P is the projectile speed and V_D is the detonation velocity of the mixture.

Matsuo and Fujii (1996b) compute unsteady cases from experiments of Ruegg and Dorsey (1962). The 19-step mechanism used by Matsuo et al. (1993) is employed and the governing equations are solved explicitly with the chemical reaction source term treated in
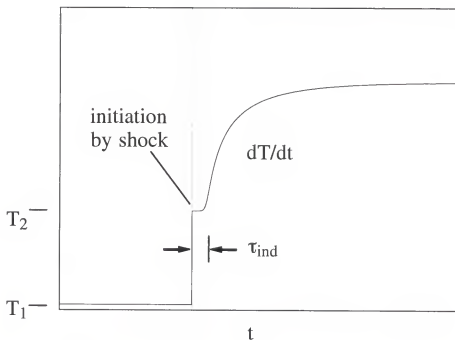

Figure 2.3.   Depiction of the temporal profile from a time integration of the governing equations using the conditions behind the shock on the stagnation line.

a linearly point-implicit manner. Yee's non-MUSCL TVD upwind explicit scheme is used on a 601x601 grid over a quarter-sphere domain. Results from grids of 201x301, 401x401, and 801x801 showed similar flow features. No direct comparison to experimental results is presented but conclusions as to the mechanisms causing the instabilities are made.

As is clear by the review here, the steady and unsteady shock-induced combustion scenarios captured by Lehr have been used in many computational studies. The current study computes the case at M=6.46 in a stoichiometric mixture of hydrogen and air. Therefore, those previous studies which have computed this same case are summarized in Table 2.8. Included in this summary are the particular fluid dynamics model and reaction model used as well as the grid resolution employed. Also, a depiction of the flow domain computed and resulting fronts are given. These images have been generated using the computed density field presented in each reference and orientating a line depicting the shock and energy release fronts based on this data. It is clear that those computations which do not cover a substantial portion of the projectile flow domain do not provide enough information to judge the accuracy of the computation. Therefore, the current study computes the entire length of the projectile as depicted in Figure 2.4 which is a larger domain than any of the previous computations. Also denoted in Figure 2.4 are the domains used in earlier computational studies in which the M=6.46 steady combustion case has been simulated. The utility of the larger domain is to be evident later.

2.3 Summary

As detailed here, the shock-induced combustion problem experimentally studied by Lehr (1972) and computationally studied by several investigators is to be used as an initial problem in developing the needed models for simulating the munition concepts discussed earlier. As is evident in the review, both the phenomenology of the various models and the numerical aspects are key in determining the accuracy of a simulation for this class of problems. For example, the chemical time scales of induction and reaction time are found to be key. However, this trend in the physical and chemical processes is only detectable if

Table 2.8. Summary of previous computational studies into steady shock-induced combustion.

Lehr (1972) Experiments	
Yungster et al. (1989) Mechanism : 8-step, Table 2.4 Grid : 42x44 Scheme : Fully implicit	
Lee and Deiwert (1989) Mechanism : 8-step, Table 2.4 Grid : 57x44 Scheme : Fully implicit	
Wilson and MacCormack (1990) Mechanism : 32-step, Table 2.7 Grid : 321x65 adapted Scheme : Fully implicit	
Ahuja and Tiwari (1993) Mechanism : 18-step, Table 2.5 Grid : 197x152 Scheme : MacCormack	
Sussman (1993) Mechanism : 19-step,Table 2.6 Grid : 44x49 Scheme : Explicit-Implicit Notes : Comparison improves with adapted grid.	
Wilson and Sussman (1993) Mechanism : 32-step, Table 2.7 Grid : 52x52 Scheme : Explicit-Implicit Notes : Solve logarithmic form of equations.	
Shang et al. (1995) Mechanism : 7-step, Table 2.2 Grid : 87x97 Scheme : Explicit-Implicit Notes : Comparison improves with extapolation scheme.	

(1) Extent of domain used by
      Yunster et al. (1989)
      Lee and Deiwert (1989)
      Ahuja and Tiwari (1993)

(2) Extent of domain used by
      Wilson and MacCormack (1990)
      Sussman (1993)
      Wilson and Sussman (1993)
      Shang et al. (1995)

(3) Extent of domain used
      in current study
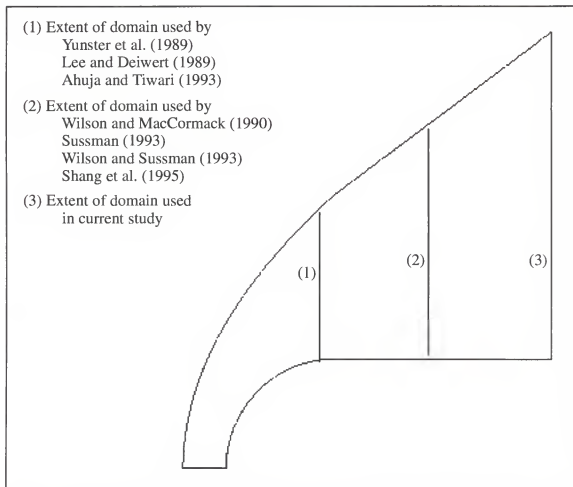
Figure 2.4. Computational domain used in previous investigations and throughout current study.

an adequate spatial discretization and reaction model is used. In the current study, not only are the computations compared to experiments, but the change in the dependent variables as a result of alternative models is used to help quantify the roles of the individual models on the accuracy of the complete computational tool. This not only aids in determining the impact these aspects have on the computation but also helps quantify the phenomenological and numerical aspects involved in solving a class of problems such as the fuel cell scenario.

This study uses the steady combustion case shown in Figure 2.2 to assess the aspects of modeling high-speed reacting flows. If the conditions for M=6.46 are used in the Damköhler parameter definition of Matsuo and Fujii (1996a), Eqn. (2.3), a value of 18 is calculated. This supports the use of this flow scenario to study the computation of reacting

flows where $\mathfrak{D} = O(1)$. As mentioned, the optical distortion in the image raises some concerns in a one-to-one comparison between the computations and image. However, instead of re-interpreting the image, the locations denoted in Figure 2.2 are used as in the case of previous investigations. It should also be noted that the experimental data is not symmetric about the stagnation line which suggests the projectile had some slight angle of attack during its flight. Results for the steady shock-induced combustion case are discussed following the description of the computational models developed here.

CHAPTER 3

GOVERNING EQUATIONS AND NUMERICAL TECHNIQUES

In this chapter the governing equations and various numerical techniques needed to solve the current class of problems are detailed. After the presentation of the governing equations, the individual approaches are discussed. For each model there are various options as to the particular phenomenological and numerical form. Where appropriate these options are discussed.

3.1 Governing Equations

The governing equations for the current problem are the axisymmetric form of the Navier-Stokes equations with appropriate source terms. The integral form of the governing equations is

$$\frac{\partial}{\partial t} \int_{\mathscr{V}} Q \ d\mathscr{V} + \int_{S} \vec{F} \cdot d\vec{S} = \int_{\mathscr{V}} \Omega \ d\mathscr{V} \tag{3.1}$$

where Q is the dependent variables in volume $\mathscr{V}$, F is the flux of those variables across the surface (S) which defines the volume $\mathscr{V}$ and Ω is any source term per unit volume for the dependent variables. The flux, F, is a non-linear function of the dependent variables Q. The governing equations once discretized for a general curvilinear coordinate system are

$$\frac{\partial \ J \ Q}{\partial t} + \frac{\partial \ J \ (F_I - F_V)}{\partial \xi} + \frac{\partial \ J \ (G_I - G_V)}{\partial \eta} + J \ (H_I - H_V) = J \ \Omega \tag{3.2}$$

where the dependent variables are

$$Q = \left[\varrho, \varrho u, \varrho v, \varrho E, \varrho \alpha_1, ..., \varrho \alpha_{NS-1} \right]^T . \tag{3.3}$$

The variables ϱ, u, v, and E are respectively the density, x component of velocity, y component of velocity, and energy. Also, α_i is the mass fraction of ith species with the fluid being defined by NS total species. Note that the mass fraction of the NSth species is not explicitly modeled since the total density is included and the relationship $\varrho = \sum_{i=1}^{NS} \varrho\alpha_i$ holds. Another modeling option is to not solve an equation for total mass but to solve an additional species conservation equation for the NSth species and calculate the total mass using the summation given above. With the addition of the relationship between the individual species densities and the total mass, both implementations require attention to numerical round-off issues. This is evident in previous investigations such as the work of Sussman (1993) and Wilson and Sussman (1993) in which it is noted that species densities can sometimes become negative due to numerical errors and that limiters must be used.

In the curvilinear directions ξ and η, the inviscid flux vectors are

$$F_I = \begin{bmatrix} \varrho U \\ \varrho uU + \xi_x P \\ \varrho vU + \xi_y P \\ U(\varrho E + P) \\ \varrho\alpha_1 U \\ \vdots \\ \varrho\alpha_{NS-1} U \end{bmatrix}, \quad G_I = \begin{bmatrix} \varrho V \\ \varrho uV + \eta_x P \\ \varrho vV + \eta_y P \\ V(\varrho E + P) \\ \varrho\alpha_1 V \\ \vdots \\ \varrho\alpha_{NS-1} V \end{bmatrix} \qquad (3.4)$$

where P is pressure, and the viscous flux vectors are

$$F_V = \begin{bmatrix} 0 \\ \xi_x\tau_{xx} + \xi_y\tau_{xy} \\ \xi_x\tau_{xy} + \xi_y\tau_{yy} \\ \xi_x\Pi_x + \xi_y\Pi_y \\ -\varrho\alpha_1\hat{U}_1 \\ \vdots \\ -\varrho\alpha_{NS-1}\hat{U}_{NS-1} \end{bmatrix}, \quad G_V = \begin{bmatrix} 0 \\ \eta_x\tau_{xx} + \eta_y\tau_{xy} \\ \eta_x\tau_{xy} + \eta_y\tau_{yy} \\ \eta_x\Pi_x + \eta_y\Pi_y \\ -\varrho\alpha_1\hat{V}_1 \\ \vdots \\ -\varrho\alpha_{NS-1}\hat{V}_{NS-1} \end{bmatrix}. \qquad (3.5)$$

The third dimension is incorporated using the axisymmetric terms

$$H_I = \frac{1}{y}\begin{bmatrix} \varrho v \\ \varrho u v \\ \varrho v^2 \\ v(\varrho E + P) \\ \varrho \alpha_1 v \\ \vdots \\ \varrho \alpha_{NS-1} v \end{bmatrix}, \quad H_V = \frac{1}{y}\begin{bmatrix} 0 \\ \tau_{xy} \\ \tau_{yy} - \tau_{\theta\theta} \\ \Pi_y \\ -\varrho\alpha_1\hat{v}_1 \\ \vdots \\ -\varrho\alpha_{NS-1}\hat{v}_{NS-1} \end{bmatrix}, \qquad (3.6)$$

where y is the distance from the line of symmetry and the vector of chemical reaction source terms is

$$\Omega = \begin{bmatrix} 0, 0, 0, 0, \dot{\omega}_1, ..., \dot{\omega}_{NS-1} \end{bmatrix}^T . \qquad (3.7)$$

The grid Jacobian J, an indication of the cell volume, and the contravariant velocities are defined as

$$\begin{aligned} J &= x_\xi y_\eta - x_\eta y_\xi \\ U &= \xi_x u + \xi_y v \\ V &= \eta_x u + \eta_y v \end{aligned} . \qquad (3.8)$$

where

$$\begin{aligned} \xi_x &= \frac{y_\eta}{J} , \quad \xi_y = \frac{-x_\eta}{J} \\ \eta_x &= \frac{-y_\xi}{J} , \quad \eta_y = \frac{x_\xi}{J} . \end{aligned} \qquad (3.9)$$

The components of the viscous flux vectors are defined as

$$\begin{aligned} \Pi_x &= u\tau_{xx} + v\tau_{xy} - q_x \\ \Pi_y &= u\tau_{xy} + v\tau_{yy} - q_y \\ \tau_{xx} &= 2\mu\frac{\partial u}{\partial x} + \lambda\left(\frac{\partial v}{\partial y} + \frac{\partial u}{\partial x} + \frac{v}{y}\right) \\ \tau_{yy} &= 2\mu\frac{\partial v}{\partial y} + \lambda\left(\frac{\partial v}{\partial y} + \frac{\partial u}{\partial x} + \frac{v}{y}\right) \\ \tau_{xy} &= \mu\left(\frac{\partial v}{\partial x} + \frac{\partial u}{\partial y}\right) \\ \tau_{\theta\theta} &= 2\mu\left(\frac{v}{y}\right) + \lambda\left(\frac{\partial v}{\partial y} + \frac{\partial u}{\partial x} + \frac{v}{y}\right) . \end{aligned} \qquad (3.10)$$

where the bulk viscosity is represented using Stokes' hypothesis, $\lambda = -\frac{2}{3}\mu$. The heat flux components are

$$q_x = -k\frac{\partial T}{\partial x} + \varrho \sum_{i=1}^{NS} h_i(\alpha_i \hat{u}_i), \qquad q_y = -k\frac{\partial T}{\partial y} + \varrho \sum_{i=1}^{NS} h_i(\alpha_i \hat{v}_i) \qquad (3.11)$$

where k is the thermal conductivity and $\alpha_i \hat{u}_i$ and $\alpha_i \hat{v}_i$ are the diffusion velocities defined in the next section.

3.1.1 Molecular Diffusion

The vector components $\hat{U}_i$, $\hat{V}_i$ are the contravariant diffusion velocities for species i and are represented using Fick's law as described by Anderson (1989), and Libby and Williams (1994). The exact form of the modeled terms are

$$\hat{U}_i = \xi_x \hat{u}_i + \xi_y \hat{v}_i, \quad \hat{V}_i = \eta_x \hat{u}_i + \eta_y \hat{v}_i$$
$$\alpha_i \hat{u}_i = -D_i \frac{\partial \alpha_i}{\partial x}, \quad \alpha_i \hat{v}_i = -D_i \frac{\partial \alpha_i}{\partial y} \qquad (3.12)$$

The use of Fick's law is made possible by some simplifying assumptions as to the molecular diffusivity of individual species. A more exact representation of the diffusion of a single species i in a mixture composed of NS species is to calculate the diffusivity of the species i as a function of its diffusivity in each of the other species. One level from this in simplification is to define a background gas or the gas which comprises the majority of the mixture. This allows the diffusivity of each species in the predominant gas to be calculated and used for D_i. For example, combustion problems involving hydrogen and air typically contain a large amount of nitrogen which can be defined as the background gas. The next level in simplification is to assume a single diffusion coefficient such that $D_i=D$ for all species, and that the binary diffusion can be related to the viscosity using the Schmidt number,

$$Sc = \frac{\mu}{\varrho D} \qquad . \qquad (3.13)$$

This simplification, used in the current study, has proven reliable in many computational studies and is considered acceptable when all the species involved have approximately the same molecular weight. The only concern in the context of the present study is the hydrogen involved given its molecular weight is one order of magnitude less than the other species. However, this simplification is employed given the predominance of the other transport mechanisms for the species in the current flow scenario and considering the reduction in the computational requirement. Also, in the context of diffusion itself, the molecular diffusivity is secondary to the turbulent enhancement which is discussed later.

3.2 Equation of State and Temperature

The equation of state used in the current computations is derived by assuming the ideal gas equation is valid for each individual species and has the form (Anderson, 1989)

$$P = \varrho R_u T \sum_{i=1}^{NS} \frac{\alpha_i}{M_i} \tag{3.14}$$

where R_u is the Universal Gas Constant and M_i is the molecular weight of species i. There are flows for which an alternate equation of state is more applicable and from a computational model standpoint, such alternate equations simply require an alternate definition of terms for which the derivative of pressure with respect to the conserved variables are needed. These modeling aspects are presented in a later section.

The temperature during the calculations must be extracted from the internal energy using the relationship

$$e = E - \frac{1}{2}\vec{u}^2 = \sum_{i=1}^{NS} \alpha_i h_i - \frac{P}{\varrho}$$

$$h_i = h_{f_i}{}^o + \int_{T_R}^{T} Cp_i dT \tag{3.15}$$

where T_R is the reference temperature and $h_{f_i}{}^o$ the heat of formation of species i at T_R. The specific heat, Cp_i, of each species is a known function of temperature and is available from various references such as the JANNAF data (Stull and Prophet, 1971). The dependence of

Cp_i on temperature can be represented in various forms ranging from a constant up to a high order polynomial. In the shock-induced combustion computations presented here, a third order polynomial of the form

$$Cp_i = c_1 + c_2T + c_3T^2 + c_4T^3 \tag{3.16}$$

is used. The coefficients have been determined by fitting curves to the JANNAF data up to 6000K and are given in Table 3.1. Higher order polynomials have been used by previous

Table 3.1. Coefficients used to calculate specific heats for the various species.

n	c_1	c_2	c_3	c_4	h_f^o
O_2	6.72433	1.75132×10^{-3}	-3.35085×10^{-7}	2.40485×10^{-11}	0.
H_2	6.18833	1.28193×10^{-3}	-1.59252×10^{-7}	9.05493×10^{-12}	0.
OH	6.96378	5.90649×10^{-4}	2.75234×10^{-8}	-1.03921×10^{-11}	9.432
H_2O	6.9803	3.6993×10^{-3}	-6.55318×10^{-7}	4.07621×10^{-11}	−57.798
O	5.25211	-2.0219×10^{-4}	3.79786×10^{-8}	0	59.559
H	4.968	0.	0.	0	52.1
HO_2	7.44933	7.3918×10^{-3}	-2.8673×10^{-6}	3.955×10^{-10}	5.
H_2O_2	6.6606	1.49214×10^{-2}	-7.7563×10^{-6}	1.3478×10^{-9}	−32.53
N_2	6.51307	1.65586×10^{-3}	-3.74607×10^{-7}	2.8942×10^{-11}	0.

Cp_n in cal / (mole K) h_f^o in kcal / mole $T_R = 298$ K

investigators but here, the third-order has been found to provide a good match using a single set of constants across the temperature range. Given this representation of specific heats, an iterative Newton-Raphson procedure must be used to extract the temperature in each cell at each time step as detailed by Molvik and Merkle (1989). The procedure solves the equation

$$e^{m+1} = e^m + \left(\frac{\partial e}{\partial T}\right)^m \Delta T \tag{3.17}$$

where m denotes the iteration step. The initial guess for the temperature in each cell at a given time step is simply the temperature at the previous time step and convergence is typically achieved in only a few iterations if an over-relaxation scheme is used.

Even though convergence is typically rather fast, it is clear to see that for a computation with a larger number of computational cells, this added aspect for reacting flows and for that matter high temperature flows can become costly. Therefore, for some

applications a lower form for Cp_i is worth using. In fact, if a linear representation for dependence of specific heat on temperature is used, the temperature can be calculated by solving a simple algebraic equation with no iteration. This representation enables the aspect of temperature dependence to be included with no added computational time. However, before using such a scheme, attention should be paid to the temperature range over which the computation is expected to vary to ensure the constants used best match this regime.

3.3 Thermal Conductivity and Viscosity

For the current study, it is assumed that the thermal conductivity can be determined by specifying a Prandtl number where

$$Pr = \frac{\mu Cp}{k} \ . \tag{3.18}$$

This as the case with the diffusivity is a simplification which has proven applicable to the class of flows modeled here. Note, the Schmidt and Prandtl number are related through the Lewis number ($Le = Sc/Pr$) which is often near unity. In the current study $Le = 1$ is assumed and the Prandtl number is set to .72. We now have the binary diffusion coefficient and the thermal conductivity related to the viscosity of the mixture by a constant of order one.

The viscosity of the mixture is modeled as a function of temperature and the species composition using Sutherland's law as described by White (1974),

$$\frac{\mu_i}{\mu_{oi}} = \left(\frac{T}{T_o}\right)^{1.5} \frac{T_{oi} + S_i}{T + S_i} \ , \tag{3.19}$$

and Wilke's formula

$$\mu = \sum_{i=1}^{NS} \frac{X_i \mu_i}{\sum_{j=1}^{NS} X_j \phi_{ij}} \ , \qquad \phi_{ij} = \left[1 + \left(\frac{\mu_i}{\mu_j}\right)^{\frac{1}{2}} \left(\frac{M_j}{M_i}\right)^{\frac{1}{4}}\right]^2 \left[8\left(1 + \frac{M_i}{M_j}\right)\right]^{-\frac{1}{2}} \ . \tag{3.20}$$

where X_i is the molecular concentration of species i and T_{oi} and S_i are constants. The constants for use in Eqn. (3.19) are given in Table 3.2. One of the requirements for the fluid mechanics model is to limit the numerical errors in the models of quantities such as the

Table 3.2. Coefficients used to calculate viscosity for the various species.

n	μ_0 (Ns/m²)	T_0 (K)	S (K)
O_2	1.919×10^{-5}	273	139
H_2	8.411×10^{-6}	273	97
H_2O	1.120×10^{-5}	350	1064
N_2	1.663×10^{-5}	273	107

diffusion of species and heat. Given the fact that both these quantities are related to the molecular viscosity with an order one constant, it is reasonable to conclude that the numerical errors in these two quantities are of the same order as numerical errors in molecular viscosity. The apparent errors in viscosity for typical computational models are not a function of the phenomenological model such as Eqn. (3.20) but are a result of numerical viscosity. Numerical viscosity is a direct function of the numerical scheme used in representing the governing equations. The particular scheme used in the current study is described next and the issue of numerical viscosity is addressed in that context. However, it is safe to assume that if the numerical viscosity is minimized, so will be the numerical errors in diffusion and conductivity.

3.4 Flux Vector Splitting Scheme

For the solution of compressible flows, the most popular schemes for representing the inviscid fluxes are flux difference and flux vector splitting. These upwind schemes are attractive due to their ability to minimize numerical viscosity. A review of these various schemes for multi-species flows is provided in the work of Montagne et al. (1987), Glaister (1988), Cinnella (1989), Grossman and Cinnella (1990), Shuen et al. (1990) and Liou et al. (1990). Here the scheme used to define the inviscid numerical fluxes is the Steger-Warming flux vector splitting (Steger and Warming, 1981) which has been extended to model multi-species flows by Liou et al. (1990). The flux vector splitting algorithm decomposes

the inviscid fluxes into components based on the eigenvalues of the Jacobian $A_I = \dfrac{\partial F_I}{\partial Q}$ and likewise for G_I. The split fluxes take the form

$$K^{\pm} = \lambda_1^{\pm} K_1 + \lambda_2^{\pm} K_2 + \lambda_3^{\pm} K_3 \qquad (3.21)$$

where

$$K_1 = \frac{\gamma - 1}{\gamma} \varrho \begin{bmatrix} \varrho \\ \varrho u \\ \varrho v \\ \varrho \left(h_t - \dfrac{c^2}{\gamma - 1} \right) \\ \varrho \alpha_1 \\ \vdots \\ \varrho \alpha_{NS-1} \end{bmatrix}, \quad K_{2,3} = \frac{1}{2\gamma} \begin{bmatrix} \varrho \\ \varrho \left(u \pm \bar{k}_x c \right) \\ \varrho \left(v \pm \bar{k}_y c \right) \\ \varrho \left(h_t \pm \theta_k c \right) \\ \varrho \alpha_1 \\ \vdots \\ \varrho \alpha_{NS-1} \end{bmatrix} \qquad (3.22)$$

with the eigenvalues being

$$\begin{aligned} \lambda_k^{\pm} &= \tfrac{1}{2} \left(\lambda_k \pm |\lambda_k| \right) \\ \lambda_1 &= \beta_k \\ \lambda_2 &= \beta_k + c|\nabla k| \\ \lambda_3 &= \beta_k - c|\nabla k| \end{aligned} \qquad (3.23)$$

where

$$\begin{aligned} \beta_k &= k_x u + k_y v \ , \quad \theta_k = \bar{k}_x u + \bar{k}_y v \\ \bar{k}_x &= \frac{k_x}{|\nabla k|} \ , \quad \bar{k}_y = \frac{k_y}{|\nabla k|} \ , \quad |\nabla k| = \sqrt{k_x^2 + k_y^2} \quad . \end{aligned} \qquad (3.24)$$

The above formulation gives $K = F_I$ when $k = \xi$ and $K = G_I$ when $k = \eta$. For the multi-species chemically reacting flow, c is the frozen speed of sound and γ is the effective specific heat ratio. The calculation of c is detailed in the Appendix.

In the finite volume formulation, the fluxes are evaluated at the cell faces and are either first or second-order spatial representations. For the class of flows to be solved here, a second-order scheme is desirable to limit the numerical viscosity. The flux at the face is a function of the states in the neighboring cells,

$$\left(F_I \right)_{i+\frac{1}{2}, j} = F_I^+ \left(Q_{i+\frac{1}{2}, j}^L \right) + F_I^- \left(Q_{i+\frac{1}{2}, j}^R \right) \qquad (3.25)$$

If a first-order spatial representation is used, then $Q^L_{i+\frac{1}{2},j} = Q_{i,j}$, $Q^R_{i+\frac{1}{2},j} = Q_{i+1,j}$. To achieve second-order accuracy, a MUSCL approach described by Shuen (1992) is used in which cell-center values are extrapolated to the interfaces. Also, to guard against the interpolation introducing any nonphysical extrema into the field in the region of large gradients, a limiter must be used. The formula for the neighboring states takes the form

$$
\begin{aligned}
Q^L_{i+\frac{1}{2},j} &= Q_{i,j} + \Phi^-_{i+\frac{1}{2},j} \\
Q^R_{i+\frac{1}{2},j} &= Q_{i+1,j} - \Phi^+_{i+\frac{1}{2},j}
\end{aligned}
\tag{3.26}
$$

where the limiting function is

$$
\begin{aligned}
\Phi^+_{i+\frac{1}{2},j} &= \frac{\ell_{i+1,j}}{2} \ \text{minmod}\left[\Delta Q^+_{i+1,j}, \Delta Q^-_{i+1,j}\right] \\
\Phi^-_{i+\frac{1}{2},j} &= \frac{\ell_{i,j}}{2} \ \text{minmod}\left[\Delta Q^-_{i,j}, \Delta Q^+_{i,j}\right]
\end{aligned}
\tag{3.27}
$$

with

$$
\begin{aligned}
\Delta Q^+_{i,j} &= \frac{2\left(Q_{i+1,j} - Q_{i,j}\right)}{\ell_{i+1,j} + \ell_{i,j}} \\
\Delta Q^-_{i,j} &= \frac{2\left(Q_{i,j} - Q_{i-1,j}\right)}{\ell_{i,j} + \ell_{i-1,j}}
\end{aligned}
\tag{3.28}
$$

Various limiters can be used with this implementation but here the minmod limiter is used where

$$
\text{minmod } [X, Y] = \text{sign}(X) \ \max[0., \min(|X|, Y\text{sign}(X))] \quad . \tag{3.29}
$$

Note $\ell_{i,j}$ is the cell-length to provide weighting for nonuniform grid spacing. The same extrapolation procedure is carried out for the fluxes in η and can be performed on either the dependent or primitive variables. Previous investigations by Shuen (1992) have shown that using primitive variables gives better performance for flows with strong shocks and this is the method used here.

Note, the second-order accuracy is achieved by the assumption that the field quantities vary linearly across a cell. Higher order schemes are achievable if a higher order

variation is assumed. However, in all cases, limiters must be used in conjunction with the higher order schemes to ensure against the introduction of any nonphysical extrema in regions of large gradients. The viscous fluxes are evaluated at the cell faces using central differencing and second order representations of the derivatives.

3.5 Chemical Reaction Source Term

The particular reaction mechanisms used in the current study have been discussed in the earlier literature review of shock-induced combustion simulations. The production of each species is incorporated into the governing equations by way of the source terms in Eqn. (3.7). This source term is calculated using the finite rate chemistry model described here. The reaction between hydrogen and oxygen which drives the shock-induced combustion must be modeled by a specific number of reactions (NR) using the form

$$\sum_{j=1}^{NS} v_{ij}' X_j \underset{k_{bi}}{\overset{k_{fi}}{\rightleftarrows}} \sum_{j=1}^{NS} v_{ij}'' X_j \ , \ i = 1, \ldots, NR \tag{3.30}$$
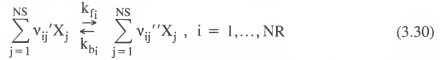
where v_{ij}' and v_{ij}'' are the stoichiometric coefficients for species j in reaction i, and X_j is the molecular concentration of species j. The parameters k_{f_i} and k_{b_i} are, respectively, the forward and backward reaction rate constants for the ith reaction and can be expressed as a function of temperature with the Arrhenius expression

$$k_i = A_i T^{b_i} exp\left[\frac{-E_{a_i}}{R_u T}\right] \tag{3.31}$$

where R_u is the universal gas constant, E_{a_i} is the activation energy and A_i and b_i constants for the ith reaction. The production rate of an individual species is calculated by summing the contribution due to each reaction

$$\dot{\omega}_j = M_j \sum_{i=1}^{NR} \left(v_{ij}'' - v_{ij}'\right) \times \left[k_{f_i} \prod_{n=1}^{NS} X_n^{v_{in}'} - k_{b_i} \prod_{n=1}^{NS} X_n^{v_{in}''}\right] . \tag{3.32}$$

The forward rate constants are available in various sources for most reactions of interest. The backward rate for a reaction is sometimes given explicitly using Arrhenius rates but is usually obtained using the equilibrium constant and the relationship

$$k_{e_i} = \frac{k_{f_i}}{k_{b_i}}. \tag{3.33}$$

The equilibrium constant can be expressed as a function of the stoichiometric coefficients and the Gibbs free energies (g_n) of the species in the reaction through the formula

$$k_{e_i} = [R_u T]^{-\sum_{n=1}^{NS}\left(v_{ni}'' - v_{ni}'\right)} \exp\left[\frac{-\Delta \mathring{g}}{R_u T}\right] \tag{3.34}$$

where

$$\Delta \mathring{g} = \sum_{n=1}^{NS}\left(v_{ni}'' - v_{ni}'\right) g_n . \tag{3.35}$$

The Gibbs free energy (g_n) associated with each species is given as a function of temperature, $g_n = g_n(T)$. Using the JANNAF data (Stull and Prophet, 1971), it is clear that a linear function of the form

$$g_n = g_{n_0} + g_{n_1}T \tag{3.36}$$

is adequate. The values of the constants for the species to be used throughout the current work are provided in Table 3.3 as well as their molecular weights. From a solution perspective, the chemical reaction source terms are numerically stiff and require special attention which is discussed later.

One note from the perspective of implementing a finite-rate reaction model as described here is needed. The necessary routines can be coded up to handle a generic reaction mechanism. This requires multiple do loops to calculate the source term as well as the Jacobian of the source term $\left(\partial \Omega / \partial Q\right)$ which is discussed later. This presents a problem when running such a code on a vector machine, or any machine for that matter, and literally orders of magnitude in computational time can be saved if the routine is coded up for a specific reaction mechanism. This is easily done if an analysis tool such as *Mathmatica* (Wolfram, 1988) is used to preprocess the needed equations and is well worth the time when large mechanisms or large grids are used.

Table 3.3. Molecular weights and coefficients used to calculate the Gibbs free energy for various species.

n	M_n	g_o	g_1
O_2	32.	0.	0.
H_2	2.016	0.	0.
OH	17.08	9.1646	-3.4×10^{-3}
H_2O	18.016	-59.29	1.35×10^{-3}
O	16.	60.464	-1.574×10^{-2}
H	1.008	53.3078	-1.396×10^{-2}
HO_2	33.008	4.195	1.194×10^{-2}
H_2O_2	34.016	-33.251	2.646×10^{-2}
N_2	28.016	0.	0.
N	14.008	114.407	-1.608×10^{-2}
NO	30.008	21.468	-2.94×10^{-3}
HNO	31.016	23.2391	1.173×10^{-2}
NO_2	46.008	7.738	1.514×10^{-2}

g_n in kcal/mole

3.6 Special Treatment For Chemical Length Scales

In the discussion of the flux-vector splitting scheme used in the current code, a detailed description is provided as to how to represent the numerical flux with a second-order spatial model. Such a model reduces the numerical dissipation of field quantities and improves the accuracy of the scheme. The second-order model is approximating the variation in variables across a cell as a linear function. As noted earlier, higher order schemes are achievable if a higher order variation is assumed. Second order schemes have proven to provide acceptable accuracy for simulations of compressible turbulent flows with little increase in computational requirements. However, this is due to the fact that the computational grid used in the simulations employ discretization of the appropriate size to capture the scales of the mean flow. With the addition of chemical reactions, the length scales which must be resolved can be orders of magnitude smaller. Of course one option is to construct the computational grid using a finer discretization. However, unless the location of key events such as the reaction front are known a priori this finer discretization must be used throughout a large portion of the flow field. An alternative is to employ a grid adaptation

technique which is only advantageous if it is closely coupled with the fluid dynamics model. Both these options present an increase in the computational requirements.

　　Other options of addressing the error associated with the small chemical length scales have been evaluated. Wilson and Sussman (1993) have used a transformed governing equation while Sussman (1993) and Shang et al. (1995) have tested source term modification techniques. These techniques take advantage of the known profiles of those species created in the chain-branching reactions. The variation of these species, such as OH, H, and O, is more logarithmic in nature. The transformed governing equation used by Wilson and Sussman (1993) is discussed briefly but attention is paid to the schemes which are an alteration only to the source term. Typically the source term is calculated using the cell averaged value for temperature and mass fractions, a piecewise representation. The modified treatment calculates the source term using an altered value for the mass fractions, $\omega_{i,j} = \dot{\omega}(\alpha_s)_{i,j}$. The scheme used by Shang et al. (1995) differs from that of Sussman (1993) so both are described here. All the source term treatments are an effort to address the fact that the cell averaged source term is not necessarily equal to the source term calculated based on the cell averaged dependent variables. This is due to the highly nonlinear nature of the Arrhenius source term.

3.6.1 Transformed Governing Equations

　　The modification option evaluated by Wilson and Sussman (1993) is a logarithmic transformation of the entire species conservation equation minus the diffusion term. The definition

$$\pi_n \equiv \varrho \ln\left(\frac{\varrho_n}{\varrho}\right) \equiv \varrho \ln(\alpha_n) \tag{3.37}$$

is used with the total mass conservation equation to specify the transformed equation for species n,

$$\frac{\partial}{\partial t}\pi_n + \frac{\partial}{\partial x_j}\pi_n u_j = \frac{\omega_n}{\alpha_n} \ . \tag{3.38}$$

In practice these transformed equations are solved in conjunction with conservation equations for the individual elements to ensure the conservation of mass. Solutions by Wilson and Sussman (1993) for the M=6.46 case of Lehr using this set of transformed equations produce good results on somewhat coarse grids. Wilson and Sussman state this formulation is no less robust than the conventional form of the equations but do warn against the added distortion at contact discontinuities between different gases. This could be key in non-premixed combustion scenarios. The computation time is cited to be 10–20 % more per time step above the standard scheme. Also, of interest is the error trend when this scheme is used on coarse grids. If the shock-induced combustion flow scenario is considered, the flow structure is such that behind the shock, a small induction zone can exist which lies between the temperature rise due to the shock and the temperature rise resulting from the reaction front. If the standard form of the governing equations are solved, a coarse grid results in a computed flow field such that the shock and reaction fronts are merged and the induction zone is not resolved. Sussman and Wilson (1991) have shown that a coarse grid used in conjunction with the transformed governing equations results in an overprediction of the induction zone. In short, the computed reaction front is positioned too far down stream. Therefore, even though the transformed governing equation method has shown promise when applied to the shock-induced combustion scenario (Wilson and Sussman, 1993), this grid dependence should be considered when analyzing the results.

3.6.2 Logarithmic Interpolation

The scheme of Shang et al. (1995) uses a logarithmic interpolation weighted by the mass flux into the cell and can be explained using the image of Figure 3.1. In this case the mass flux $(\dot{m})$ into cell (i,j) is from cell $(i-1,j)$ and $(i,j+1)$. The scheme first estimates the mass fraction at the cell faces using

$$
\begin{aligned}
\text{Log}\left(\alpha_{i-\frac{1}{2},j}\right) &= \frac{1}{2}\left[\text{Log}\left(\alpha_{i-1,j}\right) + \text{Log}\left(\alpha_{i,j}\right)\right] \\
\text{Log}\left(\alpha_{i,j+\frac{1}{2}}\right) &= \frac{1}{2}\left[\text{Log}\left(\alpha_{i,j+1}\right) + \text{Log}\left(\alpha_{i,j}\right)\right]
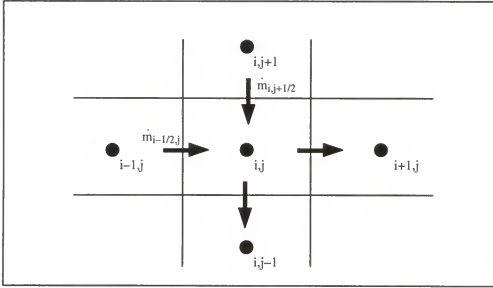\end{aligned}
\tag{3.39}
$$

Figure 3.1. Schematic of mass fraction interpolation scheme per Shang et al. (1995).

and then calculates the mass fraction to be used in the source term evaluation by

$$\alpha_s = \text{Exp}\left[\frac{\dot{m}_{i-\frac{1}{2},j}\text{Log}\left(\alpha_{i-\frac{1}{2},j}\right) + \dot{m}_{i,j+\frac{1}{2}}\text{Log}\left(\alpha_{i,j+\frac{1}{2}}\right)}{\dot{m}_{i-\frac{1}{2},j} + \dot{m}_{i,j+\frac{1}{2}}}\right] \tag{3.40}$$

where α represents each species mass fractions. The interpolations are a sum of all cell faces for which the mass flux is into the cell. In actual implementations, Log functions are singular when the mass fractions are zero. Therefore, after simple arithmetic, the interpolated value for the example case is simply

$$\alpha_s = \left[\left(\alpha_{i-1,j}\right)^{\dot{m}_{i-\frac{1}{2},j}}\left(\alpha_{i,j+1}\right)^{\dot{m}_{i,j+\frac{1}{2}}}\right]^{\frac{1}{2\left(\dot{m}_{i-\frac{1}{2},j} + \dot{m}_{i,j+\frac{1}{2}}\right)}} \left(\alpha_{i,j}\right)^{\frac{1}{2}}. \tag{3.41}$$

Shang et al. (1995) present both solutions of a one-dimensional auto-ignition case and the M=6.46 case captured by Lehr (1972). In the one-dimensional case, the modified source term treatment produced "exact" solutions using only about a fourth of the grid points required to achieve the same accuracy with the piecewise representation. This interpolation scheme also improves the comparison between the experimental data and the computed flow

field for the M=6.46 case. This is accomplished with no addition of grid cells or adaptation. These results are discussed further in the context of the results of the current study.

3.6.3 Error Estimation Based on One-Dimensional Model Equations

The source term modification proposed by Sussman (1993) is based on the analysis of a one-dimensional model problem of the governing equations. The analysis is summarized here for completeness. Consider the model problem

$$\frac{\partial Q}{\partial t} + u\frac{\partial Q}{\partial x} = kQ$$
$$Q(0, t) = Q_0$$

(3.42)

and when discretized using a first-order upwind scheme is

$$Q_i^{n+1} = Q_i^n - \frac{\Delta t}{\Delta x}u_i\left(Q_i^n - Q_{i-1}^n\right) + \Delta t\Omega_i^n$$

(3.43)

where the source term is

$$\Omega_i^n = \Omega\left(Q_i^n\right) = kQ_i^n \; .$$

(3.44)

Note, in Sussman's (1993) analysis, u is set to 1. The steady-state solution can be approximated by

$$Q(x) = Q_0 e^{kx/u}$$

(3.45)

and the source term by

$$\Omega(Q) = kQ$$

(3.46)

where $k = k_f$. The values of the discretized function and source term, using a constant spatial discretization, are

$$Q_i = Q_0 e^{k(i-1)\Delta x/u}$$
$$\Omega_i = kQ_0 e^{k(i-1)\Delta x/u} \; .$$

(3.47)

Therefore, the approximation of the spatial derivative of Q at point i, using first-order upwinding, is

$$D_i^- = Q_i^n - Q_{i-1}^n = Q_0 e^{k(i-1)\Delta x/u}\left[1 - e^{-k\Delta x/u}\right]\frac{1}{\Delta x/u} \; .$$

(3.48)

The error present in a steady-state solution of the model problem can be estimated by analyzing the ratio of this operator to the source term,

$$\frac{D_i^-}{\Omega_i} = \frac{\left[1 - e^{-k\Delta x/u}\right]}{k\Delta x/u} \quad .$$

(3.49)

Recall that k represents the reaction rate and $1/k$ is the characteristic time scale of the reaction. Therefore, $k\Delta x/u$ is the ratio of the actual chemical time scale to the fluid dynamic time scale, associated with the grid spacing, used in the computation. This is a cell Damköhler number, $\mathfrak{D}_{cfd}$. The variation of the ratio in Eqn. (3.49) with $k\Delta x/u$ is given in Figure 3.2. Both the figure and Eqn. (3.49) demonstrate that as $k\Delta x/u \rightarrow \infty$ the ratio
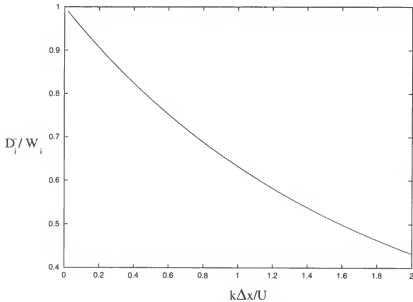

Figure 3.2.   Discretization error for Sussman's (1993) model problem.

D_i^-/Ω_i is asymptotically proportional to $\left[k\Delta x/u\right]^{-1}$. This relationship has direct implications to the solution of chemically reacting flows and demonstrates the expected trend. In a given flow scenario, the velocity is set by the solution as is the rate k, through the field variables and the reaction mechanism used. The advantage of adapting the grid to reduce Δx in regions of large k is obvious given the fact that the error changes exponentially with $k\Delta x/u$. However, the effectiveness of such adaptation is dependent on the magnitude

of k and it is clear for large k, Δx must be very close to zero to reduce the error. We next consider alternative ways of reducing the error introduced through the discretization of the exponentially varying function.

Sussman (1993) uses the information from the error analysis to propose a modification to the source term evaluation using a scaling factor f such that $\alpha_s = f \ \alpha_{i,j}$. In the context of the model problem,

$$\tilde{\Omega}(Q_i) = \Omega(fQ_i) = kfQ_i \tag{3.50}$$

where f is a scaling factor which gives $D_i^- / W_i = 1$ if

$$f = \frac{\left[1 - e^{-k\Delta x/u}\right]}{k\Delta x/u} \ . \tag{3.51}$$

In a general problem f is not known a priori because k is not a constant. Sussman (1993) estimates k using the exact solution of the model problem,

$$k \simeq -\frac{u}{\Delta x}\ln\left(\frac{Q_{i-1}^n}{Q_i^n}\right) \ . \tag{3.52}$$

Using this estimate, which is exact if Q is truly an exponential function in space, the scaling factor when using a first-order upwind scheme is

$$f = \frac{1 - r}{-\ln(r)} \ , \ r = Q_{i-1}^n / Q_i^n \tag{3.53}$$

and for a second-order upwind scheme, is

$$f = \frac{\frac{3}{2} - 2r + \frac{1}{2}r^2}{-\ln(r)} \ , \ r = Q_{i-1}^n / Q_i^n \ . \tag{3.54}$$

As presented by Sussman (1993), to achieve the exact solution of the model problem with this modified source term treatment and a first-order scheme requires only 1/8th the number of grid points if a piecewise treatment of the term is used with a second-order upwind scheme.

In applying this modification to a quasi-one-dimensional shock-induced combustion case for hydrogen-air, the modification is applied to only those species produced by the

chain-branching reactions. For application to two-dimensional flows, it is assumed the exponential variation occurs in the direction of the flow and k is estimated by

$$k \simeq - \frac{|\cos \theta|}{\Delta x} \ln(r_i) - \frac{|\sin \theta|}{\Delta y} \ln(r_j) \tag{3.55}$$

where

$$\cos \theta = \frac{u}{(u^2 + v^2)^{\frac{1}{2}}} \qquad \sin \theta = \frac{v}{(u^2 + v^2)^{\frac{1}{2}}} \ . \tag{3.56}$$

This results in a modification factor for use with second-order upwind schemes of

$$f = \frac{\frac{\cos \theta}{\Delta x} \left(\frac{3}{2} - 2r_i + \frac{1}{2} r_i^2 \right) + \frac{\sin \theta}{\Delta y} \left(\frac{3}{2} - 2r_j + \frac{1}{2} r_j^2 \right)}{- \frac{\cos \theta}{\Delta x} \ln(r_i) - \frac{\sin \theta}{\Delta y} \ln(r_j)} \tag{3.57}$$

where the parameters r_i and r_j are determined using upwinding,

$$r_i = \begin{cases} \varrho \alpha_{i-1,j} / \varrho \alpha_{i,j}, & u > 0; \\ \varrho \alpha_{i+1,j} / \varrho \alpha_{i,j}, & u < 0 \end{cases} \qquad r_j = \begin{cases} \varrho \alpha_{i,j-1} / \varrho \alpha_{i,j}, & v > 0; \\ \varrho \alpha_{i,j+1} / \varrho \alpha_{i,j}, & v < 0 \end{cases} \ . \tag{3.58}$$

A separate factor is calculated for each species α produced by the chain-branching reactions. To ensure the modification factor is bounded, the limits $r_i \leq 1$, $r_j \leq 1$ are imposed. Sussman (1993) demonstrated this technique for the M=6.46 case of Lehr but found the scheme did not produce results comparable to the experimental data unless an adapted grid is also used. These results are discussed in more detail later in conjunction with the current study.

Given the above discussion, it is of interest to compare the modification of Shang et al. (1995) in the same context. Beginning with Eqn. (3.41), and assuming the mass fractions in the neighboring cells enter the formula through a similar representation of k in the two dimensions as that used in Eqn. (3.52), we have

$$e^{-k\Delta x/u} = \frac{\alpha_{i-1,j}}{\alpha_{i,j}} \ , \ e^{-k\Delta y/v} = \frac{\alpha_{i,j+1}}{\alpha_{i,j}} \tag{3.59}$$

and after simple arithmetic, Eqn. (3.41) becomes

$$\alpha_s = \left[e^{-\dot{m}_{i-\frac{1}{2},j}k\Delta x/u} \; e^{-\dot{m}_{i,j+\frac{1}{2}}k\Delta y/v} \right]^{\overline{\frac{1}{2\left(\dot{m}_{i-\frac{1}{2},j} + \dot{m}_{i,j+\frac{1}{2}} \right)}}} \left(\alpha_{i,j} \right) \tag{3.60}$$

where v is used to represent the velocity in the second direction. For comparison purposes, consider the one-dimensional case as done by Sussman, we have $\Delta y=0$ and $\dot{m}_n = 0$. Therefore, the logarithmic extrapolation results in a scaling factor of

$$f = e^{-\frac{k}{2}\Delta x/u} \tag{3.61}$$

which at first looks quite different from that of Eqn (3.51) but as evident in Figure 3.3, when
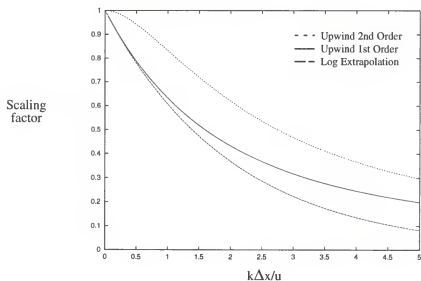

Figure 3.3.   Comparison of the scaling factors from the logarithmic extrapolation and error estimation.

plotted for a range of $k\Delta x/u$ is comparable to the scaling factor by Sussman (1993) for first-order upwind. Also presented in Figure 3.3 is the scaling factor for the second-order upwind scheme of Eqn. (3.54).

3.6.3.1 Global Order of Accuracy Analysis

        The scaling factor proposed by Sussman (1993) has been derived by analyzing the local error introduced by the piecewise representation of the source term. It is also enlightening to consider the global order of accuracy and the impact of this scaling on the

magnitude of the global error. The global order of accuracy is dependent on the accumulation of error at the locations upstream of the local computational stencil (Shyy, 1994) as depicted in Figure 3.4. This is particularly of interest in the current reactive flow problems since one
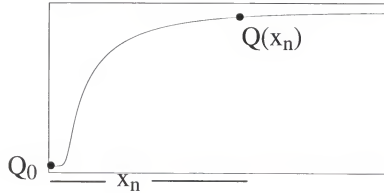

Figure 3.4. Depiction of region over which error accumulation affects the global error of accuracy.

of the key flow field features is the variation in mass fractions.

Consider the model problem, Eqn. (3.42), used by Sussman (1993) which has an exact solution for the steady-state case of the form

$$Q(x) = Q_0 e^{ax} \tag{3.62}$$

where $a = k/u$. Employing a first-order upwind difference operator with the piecewise source term representation, the difference equation used to represent the model differential equation is

$$\frac{q(x + h) - q(x)}{h} = a\ q(x) \tag{3.63}$$

where h is the grid spacing and for the current analysis constant spacing throughout the domain is assumed. The exact solution of the difference equation is

$$\begin{aligned} q_n &= (1 + ah)\ q_{n-1} \\ &= (1 + ah)\big[(1 + ah)q_{n-2}\big] \\ &= (1 + ah)^n\ q_0 \\ q_n &= (1 + ah)^{x_n/h}\ q_0 \end{aligned} \tag{3.64}$$

and to estimate the global error the solution of the difference equation is subtracted from the exact solution of the differential equation

$$\begin{aligned} E(x_n) &= Q(x_n) - q_n \\ &= Q_0 e^{ax_n} - (1 + ah)^{x_n/h} q_0 \; . \end{aligned} \tag{3.65}$$

Since the initial conditions for the difference equation are specified, $q_0 = Q_0$ and the leading order of the global error is dependent on $e^{ax_n} - (1 + ah)^{x_n/h}$. The second term can be expanded as

$$\begin{aligned} (1 + ah)^{x_n/h} &= \exp\left[\frac{x_n}{h} \text{Log}(1 + ah)\right] \\ &= \exp\left[\frac{x_n}{h}\left(ah - \frac{(ah)^2}{2} + O\!\left(h^3\right)\right)\right] \\ &= \exp\left[ax_n - \frac{a^2 x_n h}{2} + O\!\left(h^2\right)\right] \\ &= \exp(ax_n)\exp\left(\frac{a^2 x_n h}{2}\right)\exp\left(O\!\left(h^2\right)\right) \end{aligned} \tag{3.66}$$

where it has been assumed $ah < 1$ in the expansion of the logarithmic function. In implementation this may not be true but here the global order of accuracy, and specifically how the error decreases as h is reduced, is being assessed so the expansion is applicable. Using the expansion

$$e^x = 1 + x + x^2/2! + x^3/3! + \ldots$$

Eqn. (3.66) becomes

$$\begin{aligned} (1 + ah)^{x_n/h} &= \exp\left[1 - \frac{a^2 x_n h}{2} + O\!\left(h^2\right)\right] \\ &= e^{ax_n} - h\left(\frac{a^2 x_n}{2}\right)e^{ax_n} + O\!\left(h^2\right) \end{aligned} \tag{3.67}$$

and the global order of accuracy is

$$E(x_n) = Q_0\left[h\frac{a^2 x_n}{2}e^{ax_n} + O\!\left(h^2\right)\right] . \tag{3.68}$$

This results in a normalized error, when the piecewise source term is used, of

$$E_{norm}(x_n) = \frac{E(x_n)}{Q(x_n)} = O(h) \tag{3.69}$$

which is an indication of the error at locations far from the boundary. This error, an accumulation of errors across the region from where the boundary conditions are imposed to the point of interest, can be key in problems such as the current shock-induced combustion flows where features such as induction zones and reaction fronts are of interest. This is due to the fact that regions such as induction zones are areas over which quantities such as radicals are growing. Since factors such as the mass fraction of radicals directly impact the resulting chemical process, any error in their growth pattern introduce inconsistences between the simulated field and what is actually experienced.

When the scaling factor proposed by Sussman (1993) is used, the actual difference equation being solved is somewhat different from that of Eqn. (3.63) since the scaling factor is a function of the dependent variables. The exact form, using a first-order upwind scheme, is

$$\frac{q(x + h) - q(x)}{h} = a\, q(x) \left[\frac{1 - \frac{q(x)}{q(x+h)}}{-\,\text{Log}\!\left(\frac{q(x)}{q(x+h)}\right)} \right] \tag{3.70}$$

which can be simplified to

$$q_n \text{Log}\!\left(\frac{q_{n-1}}{q_n}\right) - q_{n-1}\text{Log}\!\left(\frac{q_{n-1}}{q_n}\right) + ah(q_n - q_{n-1}) = 0 \tag{3.71}$$

and further reduced to

$$\left(q_n - q_{n-1}\right)\!\left[\text{Log}\!\left(\frac{q_{n-1}}{q_n}\right) + ah\right] = 0 \tag{3.72}$$

which has two roots,

$$q_n = q_{n-1}\ ,\ \ q_n = e^{ah + \text{Log}(q_{n-1})}\ . \tag{3.73}$$

Dismissing the first root due to the nature of the problem being solved, the exact solution of the difference equation is

$$\begin{aligned}
q_n &= e^{ah} \, q_{n-1} \\
&= e^{ah}\left[e^{ah}q_{n-2}\right] \\
&= \left(e^{ah}\right)^n q_0 \\
q_n &= \left(e^{ah}\right)^{x_n/h} q_0
\end{aligned} \tag{3.74}$$

and when used to calculate the global error results in

$$E(x_n) = Q(x_n) - q_n = Q_0 e^{ax_n} - q_0 e^{ax_n} = 0 \tag{3.75}$$

given the fact the initial conditions for the difference equation are specified so $q_0 = Q_0$. Therefore, the exact solution of the difference equation being solved when the scaling factor is introduced matches the exact solution of the original differential equation. This infers the accumulation error when the scaling factor is included is minimized and is further reason to use the scaling factor in the shock-induced combustion computations to be performed here.

3.6.3.2 Current Application of Scaling Factor Scheme

In the current study the two scaling methods described above are compared by applying each to the solution of the shock-induced combustion flow. It is obvious by this point that the error is introduced in the solution of the problem through the representation of the spatial derivative. This is due to the fact that the mass fractions of the species in many cases vary exponentially over a region much smaller than the typical grid spacing. Therefore, the source term for a given cell calculated based on the cell average of the dependent variables is not equal to the cell average of the true source term. Given the use of the scaling schemes, it is worth assessing how close to the governing equations is the model problem used by Sussman (1993).

The species conservation equation can be reduced to

$$\frac{\partial \alpha}{\partial t} + U \frac{\partial \alpha}{\partial x} = \dot{\omega} \ . \tag{3.76}$$

using the continuity equation. In the actual governing equations the source term $\dot{\omega}$ is a function of all species involved in the reactions. Therefore the factor k in Sussman's model problem (Sussman, 1993) is an effective rate of production of α per concentration of α, or

the derivative of the source term with respect to the species α. This information is available in the form of the source term Jacobian, given in the Appendix. Alternate estimations for k may prove useful but here we use the form as proposed by Sussman (1993) to facilitate comparison to these earlier results.

In the documented scheme by Sussman (1993), the criterion for selecting the upwind direction in specifying the ratio of mass fractions, Eqn. (3.58), uses the Cartesian velocity components. It is not clear if this has been done simply for notation but would be very erroneous if Cartesian velocities are used in conjunction with a curvilinear grid. Therefore, here the contravariant velocities are used to determine the upwind directions. Also, the particular form of Eqn. (3.57) used by Sussman (1993) in the two-dimensional computations determines the error estimate using a weighted sum from the two curvilinear directions. However, the Cartesian velocities are used in the weighting which may introduce some inconsistencies. Therefore, the current study evaluates the scaling by Shang et al. (1995) and Sussman (1993), with curvilinear upwinding, and also evaluates the scaling factor in the form

$$
f = \frac{\tilde{m}_w\left(\frac{3}{2} - 2r_i + \frac{1}{2}r_i^2\right) + \tilde{m}_n\left(\frac{3}{2} - 2r_j + \frac{1}{2}r_j^2\right)}{-\tilde{m}_w \ln(r_i) - \tilde{m}_n \ln(r_j)}
$$

$$
\tilde{m}_w = \frac{\dot{m}_{i-\frac{1}{2},j}}{\sqrt{\dot{m}_{i-\frac{1}{2},j}^2 + \dot{m}_{i,j+\frac{1}{2}}^2}} \quad , \quad \tilde{m}_n = \frac{\dot{m}_{i,j+\frac{1}{2}}}{\sqrt{\dot{m}_{i-\frac{1}{2},j}^2 + \dot{m}_{i,j+\frac{1}{2}}^2}}
$$

(3.77)

where the components are as defined earlier and the flow scenario is that of Figure 3.1. The schemes of Shang et al. (1995), Sussman (1993) and the current scaling factor, Eqn. (3.77), based on Sussman's work (1993) are evaluated here and the results are presented later. When these scaling are used, the effective reaction rate is not just the change in the mass fraction over the distance between neighboring cells but a velocity scaling is included as detailed in the derivation using the model problem.

As is evident by the attention to both adaptive gridding techniques, transformed equations, and modified source term treatments, the additional scales introduced by the chemical reaction processes in the current problem set can not be ignored. Various studies have evaluated these three options for treating the problem and here the modified source term treatment is tested. This is done in part because if such a treatment proves worthwhile, it is easily integrated into the solution process. The scaling factor offers an attractive option to grid adaptation but the error estimation required is only as good as the estimate of the effective rate k. Given the behavior of the error as $k\Delta x/U$ increases, any errors in this estimate are heightened for large k.

3.6.4 Nonphysical Wave Speeds

LeVeque and Yee (1990) also document the problems associated with highly nonlinear source terms. In their study a model problem is used to study the behavior of the linear advection equation with a source term. Nonphysical wave speeds are noted for large Δt. The source of the nonphysical speeds is found to be solely a function of the presence of the source term since the conservative numerical methods used correctly reproduce the wave speed if no source term is present. LeVeque and Yee's (1990) analysis is summarized here. Consider the governing equation of the current reactive flow problems. If no source term is present, the numerical scheme is conservative if the summation over the domain results in the cancellation of the defined fluxes. In a word, for a finite volume scheme, the defined fluxes at the cell faces must balance. The addition of a source term results in a quantity that does not cancel when summed over the domain and therefore, if this term is incorrectly modeled, the accuracy in characteristics such as wave speed are reduced.

In the numerical model of both the model problem studied by LeVeque and Yee (1990) and the full set of governing equations to be solved for reacting flows, the source term is typically represented as a function of the cell averaged α, $\omega(\overline{\alpha_i})$. In the context of the integral form of the governing equations which is used to validate conservatism, this replaces the average value of the source term, $\overline{\omega}$, with a source term which is calculated base on an

average α. The discrepancy between these two is small for a smoothly varying α but in the case of reacting flows where sharp variations exist, the difference can be large. The conclusions of LeVeque and Yee (1990) on how to treat the occurrence are much the same as those already presented. First is the option of refining the grid which is not appealing as mentioned earlier. A second option proposed by LeVeque and Yee (1990) is to better represent the integral of the source term across a given cell. This requires a better model for the variation across the cell which is in the same line as the logarithmic variation approximations evaluated here.

3.7 Numerical Solution Methods

Many options exist for the integration and numerical solution of the governing equations. These options typically fall in the categories of explicit or implicit schemes. Problems including chemical reaction source terms as here normally require an implicit method for the treatment of the stiff source terms. This can be achieved in two ways. The first option is to solve the governing equations in a fully coupled manner which requires the derivatives of both the fluid dynamic and source terms with respect to the dependent variable vector, Q. These derivatives, Jacobian matrices, can be quite large in the case of a multi-species flow. The second option is a splitting method in which the fluid dynamic terms are treated explicitly and only the source terms are treated in an implicit manner. Both of these schemes are to be used in the current study so a description of each is provided here.

3.7.1 Fully-Implicit Formulation

As detailed in the description of the flux scheme, a second-order spatial accurate model is used. Likewise, it is advantageous to use a second-order temporal scheme as well. A detailed review of the fundamentals of achieving such a scheme is available in Hirsch (1990a, 1990b) and the current implementation follows that of Shuen (1992). A concise review is provided here.

The governing equation for the current problem, Eqn. (3.2), is of the form

$$\frac{dQ}{dt} = M(Q, t) \tag{3.78}$$

where M is a non-linear function of Q and represents the differential space operators and source terms of Eqn. (3.2). A one-step scheme for solving the system of equations is

$$Q^{n+1} - Q^n = \delta t \left[\zeta M^{n+1} + (1 - \zeta)M^n \right] \tag{3.79}$$

and when $\zeta = 1/2$ the scheme is second order in time. Since the whole purpose of solving the set of equations is to determine Q^{n+1}, the question is first how to represent $M^{n+1} = M(Q^{n+1})$. One option is to use a predictor and corrector approach which results in an explicit scheme. The second option is to linearize the non-linear term M^{n+1} which results in a fully implicit scheme. The term is linearized as

$$
\begin{aligned}
M^{n+1} &= M^n + \left(\frac{\partial M}{\partial t}\right)_n \delta t + O(\delta t^2) \\
&= M^n + \left(\frac{\partial M}{\partial Q}\right)_n \left(\frac{\partial Q}{\partial t}\right)_n \delta t + O(\delta t^2) \\
&= M^n + N^n \delta Q^n + O(\delta t^2)
\end{aligned}
\tag{3.80}
$$

where $\delta Q^n = Q^{n+1} - Q^n$ and the Jacobian, $N = \partial M / \partial Q$, has been introduced. Introducing the linearized terms the equation becomes

$$
\begin{aligned}
\delta Q &= \delta t \left[\zeta(M^n + N^n \delta Q) + (1 - \zeta)M^n \right] \\
&= \delta t \left[\zeta(N^n \delta Q) + M^n \right]
\end{aligned}
\tag{3.81}
$$

Using $\Delta t = \delta t / J$ and the definitions

$$
\begin{aligned}
F &= J(F_I + F_v) \\
G &= J(G_I + G_v) \\
H &= J(H_I + H_v) \\
S &= J\Omega
\end{aligned}
\tag{3.82}
$$

the governing equation, Eqn. (3.2) becomes

$$\left[I + \frac{1}{2}\Delta t \left(\delta_\xi A + \delta_\eta B + H' - S' \right) \right] \Delta Q = -\Delta t \left(\delta_\xi F + \delta_\eta G + H - S \right) \tag{3.83}$$

where δ_ξ and δ_η represent the spatial discretization in the two curvilinear directions, $A = \partial F/\partial Q$, $B = \partial G/\partial Q$, $H' = \partial H/\partial Q$, and $S' = \partial S/\partial Q$. Note, ζ has been set to 1/2 for second order accuracy. When implemented, the Jacobians of the viscous terms are neglected which has proven to save computational time with no negative impact on the solution process.

Introducing the flux vector splitting described previously, Eqn. (3.83) can be symbolically expressed as

$$[D + L + U]\, \Delta Q = -\, \Delta t\; R \qquad (3.84)$$

where the components of the implicit operator are

$$D = I + \frac{1}{2}\Delta t \left(A^+{}_{i,j} - A^-{}_{i,j} + B^+{}_{i,j} - B^-{}_{i,j} + H'{}_{i,j} - S'{}_{i,j} \right)$$
$$L = -\frac{1}{2}\Delta t \left(A^+{}_{i-1,j} + B^+{}_{i,j-1} \right) \qquad (3.85)$$
$$U = \frac{1}{2}\Delta t \left(A^-{}_{i+1,j} + B^-{}_{i,j+1} \right)$$

and the explicit operator is

$$R = \Delta t \left(F_{i+\frac{1}{2},j} - F_{i-\frac{1}{2},j} + G_{i,j+\frac{1}{2}} - G_{i,j-\frac{1}{2}} + H_{i,j} - S_{i,j} \right) \;. \qquad (3.86)$$

Due to the linearization, all the components of the implicit and explicit operator are evaluated at time level n. As detailed by Janus (1989), when solving unsteady flows, many times sub-iterations are used in the solution process to minimize the linearization error.

The Jacobian matrices of the split fluxes are exactly $A^\pm = \partial F^\pm/\partial Q$ but are approximated here as in previous studies (Shuen, 1992) using

$$A^\pm = T_\xi \Lambda_\xi^\pm T_\xi^{-1} \;. \qquad (3.87)$$

The matrix $\Lambda_\xi^\pm$ is a diagonal matrix composed of the eigenvalues $\lambda_\xi^\pm$ given in Eqn. (3.23). The matrix T_ξ is composed of the right eigenvectors of the matrix A, in columns, and T_ξ^{-1} the corresponding left eignevectors in rows. The eigenvectors are provided in the Appendix. The exact Jacobians are available in Janus et al. (1992).

Here the system of equations represented in Eqn. (3.84) is solved using a lower-upper (LU) approximate factorization scheme described by Shuen (1992) and Shuen and Yoon (1989) and based on the scheme developed by Jameson and Yoon (1987). The left-hand side of Eqn. (3.84) is approximately factored into the product of two operators

$$[D + L]D^{-1}[D + U] \; \Delta Q = - \Delta t \; R \qquad (3.88)$$

and when implemented can be solved in the sequence

$$\begin{aligned} [D + L]\Delta Q^* &= - \Delta t \; R \; , \\ [D + L]\Delta Q &= D\Delta Q^* \; , \\ Q^{n+1} &= Q^n + \Delta Q \; . \end{aligned} \qquad (3.89)$$

Various stability advantages of this solution scheme are detailed by Shuen (1992).

3.7.2 Explicit-Implicit Splitting Scheme

As mentioned, options for the solution method for the current problem range from fully implicit to fully explicit schemes. Implicit schemes are essential when solving problems with strong source terms as is the case here. However, explicit methods are attractive due to their reduced computational requirements. Also, there is some question as to the advantage of fully implicit schemes for this class of problems. For high-speed reacting flows, small temporal steps are used to either capture the unsteady nature of the flow or in light of the small time scales of the chemical processes.

The need for an implicit scheme for the treatment of the source terms and the efficiency of an explicit formulation can be met using the Strang splitting method described by Le Veque and Yee (1990). The scheme computes the dependent variables (Q) at the new time level (n+1) by performing various operations on the variables at the current time level (n). The splitting can be represented by

$$Q^{n+1} = S_\Omega(\Delta t/2) \; S_F(\Delta t) \; S_\Omega(\Delta t/2) \; Q^n \qquad (3.90)$$

where S_Ω represents the numerical solution operator for the source term and S_F the numerical solution operator for the fluid dynamics conservation equations. The Strang splitting has two features which make it very attractive for the current problem. First the

splitting maintains second-order accuracy which is needed to reduce the numerical dissipation of the important phenomena. The second feature is the fact that the splitting allows proven solution schemes for each aspect, the chemistry and fluid dynamics, to be easily integrated. Such a splitting may raise some concerns about capturing the coupling between the fluid dynamics and the chemical processes. However, as demonstrated in the combustion instability simulation work of Shyy et al (1993), this approach yields a very satisfactory treatment for the source terms.

As mentioned, in the splitting technique the fluid dynamics aspects of the problem are modeled using explicit schemes. To maintain second-order accuracy, the fluid dynamics operator must be second-order and here a prediction-correction scheme is used in the form given by Hirsch (1990b). To clarify the steps in the solution process, the sequence of equations are as follows,

$$
\begin{aligned}
S_\Omega(\Delta t/2) \; : \quad & \left[I - \frac{\Delta t}{4}\Omega'\right]^n \Delta Q^* = \frac{\Delta t}{2}\Omega^n \\
& Q^* = Q^n + \Delta Q^* \\
S_F(\Delta t) \; : \quad & \Delta Q^{**} = -\frac{\Delta t}{2}\left[\partial_\xi F^{(1)} + \partial_\eta G^{(1)} + H\right]^* \\
& Q^{**} = Q^* + \Delta Q^{**} \\
& \Delta Q^{***} = -\Delta t\left[\partial_\xi F^{(2)} + \partial_\eta G^{(2)} + H\right]^{**} \\
& Q^{***} = Q^* + \Delta Q^{***} \\
S_\Omega(\Delta t/2) \; : \quad & \left[I - \frac{\Delta t}{4}\Omega'\right]^{***} \Delta Q^{****} = \frac{\Delta t}{2}\Omega^{***} \\
& Q^{n+1} = Q^{***} + \Delta Q^{****}
\end{aligned}
\tag{3.91}
$$

where the superscript *'s denote what value of Q is used to calculate the fluxes, source terms, and Jacobian of the source term, $\Omega'\left(Q_{i,j}^n\right) = \partial\Omega\left(Q_{i,j}^n\right)/\partial Q_{i,j}^n$. The superscripts (1) and (2) denote the spatial order of the numerical fluxes. The term $\partial_\xi F = F_{i+\frac{1}{2}j} - F_{i-\frac{1}{2}j}$ and likewise for $\partial_\eta G$. The scheme used to define the inviscid numerical fluxes is the same as that used in the fully-implicit method. However, here the Jacobians of the fluid dynamic terms

do not have to be calculated which reduces computational time as does the fact that a banded system of equations does not have to be solved.

3.7.3 ODE Solution Issues

Even when implicit integration is used difficulties can arise when implementing the solution process for problems with large reaction rates. Here some of these issues are discussed in the context of solving the ODE associated with the source term operator in the splitting solution method. One difficulty is due to the fact that the Jacobian matrix Ω' can become ill-conditioned which can introduce errors when the equations are solved. The Jacobian matrix can be changed somewhat to help alleviate this problem. Consider the two step reaction

$$
\begin{aligned}
H_2 \;+\; O_2 &\;\leftrightarrows\; 2OH &\quad (1) \\
H_2 \;+\; 2OH &\;\leftrightarrows\; 2H_2O &\quad (2)
\end{aligned}
\qquad (3.92)
$$
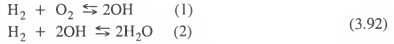
which is used later in this study and has been presented in Table 2.1. The source term for each species, when expanded, is

$$
\begin{aligned}
\dot{\omega}_{H_2} &= M_{H_2}\left\{ -k_{f_1}\!\left(X_{H_2}\right)\!\left(X_{O_2}\right) + k_{b_1}\!\left(X_{OH}\right)^2 - k_{f_2}\!\left(X_{H_2}\right)\!\left(X_{OH}\right)^2 + k_{b_2}\!\left(X_{H_2O}\right)^2 \right\} \\
\dot{\omega}_{O_2} &= M_{O_2}\left\{ -k_{f_1}\!\left(X_{H_2}\right)\!\left(X_{O_2}\right) + k_{b_1}\!\left(X_{OH}\right)^2 \right\} \\
\dot{\omega}_{OH} &= 2M_{OH}\left\{ k_{f_1}\!\left(X_{H_2}\right)\!\left(X_{O_2}\right) - k_{b_1}\!\left(X_{OH}\right)^2 - k_{f_2}\!\left(X_{H_2}\right)\!\left(X_{OH}\right)^2 + k_{b_2}\!\left(X_{H_2O}\right)^2 \right\} \\
\dot{\omega}_{H_2O} &= M_{H_2O}\left\{ 2k_{f_2}\!\left(X_{H_2}\right)\!\left(X_{OH}\right)^2 - 2k_{b_2}\!\left(X_{H_2O}\right)^2 \right\}
\end{aligned}
\qquad (3.93)
$$

and after some simple arithmetic those for H_2 and OH can be written in the form

$$
\begin{aligned}
\dot{\omega}_{H_2} &= \frac{M_{H_2}}{M_{O2}}\left[\omega_{O2}\right] - \frac{M_{H_2}}{2M_{H_2O}}\left[\omega_{H_2O}\right] \\
\dot{\omega}_{OH} &= -\frac{2M_{OH}}{M_{O2}}\left[\omega_{O2}\right] - \frac{M_{OH}}{M_{H_2O}}\left[\omega_{H_2O}\right] \;.
\end{aligned}
\qquad (3.94)
$$

The Jacobian matrix of the source term can be altered to reflect the relationships of Eqn. (3.94). This implementation has been used for reaction mechanism composed of two and

eight steps and has proven to increase the robustness of the computational code in the case of the two-step mechanism. This is due to the fact that the reaction rate constants for the two-step mechanism are orders of magnitude larger than those for the higher order mechanisms and result in a Jacobian matrix with a much larger condition number. For the higher order mechanisms, the Jacobian matrix using the standard form is well conditioned.

Even if the Jacobian matrix is well conditioned and a solution is obtained, the resulting state of Q can be nonphysical. This is typically manifested in the mass fractions of various species being less than zero. These nonphysical solutions are a result, once again, of the fact that quantities such as mass fraction vary in a logarithmic fashion. Because the solution process utilizes a linearization for the derivative of Q, these overshoots are produced. In the solution of problems such as the reacting flows currently studied, such non-physical solutions must be guarded against. This can be done by either taking smaller time steps, which is not desirable, or by employing a scaling technique such as the method demonstrated by Ramshaw and Chang (1995). Here a technique is used which scales ΔQ if the solution of the ODE in Eqn (3.91) would result in a non-physical Q. In the current code, the solutions from the ODEs of Eqn. (3.91) are evaluated to see if Q^* or Q^{n+1} contain species mass fractions such that $\alpha_i < 0$ for all i. If so, a single appropriate scaling factor is calculated and applied to all ΔQ's such that $0 < \alpha_i < 1$ for all i. The change in Q due to the fluid dynamic operator presents no problem. This is due to the fact that the Δt is calculated based on the CFL < 1 condition necessary for explicit schemes.

When applying such a scaling, caution must be used to ensure the actual equation being solved is not altered. In the case of steady-state solutions, typically the scaling is needed only in the early stages of the evolution of the flow field. If the scaling factor converges to 1 long before the convergence of the governing equations to the steady-state solution, then there are no concerns that the equations have been altered. In the case of unsteady problems, an iterative process can be used to solve the ODE to ensure non-physical solutions are not encountered. However, typically when solving unsteady problems, the time

step is set small to resolve the evolution of the flow field and such problems are not encountered. It should be noted that these overshoots are different than the round-off errors which can appear as mentioned earlier and as addressed in previous investigations (Sussman, 1993 and Wilson and Sussman, 1993).

3.8 Summary

Here the various models needed to successfully simulate the problems of interest have been described. As is clear, there are numerous phenomenological and numerical models available. Those selected to be used in the current development offer the latest in methodology and have a wide range of applicability. This is important in the context of the current study given the fact that a multitude of scales are intertwined. Those simplification that have been made have been done so after analyzing the phenomenology of the process and based on previous investigations. From the numerical aspect, one of the key items to be highlighted is the source term treatment. This is due to the fact that previous investigations have shown the accuracy is highly dependent on the grid resolution. The source term treatments offer a viable alternative to the computationally intensive grid adaptation schemes.

The primary chemical aspect to be focused on is the impact of the reaction mechanism. The model described here is used to compute the shock-induced combustion problem with various mechanisms in a effort to correlate mechanism characteristics to simulation accuracy. The impact of turbulence in the reactive flow scenarios presented here is also quantified. Both the modeling of the turbulence and the coupling of these effects with the chemical processes are detailed in the next chapter. The turbulence effects are known to be manifested in the governing equations through the viscous aspects. It is clear from the description of the governing equations that these aspects impact field quantities but also the chemical process through the dispersion of species and heat.

CHAPTER 4

TURBULENCE MODEL

The turbulence aspects of the problems of interest like the other physical and chemical aspects require a phenomenological model. As eluded to earlier, turbulence impacts many of the aspects already discussed as well as the particular models that have been described. Therefore, this aspect of the problem is dedicated its own chapter to emphasize both the phenomenological importance of turbulence but also the attention which must be paid to its modeling.

A turbulent flow, like all continuum fluid problems, is governed by the Navier-Stokes equations. But to model these equations on the length and time scales to resolve all pertinent physical phenomena is not a practical method given today's computational platforms. Simulations which do resolve all the scales ranging from the small to the large eddies are conducted and are labeled Direct Numerical Simulations (DNS). A review of DNS is provided by Galperin and Orszag (1993). To highlight the computational resources required to conduct a DNS let us estimate the number of grid points that would be required for the fuel cell scenario.

As mentioned, the phenomena of turbulence is known to be driven by a multitude of scales, particularly the large scale eddies which contain what is call the turbulent kinetic energy and the small scale eddies which work to dissipate this energy. The dynamics of turbulence consist of various transformation processes which transfer this energy between the eddies. To capture all the important phenomena, the governing equations must be discretized spatially such that all scales are resolved. This infers that the computational grid used must contain points spaced on the order of the size of the small eddies. The

characteristic length scale of the small eddies is the Kolmogoroff scale (η) and the ratio of

this scale to the characteristic length scale of the large eddies (l_e) is related to the large eddy

Reynolds number by $\eta/l_e = \left(Re_{l_e}\right)^{-\frac{3}{4}}$ where $Re_{l_e} = \frac{ul_e}{\nu}$. Therefore, to capture all scales of

interest, the grid spacing must be on the order of $\eta = l_e\left(\nu^3/u^3 l_e^3\right)^{\frac{1}{4}}$. Given the fact that these

small eddies can have an arbitrary orientation in the flow, this same spacing must be used

in all three physical dimensions. An estimate of l_e is needed and for the fuel cell scenario,

the large scale eddies are on the order of the thickness of the various shear layers which mix

the fuel and oxidizer. These shear layers are on the order of the size of the projectile so this

length scale can be estimated as $l_e = O(d)$ where d is the projectile diameter. Using the

Reynolds number of the mean flow ($Re = ud/\nu$) we can estimate the Kolmogoroff scale to

be $\eta = O\left[d(Re)^{-\frac{3}{4}}\right]$. Recalling that the discretization must be on this order in all directions

and considering the computational domain, at the least, must be on the order of the projectile

diameter, the number of points to carry out a DNS study of this problem is on the order of

$(Re)^{\frac{9}{4}}$. Using quantities for the viscosity, length, and velocities comparable to those in the

problems to be solved here, we have $Re = O\left(1.0 \times 10^7\right)$ which would require on the order

of 5×10^{15} spatial points on which the governing equations must be solved. This is clearly

not practical for typical engineering analysis or much less easy given the current

computational platforms. However, DNS is pursued for moderate Reynold's numbers and

simple geometries in hopes of better understanding the dynamics of turbulence thereby

advancing optional modeling techniques. These optional techniques are required to

complement the solved set of governing equations in an attempt to reproduce the dynamics

of those scales known to not be adequately resolved.

     The temporal scale of the small eddies must also be considered if a DNS is to be

performed. This time scale can be thought of as the turnover time of the small eddies. Like

the spatial requirements impact the number of points at which the governing equations must

be solved and in turn the amount of computer memory needed, this requirement on the temporal discretization effects the required computational time as does the small time scales of the chemical reactions.

The next level from DNS in the context of grid requirements is Large Eddy Simulation (LES) in which grid refinements are used such that the large scales of turbulence are resolved but a model is needed for the small scale phenomena. LES is also characterized by the use of spatial filters on the governing equations. This terminology is used because the computational grid has to be constructed such that the spatial discretization is on the order of the inertial subrange, or that region which lies between the large and small eddies and over which the primary physical process is the transfer of energy. Since the primary role of the small eddies is known to be one of energy dissipation, this is the phenomena which must be modeled. A review of LES is provided by Erlebacher et al. (1992) and Germano (1992).

In the context of solving a full scale engineering problem, the term large eddy is somewhat misleading in that the size of the large scales in turbulence can still be orders of magnitude smaller than the domain over which the solution must be carried out. Therefore, the LES requirement to resolve only the large scales is still computationally restrictive. However, LES is currently being pursued aggressively and has been used for many problems of interest. LES will continue to become more viable as computational platforms become faster and cheaper.

Based on the description of DNS and LES, it is clear that an optional modeling technique is needed for problems composed of large Reynolds numbers and large computational domains. The problem in modeling turbulent flows is that the highly nonlinear dynamics, represented by the Navier-Stokes equations, occurring at these unresolved scales produce phenomena when observed from a larger frame of reference appear random and non-systematic. The model of choice for problems such as the reactive munition and shock-induced combustion scenarios remains a class of engineering models labeled moment methods which are solved in conjunction with a set of averaged governing

equations. There are many options as to both how to average the equations as well as the form of the engineering models. More details on various engineering models is provided by Wilcox (1992) and a review in the context of reacting flows is provided by Libby and Williams (1994). Here the work of Krishnamurty (1996) is followed to describe the implementation of one particular model in an attempt to quantify the role of turbulence in the reacting flow problems of interest.

4.1 Averaging Techniques and Averaged Variables

As mentioned, when a turbulent flow is observed, an apparent randomness exists. Conceding the fact that all scales are not to be resolved, it is assumed that a solution on the resolvable scales can provide a statistical average of the exact flow field. In LES a spatial averaging, or filtering, procedure is used. Here, however, the averaging is cast as either a time or ensemble average. A time average of a quantity with instantaneous value ϕ is

$$\overline{\phi} = \lim_{T \to \infty} \frac{1}{T} \int_{t_0}^{t_0 + T} \phi \, dt \tag{4.1}$$

where T is the period over which the instantaneous values are sampled. This results in a formula for the instantaneous value at a given time of the form

$$\phi = \overline{\phi} + \phi' \tag{4.2}$$

where ϕ' is the deviation from the mean and by definition $\overline{\phi'} = 0$.

When solving unsteady flows, it is more applicable to employ a methodology of ensemble averaging. The ensemble average of a quantity ϕ is an average over a number of realizations of the problem and mathematically is

$$\overline{\phi} = \lim_{N \to \infty} \frac{1}{N} \sum_{n=1}^{N} \phi_n \tag{4.3}$$

where again ϕ' is the deviation from the mean and by definition $\overline{\phi'} = 0$. A realization is simply the same problem restarted from the same initial conditions with the quantity ϕ being measured at the same point in space and at the same time after the start of the problem.

The mental picture of this type of averaging is an excellent way to frame the problem of turbulence. Consider the task of collecting an ensemble average of say the velocity at a specific point in the flow field about a model in a wind tunnel at a specific time after the tunnel is started. Assuming the measurement can be made precisely at the same point in time and space, the variation from measurement to measurement is a function of the nonlinearity of the governing equations. Small perturbations can be generated in any quantity whether it is caused by the startup process, a slight movement of the model, a small contaminant on the tunnel wall, or a miniscule change in the environment. These small changes can grow within the framework of the Navier-Stokes equations and effect the field quantities at various points in space and time. And as mentioned several times now, to capture this evolution with a computational model is no easy task.

Continuing with the premise that when the Navier-Stokes equations are solved on a grid known to introduce some statistical averaging, the equations which are actually solved need to be cast into a form accounting for this averaging process. The first step in doing so is defining the averaged variables based on the averaging techniques discussed earlier. When solving turbulent flows, averaged variables in the form of Eqn. (4.2) are typically defined as Reynolds averaged variables. With the added desire to model compressible flows, a second averaged variable definition is introduced. This is in light of the fact that unlike incompressible flows, the added aspect of compressibility can introduce deviations, or fluctuations, in density. By introducing a mass weighted average, denoted as a Favre average, the resulting equations are somewhat simpler. Using this form, the instantaneous value is given by

$$\phi = \tilde{\phi} + \phi''$$
(4.4)

where

$$\tilde{\phi} = \frac{\overline{\varrho\phi}}{\bar{\varrho}}$$
(4.5)

which results in the relationships

$$\overline{\phi''} = -\frac{\overline{\varrho'\phi''}}{\overline{\varrho}} \ , \qquad \overline{\varrho\phi''} = 0 \ . \tag{4.6}$$

Note, the tilde and double primes are used to distinguish Favre averaged variables from Reynolds averaged ones. One reason this approach is taken in modeling compressible turbulent flows is that with the density weighting introduced, the final form of the governing equations is closely analogous to the incompressible form and it is in the context of incompressible turbulence that most models have been developed.

Following the typical convention, a mix of Reynolds and Favre averaged variables are used. Specifically, Reynolds averaging is used for the density and pressure and Favre averaging for the velocity components and scalars such as temperature and species mass fractions. The forms are

$$\begin{aligned}
\varrho &= \overline{\varrho} + \varrho' \\
p &= P + p' \\
u_i &= \tilde{u}_i + u_i'' \\
T &= \tilde{T} + T'' \\
\alpha_i &= \tilde{\alpha}_i + \alpha_i'' \ .
\end{aligned} \tag{4.7}$$

The next section presents the form of the governing equations once these averaged variables are introduced.

4.2 Averaged Equations

A review of the averaging process is provided by Wilcox (1992). Here the final form of the equations are presented. This final form is obtained by introducing the defined average variables of Eqn. (4.7) into the governing equations of Chapter 3 and making use of the relationships given above. Note, for convenience, the Cartesian form of the equations with tensor notation is used in the discussion. The continuity equation takes the form

$$\frac{\partial}{\partial t}\left(\overline{\varrho}\right) + \frac{\partial}{\partial x_j}\left(\overline{\varrho}\tilde{u}_j\right) = 0 \tag{4.8}$$

and the momentum

$$\frac{\partial}{\partial t}\left(\overline{\varrho}\tilde{u}_i\right) + \frac{\partial}{\partial x_j}\left(\overline{\varrho}\tilde{u}_i\tilde{u}_j\right) = -\frac{\partial P}{\partial x_i} + \frac{\partial}{\partial x_j}\left(\tilde{\tau}_{ij} + \overline{\tau_{ij}''} - \overline{\varrho u_i''u_j''}\right) \tag{4.9}$$

where

$$\bar{\tau}_{ij} = \nu\left[\frac{\partial\tilde{u}_i}{\partial x_j} + \frac{\partial\tilde{u}_j}{\partial x_i}\right] + \lambda\left[\frac{\partial\tilde{u}_k}{\partial x_k}\right]\delta_{ij}$$

$$\overline{\tau_{ij}''} = \nu\left[\overline{\frac{\partial u_i''}{\partial x_j}} + \overline{\frac{\partial u_j''}{\partial x_i}}\right] + \lambda\left[\overline{\frac{\partial u_k''}{\partial x_k}}\right]\delta_{ij} \tag{4.10}$$

and the term $\overline{\varrho u_i'' u_j''}$ is yet to be defined. The energy equation, with the introduction of total enthalpy, $H = E + \dfrac{P}{\varrho}$, and specific enthalpy, $h = e + \dfrac{P}{\varrho}$, becomes

$$\frac{\partial}{\partial t}\left(\bar{\varrho}\tilde{E}\right) + \frac{\partial}{\partial x_j}\left(\bar{\varrho}\tilde{u}_j\tilde{H}\right) = -\frac{\partial}{\partial x_j}\left[\tilde{u}_i\left(\bar{\tau}_{ij} + \overline{\tau_{ij}''} - \overline{\varrho u_i'' u_j''}\right) + \overline{u_i''\tau_{ij}} + \overline{u_i''\tau_{ij}''}\right. $$
$$\left. - \tilde{q}_j - \overline{q_j''} - \overline{\varrho u_j'' h''} - \overline{\varrho u_j''(\tfrac{1}{2}u_i'' u_i'')}\right] . \tag{4.11}$$

Recall for reacting flows, the heat flux is also a function of species diffusion velocities as given in Eqn. (3.11). Also, as a result of the averaging process, the the total energy, E, now includes the turbulent kinetic energy which is defined later. The final equation is the species conservation equation and when averaged for a single species n is

$$\frac{\partial}{\partial t}\left(\bar{\varrho}\tilde{\alpha}_n\right) + \frac{\partial}{\partial x_j}\left(\bar{\varrho}\tilde{\alpha}_n\tilde{u}_j\right) - \frac{\partial}{\partial x_j}\left[\frac{\mu}{Sc}\frac{\partial\left(\tilde{\alpha}_n + \overline{\alpha_n''}\right)}{\partial x_j} - \overline{\varrho\alpha_n'' u_j''}\right] = \overline{\dot{\omega}_n} \tag{4.12}$$

where the source term is denoted as an average and the particular representation is discussed later.

The first terms to be addressed are those that are dependent on the product of the molecular viscosity and the fluctuating terms. This includes $\overline{\tau_{ij}''}$ in the momentum equation, $\overline{u_i''\tau_{ij}}$ and $\overline{q_j''}$ in the energy equation, and $\dfrac{\mu}{Sc}\dfrac{\partial\overline{\alpha_n''}}{\partial x_j}$ in the species conservation equation. These terms are small in magnitude when compared to the terms that are a function of the product between molecular viscosity and the mean field quantities. Therefore, these terms are ignored in the modeling. The remaining terms are significant and must be modeled.

4.3 Turbulence Closure

The first term in need of modeling, or closure, is $\overline{\varrho u_i'' u_j''}$ which is a symmetric tensor with six independent components. Analysis shows that this term behaves much like the molecular stress term and is labeled the Reynolds-stress tensor. Boussinesq first proposed modeling this term in an analogous fashion, dependent on the gradients of the mean field. This requires an effective viscosity dependent on the turbulence, and the estimation of this turbulent viscosity varies based on the model employed. The first level in sophistication is the mixing-length model proposed by Prandtl (Tennekes and Lumley, 1972) which uses the gradient of the mean velocity field and a yet undetermined mixing length to define the viscosity. In a shear layer flow, the form for the turbulent viscosity is

$$\mu_t = \varrho l_{mix}^2 \left| \frac{du}{dy} \right| \tag{4.13}$$

where u is the streamwise component of velocity and y is normal to the flow direction. This model performs well for some flows in which the mixing length, l_{mix}, has been empirically determined. However, this model offers limited potential for complex flow fields in which a single length scale does not hold. A more appropriate model for such flows is one which incorporates the dynamics of turbulence in the estimation of turbulent viscosity. This requires the definition of a velocity scale and length scale.

Various models have been used and a review is provided by Wilcox (1992). Here, one particular model is discussed and integrated with the other models required for the high-speed reactive flow problems. The model used here is the k-ε model, a two-equation model with its foundation in the work of Jones and Launder (1973). The exact equations used to govern these quantities are presented next but first the closure of the various terms in the averaged equations are discussed. The quantity k is the turbulent kinetic energy mentioned earlier and ε is the dissipation of k and both are defined as

$$k = \frac{\frac{1}{2}\overline{\varrho u_i'' u_i''}}{\overline{\varrho}} \quad , \quad \varepsilon = \nu \overline{\frac{\partial u_i''}{\partial x_j} \frac{\partial u_i''}{\partial x_j}} \quad . \tag{4.14}$$

Using k and ε to define the velocity and length scale of turbulence, the turbulent viscosity becomes

$$\mu_t = C_\mu \varrho \frac{k^2}{\varepsilon} \qquad (4.15)$$

where C_μ is a constant found to be .09. The Reynolds stress term is modeled as

$$-\overline{\varrho u_i{''} u_j{''}} = \mu_t \left[\frac{\partial \bar{u}_i}{\partial x_j} + \frac{\partial \bar{u}_j}{\partial x_i} \right] + \lambda_t \left[\frac{\partial \bar{u}_k}{\partial x_k} \right] \delta_{ij} - \frac{2}{3} \overline{\varrho} k \delta_{ij} \qquad (4.16)$$

with the last term introduced to maintain the proper trace of the Reynolds stress tensor. The turbulent bulk viscosity is represented as is the molecular, $\lambda_t = -\frac{2}{3} \mu_t$.

The next term in need of closure is $\overline{\varrho u_j{''} h{''}}$ which is modeled, using the Reynolds' analogy (Hinze, 1959), as

$$-\overline{\varrho u_j{''} h{''}} = \frac{C_p \mu_t}{Pr_t} \frac{\partial T}{\partial x_j} \qquad (4.17)$$

where Pr_t is the turbulent Prandtl number. Using this closure, a single turbulent Prandtl number, assumes the turbulent transport of heat and momentum are dependent on a single time scale, i.e. the ratio between the turbulent heat and momentum flux are the same throughout the flow field. This assumption is known to not hold in many flow scenarios and an optional modeling concept such as the work of Nagano and Shimada (1996) is to define a second velocity and length scale associated with the heat flux. This allows the thermal eddy diffusivity to be calculated explicitly throughout the flowfield. For the current study which is an initial investigation into the coupling of the turbulence and chemical reacting aspects of the flow, the closure of Eqn. (4.17) is deemed acceptable. In most flows, the turbulent Prandtl number is close to unity and that is the value used in the current study. The remaining term in the energy equation, Eqn. (4.11), is $\overline{u_i{''} \tau_{ij}{''}} - \overline{\varrho u_j{''} (\frac{1}{2} u_i{''} u_i{''})}$ which represents the diffusion of energy due to turbulent fluctuations and is modeled as

$$\overline{u_i{''} \tau_{ij}{''}} - \overline{\varrho u_j{''} (\frac{1}{2} u_i{''} u_i{''})} = \frac{\mu_t}{\sigma_k} \frac{\partial k}{\partial x_j} \qquad (4.18)$$

where σ_k is a Prandtl number associated with the turbulent kinetic energy and is set to unity.

The one term in the species conservation equation needing closure is $\overline{\varrho\alpha_n''u_j''}$. Using the gradient treatment already introduced for the turbulent heat flux, the term is modeled as

$$- \overline{\varrho\alpha''u_j''} = \frac{\mu_t}{Sc_t}\frac{\partial\alpha_n}{\partial x_j} \qquad (4.19)$$

where the turbulent Schmidt number, Sc_t, has been introduced. As in the case of the turbulent Prandtl number, assuming a single turbulent Schmidt number prescribes that the scales associated with the turbulent transport of species are the same throughout the flow relative to those of the momentum. Also, similar to the modeling option for the turbulent heat flux, additional equations can be solved for the correlations of Eqn. (4.19) but an additional equation is needed for each species which can be computationally expensive. Here, $Sc_t=1$ which also implies the turbulent Lewis number is 1. All the modeled terms are now expressed as a function of k and ε so the next issue is the modeling of these two quantities.

4.4 k-ε Model

The equation for k is derived by manipulating the momentum equation. A description is given in Krishnamurty (1996) but here only the final form of the equation is given,

$$\frac{\partial}{\partial t}\left(\overline{\varrho}k\right) + \frac{\partial}{\partial x_j}\left(\overline{\varrho}\tilde{u}_j k\right) = - \overline{\varrho u_i''u_j''}\frac{\partial\tilde{u}_i}{\partial x_j} - \overline{u_i''}\frac{\partial\overline{P}}{\partial x_i} - \overline{\frac{\partial u_i''}{\partial x_j}\tau_{ij}''}$$
$$+ \frac{\partial}{\partial x_j}\left[\overline{u_i''\tau_{ij}''} - \overline{\varrho u_j''(\frac{1}{2}u_i''u_i'')} - \overline{p'u_j''}\right] + \overline{p'\frac{\partial u_i''}{\partial x_i}} \qquad (4.20)$$

where some terms needing closure have already been defined. The definitions for the production of turbulent kinetic energy and the rate of dissipation of this same energy are such that

$$P_k = - \overline{\varrho u_i''u_j''}\frac{\partial\tilde{u}_i}{\partial x_j}$$
$$\Phi_\varepsilon = \overline{\frac{\partial u_i''}{\partial x_j}\tau_{ij}''} \ . \qquad (4.21)$$

Note, the term $\overline{p' u_j''}$ is not explicitly modeled and is included in the closure of Eqn. (4.18).

The terms $\overline{p' \dfrac{\partial u_i''}{\partial x_i}}$ and $\overline{u_i'' \dfrac{\partial P}{\partial x_i}}$ are, respectively, the pressure dilatation term and the enthalpic production term. A model has been proposed by Krishnamurty (1996) for these terms and has been evaluated for nonreacting blunt body flows with shocks. The work of Krishnamurty (1996) shows these terms may prove important in flows where compressibility effects are significant. The shock-induced combustion flow studied here is a high-speed, compressible flow and it may prove necessary to model these terms. However, for this initial investigation, the standard form of the k-ε model is used. This is due in part to establish a benchmark using the baseline model but also in light of the fact that the derivation of the models proposed by Krishnamurty (1996) need to be investigated in the context of multi-species reacting flows. There have also been several modifications proposed for addressing known compressibility effects and how they impact factors such as the dissipation rate of k. These modifications are also discussed in detail by Krishnamurty (1996). Here, the final form of the k equation used is

$$\frac{\partial}{\partial t}\left(\overline{\varrho}k\right) + \frac{\partial}{\partial x_j}\left(\overline{\varrho}\tilde{u}_j k\right) = P_k - \overline{\varrho}\varepsilon + \frac{\partial}{\partial x_j}\left[\left(\mu + \frac{\mu_t}{\sigma_k}\right)\left(\frac{\partial k}{\partial x_j}\right)\right] \qquad (4.22)$$

The governing equation for ε is not as cleanly derived from the Navier-Stokes equations but is based on the assumption the time rate of change and the convection of the dissipation (ε) is balanced by a production, dissipation and diffusion term in the form

$$\frac{\partial \overline{\varrho}\varepsilon}{\partial t} + \frac{\partial}{\partial x_j}\left(\overline{\varrho}\tilde{u}_j \varepsilon\right) = P_\varepsilon - \Phi_\varepsilon + T_\varepsilon + B_\varepsilon \qquad (4.23)$$

Unlike the k equation which is derived from manipulation of the Navier-Stokes equations, the terms in the ε equation have been derived based on dimensional analysis and physical reasoning. The terms in the standard model are

$$P_\varepsilon = C_{\varepsilon 1}\frac{\varepsilon}{k}P_k \ , \ \ \Phi_\varepsilon = C_{\varepsilon 2}\overline{\varrho}\frac{\varepsilon^2}{k} \ , \ \ T_\varepsilon = \frac{\partial}{\partial x_j}\left[\left(\mu + \frac{\mu_t}{\sigma_\varepsilon}\right)\frac{\partial \varepsilon}{\partial x_j}\right] \qquad (4.24)$$

where σ_ε is a Prandtl number associated with the ε and is set to 1.3. The coefficients in the production and dissipation terms can be modified to account for the imbalance between the production and dissipation of turbulent kinetic energy. These modeling option are discussed by Chen and Kim (1987) for $C_{\varepsilon 1}$ and Thakur et al. (1996) for $C_{\varepsilon 2}$. Here, the standard values of $C_{\varepsilon 1} = 1.44$, $C_{\varepsilon 2} = 1.92$ are used.

The term B_ε represents the baroclinic torque term which arises due to gradients in density and pressure, $\left[\vec{\nabla}\left(\frac{1}{\varrho}\right) \times \left(\vec{\nabla}p\right) \right]$, which do not appear in incompressible problems. A model for this term, which may prove important to flows such as the current shock-induced combustion scenario, is proposed by Krishnamurty (1996). Here, though the standard form of the equation,

$$\frac{\partial \overline{\varrho}\varepsilon}{\partial t} + \frac{\partial}{\partial x_j}\left(\overline{\varrho}\overline{u}_j\varepsilon\right) = \frac{\varepsilon}{k}\left(C_{\varepsilon 1}P_k - - C_{\varepsilon 2}\overline{\varrho}\varepsilon\right) + \frac{\partial}{\partial x_j}\left[\mu + \frac{\mu_t}{\sigma_\varepsilon}\left(\frac{\partial \varepsilon}{\partial x_j}\right)\right] \qquad (4.25)$$

is solved. Now that the equations for k and ε have been presented, the next section specifies the needed boundary conditions.

4.5 Wall Function

The k-ε model used here requires a wall treatment due to the low Reynolds number associated with this region. Here, the standard wall function (Wilcox, 1992) is used. This function is based on the known correlation between the nondimensional velocity near the wall and the nondimensional distance from the wall. This velocity is specified as $U^+ = U_p/U_\tau$ where $U_\tau = \sqrt{\tau_{wall}/\varrho}$ and the nondimensional height is $y^+ = \left(\varrho U_\tau\, y_p\right)/\mu$ where y_p is the distance normal to the wall and μ is the molecular viscosity. In the viscous sublayer, the region nearest the wall, the relationship

$$U^+ = y^+ \qquad (4.26)$$

holds. Outside this region, the relationship between the two nondimensional quantities is

$$U^+ = \frac{1}{\varkappa}\ln\left(y^+\right) + B \qquad (4.27)$$

where $\varkappa$ is the von Kármán constant set to .41 and B=5.1. Therefore, this region is labeled the log layer. Where the curves defined by Eqn. (4.26) and Eqn. (4.27) meet is defined y_c^+, the critical value of the nondimensional height.

In a finite volume scheme, such as the one developed here, the flow properties are defined at the cell centers. Therefore, when implementing the wall function, the y^+ corresponding to each cell which bounds the wall must be calculated based on the half-height of the cell. Using this value along with velocity and viscosity, the boundary values for k and ε are calculated, if $y^+ < y_c^+$, using (Krishnamurty, 1996)

$$k_{\text{wall}} = \frac{U_\tau^2}{\sqrt{C_\mu}} \left(\frac{y_p^+}{y_c^+} \right)^2 \quad , \quad \varepsilon_{\text{wall}} = \frac{k_{\text{wall}}^{\frac{3}{2}}}{l_\varepsilon} \tag{4.28}$$

where

$$l_\varepsilon = \frac{c_i y_p}{1 + \frac{5.3}{\text{Re}_t}} \quad , \quad c_i = \varkappa \left(C_\mu \right)^{-\frac{3}{4}} , \quad \text{Re}_t = \frac{\varrho \sqrt{k_{\text{wall}}}\, y_p}{\mu} \quad . \tag{4.29}$$

If $y^+ > y_c^+$ then the boundary conditions are specified as

$$k_{\text{wall}} = \frac{U_\tau^2}{\sqrt{C_\mu}} \quad , \quad \varepsilon_{\text{wall}} = \frac{U_\tau^3}{\varkappa y_p} \quad . \tag{4.30}$$

Now that the equations for k and ε have been specified as well as the boundary conditions for both quantities at the wall, the final information needed is the boundary condition for k and ε at the inflow. This is typically specified in terms of a turbulent intensity, the magnitude of the velocity fluctuations relative to the mean value. Here a value of 3% is used base on data for similar flow scenarios used in earlier studies (Krishnamurty, 1996).

The governing equations for k and ε are solved in conjunction with the Navier-Stokes equations. These equations provide the necessary information with which to define μ_t. With the addition of the turbulent viscosity, an estimate of the enhanced diffusion of species and heat is obtained. This alone can impact the mean flow field and the impact this has on the shock-induced combustion scenario is studied. In addition to these effects, the turbulence

aspects of the flow can also directly impact the reaction source term. This is the focus of the next section.

4.6 Turbulence Effects On The Reaction Source Term

The chemical reaction source term, $\overline{\omega}_n$, in Eqn. (4.12) is a function of temperature and species mass fractions. The chemical source term is a function of the mean values of these quantities and any deviations. The effect of turbulence on the source term is first represented by modeling the impact turbulence has on the mean temperature and mass fraction field. This is done in the framework of the two-equation type model by applying the averaging and closures described above. The next step in modeling the impact of turbulence on the source term is to account for the effect of the fluctuations. This is needed given the highly nonlinear dependence of the source term on the dependent variables. The analysis of Sagara and Tsugé (1970) shows that the fluctuation in velocity does not effect the mean reaction rate, the effect of density fluctuations is relatively minor, and the primary effect of turbulence on the source term is manifested through the temperature fluctuations. They find the mean reaction rate in a turbulent field to be

$$\overline{\omega} = \frac{1}{2}\left[(1 + \Delta)^{\frac{1}{2}}\exp\left(\frac{\Gamma\Delta}{1 + \Delta}\right) + (1 - \Delta)^{\frac{1}{2}}\exp\left(\frac{-\Gamma\Delta}{1 - \Delta}\right)\right]\omega(\overline{\alpha}, \overline{T}) \qquad (4.31)$$

where $\Delta = \delta T/\overline{T}$ and $\Gamma = E/R\overline{T}$. The term $\delta T = \sqrt{\overline{T''T''}}$ is the root-mean-square of the temperature fluctuation. This effective source term can be written in the form

$$\overline{\omega} = \frac{1}{2}\left[(1 + \Delta)^{\frac{1}{2}}\omega(\overline{T} + \delta T) + (1 - \Delta)^{\frac{1}{2}}\omega(\overline{T} - \delta T)\right] \qquad (4.32)$$

after simple arithmetic. Given the highly nonlinear nature of ω, the resulting reaction source term can be quite larger than simply the order of magnitude of the temperature fluctuation, especially for large activation energies. This model has been used by Mizobuchi et al. (1997) to simulate a scramjet combustor scenario. In their computations the factors $(1 \pm \Delta)^{\frac{1}{2}}$ are neglected but here, these are included. Their results show an improvement in the computed combustion efficiency when compared with experimental data.

To this point in the modeling of the various terms in the averaged equations, the presence of temperature fluctuations has been solely in the context of the correlation of these fluctuations with those of velocity. As mentioned in the context of the closure of Eqn. (4.17), one modeling option is to solve additional equations for the temperature fluctuations scales. If such a model is used then the estimate of the root-mean-square of the temperature deviation is explicitly provided. Since we have chosen to specify a single turbulent Prandtl number, these deviations are to be estimated based on the deviations in the velocity field. This is considered appropriate given the goal of the current study is to determine if any estimate for the effect of turbulence on the temperature field impacts the computed flow field in the problems of interest.

Using the strong Reynolds analogy (Gaviglio et al., 1977), the ratio of the root-mean-square of the temperature fluctuations to the mean value is related to the velocity field as

$$\frac{\delta T}{\bar{T}} = (\gamma - 1)M^2 \frac{\sqrt{2k}}{U} \tag{4.33}$$

where U denotes the velocity magnitude and k is used to estimate the root-mean-square of the velocity fluctuations.

4.7 Summary

The model employed to represent the turbulent aspects of the flows has been described. The two-equation model has been selected due to its utility in solving full-scale engineering problems. The various modifications to the k-ε for compressibility effects and the imbalance between the production and dissipation of the turbulent kinetic energy have been presented. In the initial computations, the standard form of the equations is used to produce a benchmark to which further computations using these modifications can be compared. Turbulence is known to enhance the dispersion of species and heat and these aspects in turn affect the chemical processes. An additional effect explicitly accounted for in the present effort is the impact of temperature fluctuations. This is incorporated through

a modified source term dependent on the root-mean-square of the temperature fluctuations. The impact turbulence has on the problems of interest is detailed in the context of results using these models presented in the next chapters.

CHAPTER 5
SHOCK-INDUCED COMBUSTION RESULTS AND DISCUSSIONS

Through the review of the earlier computational studies into the shock-induced combustion scenario and model development discussion, it is clear that many issues related to both the numerical and phenomenological aspects of the models used can affect the outcome of the simulation. For example, it has been quantified in the discussion of the source term treatments that the numerical error due to the presence of the reaction source term is dependent on the cell Damköhler number, $\mathfrak{D}_{cfd} = k\Delta x/u$. Using this parameter to frame the computational investigation into high-speed reacting flows, the phenomenological aspects of importance is the reaction rate, k, and the local flow speed, u, while the numerical aspect is the mesh spacing, Δx. To date, the numerical aspect has been the primary focus of investigations into the shock-induced combustion flow scenario.

In the context of the shock-induced combustion problem, various techniques for addressing this numerical aspect have been evaluated including grid adaptation (Wilson and MacCormack, 1990, Sussman, 1993, Shang et al., 1995), source term treatments (Sussman, 1993, Shang et al., 1995), and solving a logarithmic form of the governing equations (Sussman and Wilson, 1991, Wilson and Sussman, 1993). In these earlier studies a single reaction mechanism is selected and used to simulate the M=6.46 shock-induced combustion case captured by Lehr (1972). A main focus of these earlier computations has been to quantify the effectiveness of particular numerical treatments. Wilson and MacCormack (1990) do compare the effect of altering the rate of the chain-branching reaction $H + O_2 \rightleftharpoons OH + O$ and note the impact the alteration has on the induction time. However, none of the studies perform a comprehensive comparison over a wide range of reaction mechanisms

which is one focus of the present investigation. A subset of those numerical techniques developed in these earlier studies is evaluated, particularly the source term treatments including the logarithmic interpolation proposed by Shang et al. (1995) and the scaling factor scheme proposed by Sussman (1993). Also evaluated is the explicit-implicit splitting scheme used to integrate the governing equations.

Given the variety of reaction mechanisms that has been proposed for the hydrogen-oxygen reaction process, the models used here have been selected based on their use in earlier computations of the shock-induced combustion scenario. These models are used to derive key parameters useful in quantifying reaction mechanisms and shown to be directly related to the computed flow fields. This establishes comparison parameters useful in future studies into the aspects of computing high-speed reacting flows and the coupling of the numerical and physical aspects.

To assess the impact the numerical and physical aspects have on the accuracy of such computations, a starting point must be selected. The steady combustion scenario at M=6.46, captured by Lehr (1972) is chosen as the case to study. Based on the success of earlier computations, neither wall nor turbulence seems to have order one effects in the overall flow field and a logical starting point is to perform the computations with an inviscid model using piecewise representation of the source term. This is done in part to compare the current computations with those of earlier investigations.

Based on the review of previous computational studies of Lehr's experiments (1972) it has been decided to first consider the 7-step mechanism on a moderate grid and with no special treatment of the source term. The present computational grid is composed of 80x120 cells with 120 being in the direction normal to the body. The current grid is shown in Figure 5.1. To simplify the issue related to the grid distribution, uniform spacing is used in the normal direction and the tangential spacing along the body is approximately uniform.

The 7-step hydrogen-oxygen mechanism used in the baseline computation is given in Table 2.2 and is from the work of Drummond et al. (1986). The fully implicit solution
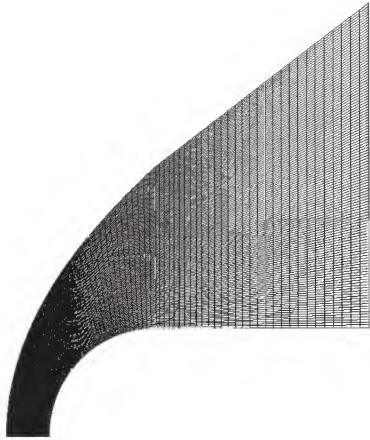
Figure 5.1.   Baseline 80 x 120 grid used for the M=6.46 case.

scheme is used for the computations presented in this section. Also, for all shock-induced

combustion computations, a third-order representation for the dependence of specific heats

on temperature is used. The density contour from this baseline computation is shown in

Figure 5.2 along with the reference points from the experimental shadowgraph presented

earlier. The computation is carried out for only half the field but a mirror image is also

presented to facilitate comparison to the experiments. The first noticeable feature of the

comparison is the asymmetry in the experimental data, especially in the axial locations near

the baseline of the projectile. It should be reiterated that there is also some optical distortion

in the shadowgraph and the reference points have been altered in no way. They have simply

been placed such that the experimental shock location on the stagnation line corresponds to
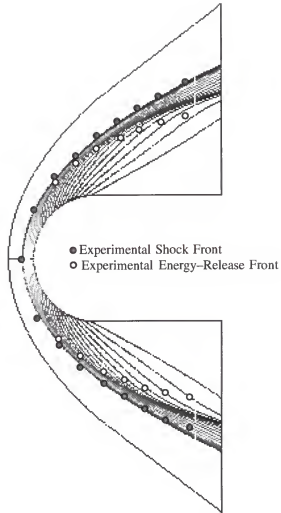
Figure 5.2.   Solution on the 80 x 120 grid for M=6.46 using the 7-step mechanism and the piecewise constant representation of the reaction source term.

that of the computations. Also, the data has been scaled 1:1 in length and height until the diameter of the experimental projectile matches that of the computational geometry. As is evident, this results in the reference points not extending as far to the base as in the experimental image of Figure 2.2. The data from the experimental shadowgraph can be altered to better match the length of the projectile in the computations but this requires additional assumptions on the optical distortion which are not made here.

The comparison between the computed shock and reaction fronts are quite good in the nose region but in the region further downstream the reaction front is somewhat closer

to the shock than the experimental data infers. This is one reason, unlike many of the previous studies, the current study models the complete length of the projectile to provide a more complete comparison. This thinning trend is also seen in the computations of Shang et al. (1995) in which the same reaction mechanism is used on a comparable grid. It is noted that all computations presented here have been converged to the point where the average density residual is reduced six orders of magnitude.

Before studying other modeling aspects, the dependence of the solution on the grid resolution used in the computation must be measured. The 80x120 grid has been chosen based on the results of Shang et al. (1995) and the results from this grid as well as three alternate grids are shown in Figure 5.3. For comparison purposes, only the experimental data from the upper half of the shadowgraph in Figure 2.2 is used. To make a more precise comparison, in Figure 5.4 the variation in density along a line normal to the cylindrical body is presented. The x location of the lateral variation is one radius downstream of the hemispherical nose-cylindrical body junction. All lengths are nondimensionalized by the projectile diameter. A similar comparison along the stagnation line results in lines that are essentially indistinguishable. The solutions on the coarser grids of 40x90 and 40x120 do alter the shock and reaction front location slightly, but even then the relative location of the reaction front to the shock are similar. Therefore, the thinning at the larger x must be due to factors other than the grid.

Although Figure 5.4 demonstrates that as the grid is refined, the solution seems to asymptotically converge, caution must be exercised when determining grid dependency for high-speed reacting flows. This is due to the role of the chemical reaction source term which is dependent on the distribution of species and temperature. In the context of solving the multi-dimensional problem, this source term is calculated in each computational cell, or control volume. The discussion on source term treatments has shown that error introduced through the representation of the source term in each cell is proportional to $k\Delta x/u$, the cell Damköhler number, where k denotes the reaction rate and Δx the grid spacing. Figure 3.3

40x90

40x120

40x150

80x120

● Experimental Shock Front; upper half
○ Experimental Energy–Release Front; upper half
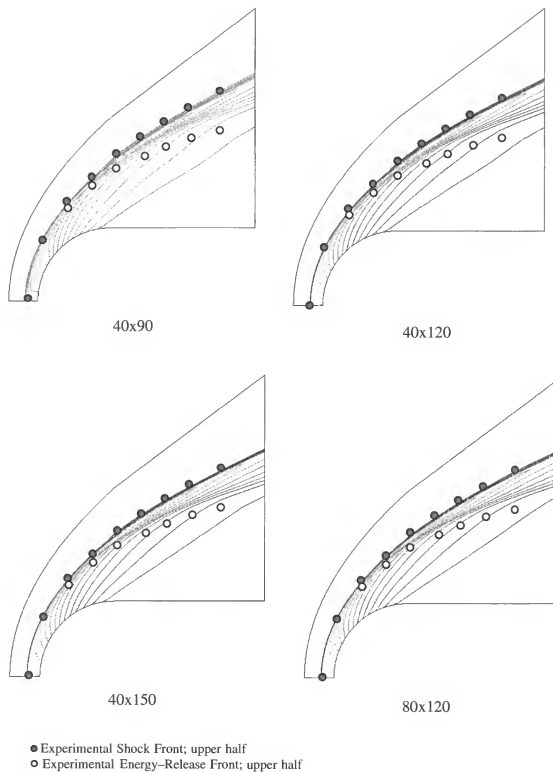
Figure 5.3.   Impact of grid resolution on the baseline M=6.46 computation using the 7-step mechanism. Experimental data used for comparison is the upper half of the shadowgraph in Figure 2.2.
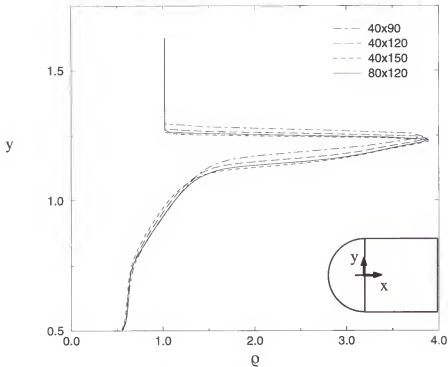
Figure 5.4. Density variations along a line normal to the body corresponding to the contours of Figure 5.3.

shows that to eliminate this error, the cell Damköhler number, $\mathfrak{D}_{cfd}$, must be small and for large reaction rates the grid spacing must be exceedingly small. This suggest a grid refinement to completely negate the source term error is not practical. Therefore, all that can be concluded from the results here is that the grid is adequate from a fluid dynamics perspective.

5.1 Comparison of Solution Methods

Next the fully implicit and splitting solution methods described in Chapter 3 are compared. This is done in part to verify the splitting scheme can be used for the remainder of the computations which is desired given its reduced computational requirements. Of course the predominant question is whether the splitting technique is unsatisfactory in its coupling of the fluid dynamics and chemical reactions. If such inconsistences exist, they

should be evident in both steady and unsteady computations. Here we compare the fully implicit and the splitting schemes for the steady-state shock-induced combustion case at M=6.46. It is worthwhile to first consider what sort of anomalies in the final steady-state solution would be expected if indeed the splitting scheme failed. Considering the governing equations of the problem, a steady-state solution, $\partial Q/\partial t = 0$, implies the convective terms and source terms balance whether the fully implicit or splitting scheme is used. The current computations are inviscid so the diffusive terms are neglected. If the steady-state solutions from each scheme do not match, then the splitting scheme has misrepresented these terms in some way even though they balance. Such errors should be evident in the dependent variables.

Figure 5.5 shows a comparison of the densities computed using the fully implicit and splitting schemes. Both computations have been carried out on the 80x120 grid and using the 7-step mechanism. If the splitting scheme did introduce any anomalies, they would be manifested in a discrepancy in the variation of species which in turn would impact the
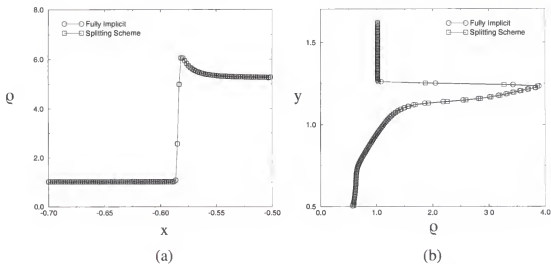
Figure 5.5. Comparison of computed density from the fully implicit and splitting schemes, (a) along the stagnation line and (b) along x=.5.

calculation of the source term and finally the densities. Therefore, the splitting scheme as implemented proves adequate in solving the steady-state problems. This also increases the confidence in using such a scheme for unsteady calculations since the problem of artificially convecting species at incorrect speeds should appear in the steady-state problem as well.

5.2 Source Term Treatment

Here the various source term treatments discussed in Chapter 3 are evaluated. These various techniques are efforts to compensate for the error introduced in the representation of the source term which has been shown earlier. In addition to the source term treatments evaluated here, the two other leading options for addressing this error are the solution of the logarithmic form of the equations and the grid adaptation techniques. The source term modification has been chosen to be evaluated here given the fact that of the three alternatives, this is the easiest to integrate into existing simulation tools. The comparisons carried out here are to not only compare the various schemes but also to see how the source term treatments affect the computed flow field.

Figure 5.6 shows the computed density field using the various treatments on the baseline 80 x 120 grid with the 7-step mechanism. All treatments produce similar results as is also evident in Figure 5.7 which shows a comparison between the density variations along x=.5 and x=.7. The comparison includes computations using the baseline model, with no modification to the source term, and the results using the scaling factors proposed by Shang et al. (1995) and Sussman (1993) as well as the current scaling factor of Eqn. (3.77). The computed fronts using all three techniques are essentially indistinguishable. Even though the current scaling factor, Eqn. (3.77), is based on the same error estimation proposed by Sussman (1993), the new weighting function is dependent on the curvilinear mass flux rather than the Cartesian velocity components. This alteration has been made given the fact that the error is introduced through the discretization and in the case of a curvilinear finite volume method, this is done in the curvilinear frame of reference. In Sussman's (1993) computations, the scaling factor is applied to only a subset of the species, primarily the

Piecewise constant

Log Interpolation, Eqn. (3.40)

Sussman's scaling, Eqn. (3.57)

Current Scaling, Eqn. (3.77)

● Experimental Shock Front; upper half
○ Experimental Energy–Release Front; upper half
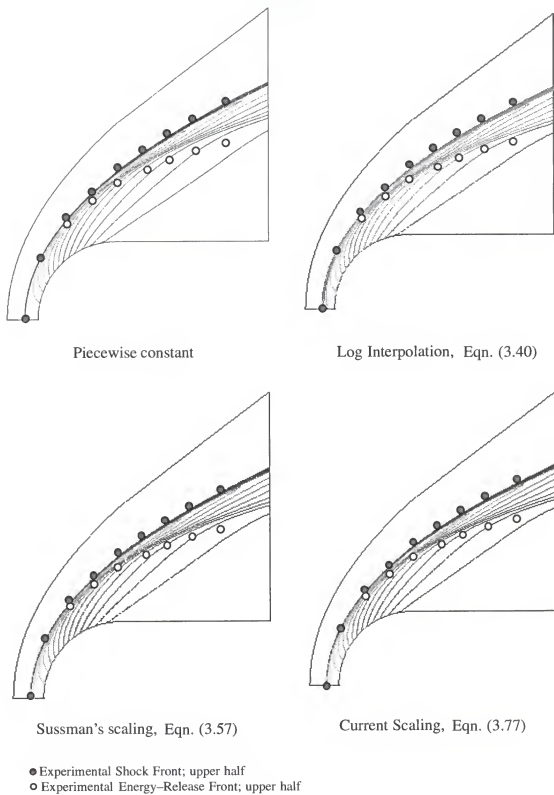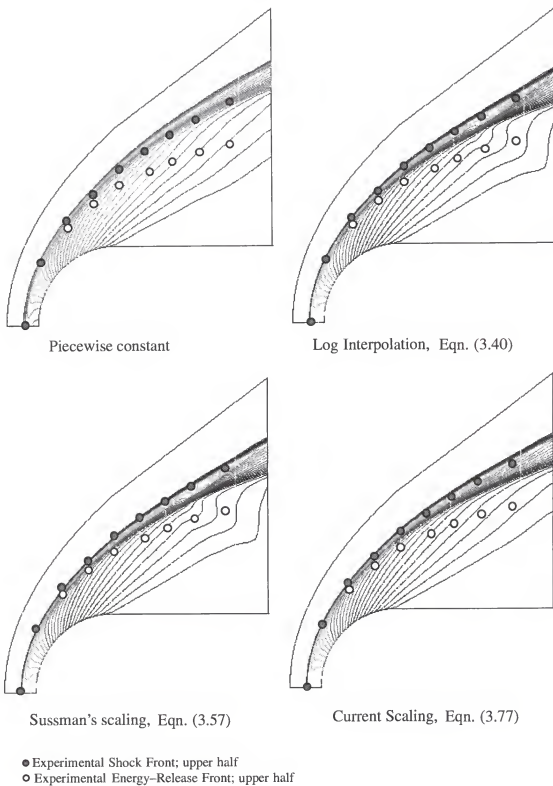
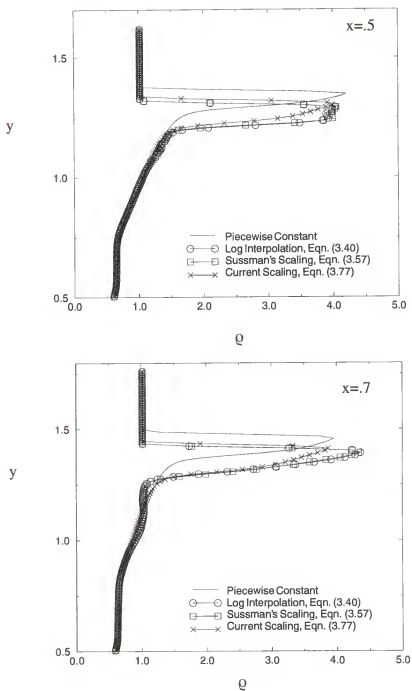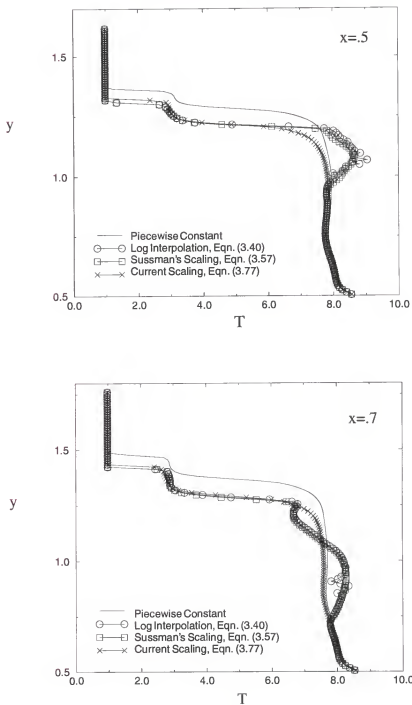Figure 5.6. Density contours using the 7-step mechanism along with various source term treatment schemes.
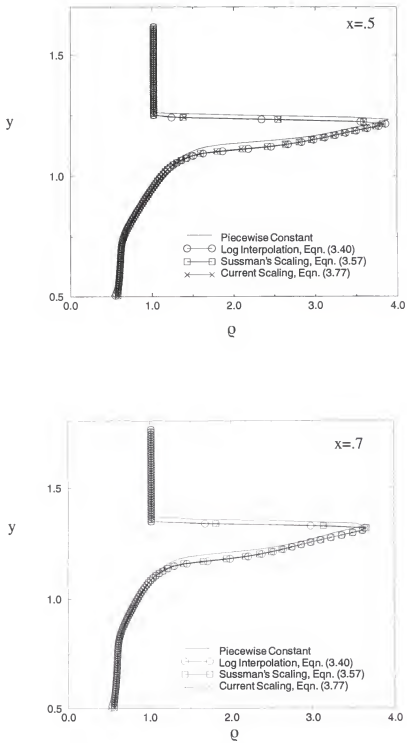
Figure 5.7. Density variations along a line normal to the body at x=.5 and x=.7 from various source term treatments using the 7-step mechanism.

radicals. In the current study, his scaling has been tested in this manner as well as applying the scaling to all species. The results are indistinguishable.

As is seen in both the contours of Figure 5.6 and the traces of Figure 5.7, the modified source term does impact the shock and reaction front location. Also, the thickness of the reaction zone is impacted and the curvature at the baseline of the projectile is somewhat different and more in line with the experimental results. The most attractive aspect of the source term modification scheme is the fact that improved accuracy is achievable without modifying the grid and with minimal alteration to the governing equations. It is also of note that all schemes evaluated give comparable results which indicates any correction for the discretization error is an improvement beyond the piecewise constant model. We next see if this is true when a higher order mechanism is used.

Next the source term treatments are evaluated using the 32-step mechanism with the rate for $H + O_2 \leftrightarrows OH + O$ suggested by Warnatz (1984). Figure 5.8 shows the computed density fields using the various treatments. The first noticeable aspect of the solution is the difference between the piecewise constant results when the 32-step mechanism is used when compared to the 7-step results. This is investigated more after the comparison of the source term treatments. The density contours show all treatments do cause the fronts to be oriented closer to the projectile and the predominant gradients are at similar locations. However, there seems to be some abnormality in the region between the shock and energy release front when the schemes by Shang et al. (1995) and Sussman (1993) are used. This can be seen clearer in specific traces of density and temperature.

Figure 5.9 shows a comparison in the density variation at x=.5 and x=.7. It is clear that all three schemes do produce a change in the location of the fronts in a similar manner. However, the interpolation scheme by Shang et al. (1995) and Sussman's (1993) scaling factor alter the profile behind the shock. This is also very clear in the temperature profiles of Figure 5.10. In the case of the logarithmic interpolation, the computations using the 7-step and 32-step mechanisms also show some oscillations in the contours of the intermediate

Piecewise constant

Log Interpolation, Eqn. (3.40)

Sussman's scaling, Eqn. (3.57)

Current Scaling, Eqn. (3.77)

● Experimental Shock Front; upper half
○ Experimental Energy–Release Front; upper half

Figure 5.8. Density contours using the modified 32-step mechanism along with various source term treatment schemes.

Figure 5.9.   Density variations along a line normal to the body at x=.5 and x=.7 from various source term treatments. The 32-step mechanism with the modified rate for $H + O_2 \leftrightarrows OH + O$ is used.

Figure 5.10. Temperature variations along a line normal to the body at x=.5 and x=.7 from various source term treatments. The 32-step mechanism with the modified rate for $H + O_2 \leftrightarrows OH + O$ is used.

species. This is thought to be due to the fact that no limiting process is used when calculating the higher order variation in species. In the case of the scaling by Sussman (1993), a criterion is used to ensure the scaling factor is always less than or equal to unity, so the abnormalities are most likely due to the inconsistencies in using the Cartesian velocity components in the weighting function but the contravariant velocities in the upwinding. It is noted that the current scheme, Eqn. (3.77), displays a much better convergence history than the other two schemes. As in the case of the 7-step results, the modified source term treatments do bring the computed front locations more in-line with the experiments. However, the 32-step results are still quite different from those achieved with the 7-step model and the experimental data.

It should be noted that Wilson and Sussman (1993) employ the 32-step model to compute the M=6.46 shock-induced combustion case using the logarithmic form of the governing equations on a 52 x 52 grid which is rather coarse compared to the current 80 x 120 grid. A good comparison to experimental data is achieved. However, the logarithmic equation set represents a nonlinear transformation of the original equation set and is found to result in an overprediction of the induction zone if too course a grid is used. Therefore, it is difficult to determine the relative roles of the mechanism and grid in determining the close comparison with experimental results without a systematic grid refinement study using the transformed equation set.

Wilson and MacCormack (1990) also use the 32-step mechanism to compute the M=6.46 case captured by Lehr (1972) on an adapted 321 x 65 grid using the piecewise constant source term representation. Good agreement between the computed density field and the experimental data is shown, although no systematic grid dependency test has been conducted. Given these earlier studies using the 32-step model, there is some question as to the failure of the current computation using the 32-step model with the scaled source term treatments to match the experimental results. It has been pointed out that the refinement can be judged to be fine enough only from a fluid dynamics standpoint but not from the chemical kinetics aspect. However, significant insight into the role of the reaction mechanism can be

gained by assessing the difference between the 7 and 32-step results using the present solution method.

5.3 Effect of Reaction Mechanism on the Computed Flow Field

It has been seen in the computed density fields used in the evaluation of the source term treatments that the difference between the 7 and 32-step results are quite noticeable. Therefore, here various reaction mechanisms are used in an effort to draw correlations between the characteristics of the mechanisms and the computed flow field. The computations are carried out using the piecewise representation of the source term to ensure any differences are due only to the reaction mechanism. In addition to the 7 and 32-step models already presented, mechanisms composed of 2, 8, and 19 steps are also evaluated. The mechanisms are presented in Tables 2.1, 2.2, 2.3 and 2.7. The 19-step mechanism is simply a subset of the 32-step mechanism and is steps 1 through 19 in Table 2.7. This results in a mechanism which neglects the nitrogen reactions and has been used by Matsuo et al. (1993).

The computed density field using the 2-step mechanism is shown in Figure 5.11. The computation has been carried out over half the domain but the complete domain is used for presentation. This mechanism gives no induction delay and the reaction front is indistinguishable from the shock. Also, the heat release immediately behind the shock causes the shock to be pushed out to the boundary of the computational domain. This process is similar to the runaway detonation captured by Lehr (1972) for certain shots into hydrogen-oxygen mixtures. However, more study is needed to draw any detailed correlation between the two cases. It is difficult to draw any conclusions as to the relative effect of induction and reaction time using this mechanism. Therefore, for the remainder of this study, focus is placed on the results using the other mechanisms.

Density contours from the computations using the other reaction mechanisms are shown in Figure 5.12. All computations have been carried out on the 80x120 grid. The 7-step results compare most favorably with the experimental data whereas the 8-step results also
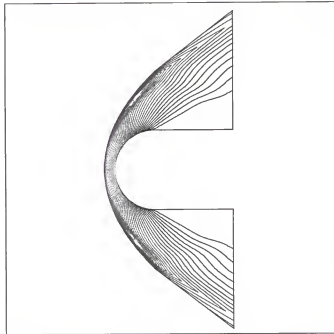
Figure 5.11. Density contour from the computation using the 2-step global mechanism for the M=6.46 case.

show a similar structure and a distinct shock and reaction front. However, their locations are somewhat closer to the projectile than indicated by the experimental data collected by Lehr (1972). Two 32-step models have been used with the difference being the rate used for the reaction $H + O_2 \leftrightarrows OH + O$. The baseline 32-step model uses the rate suggested by Jachimowski (1988) where as the modified 32-step model refers to the rate suggested by Warnatz (1984). It is clear that both 32-step models produce shock locations further from the projectile than the 7 or 8-step models and the experimental results. Also, the zone between the shock and energy-release front are much smaller. It is of note that when the rate of the branching reaction is altered, the overall results are somewhat difference. The 19-step results are not included in the comparison since the computations using the 19-step model are found to be essentially identical to those use the 32-step model. From an application standpoint, this suggest the nitrogen reactions are not essential for the M=6.46 flow conditions.

7–step

8–step

32–step

Modified 32-step

● Experimental Shock Front; upper half
○ Experimental Energy–Release Front; upper half
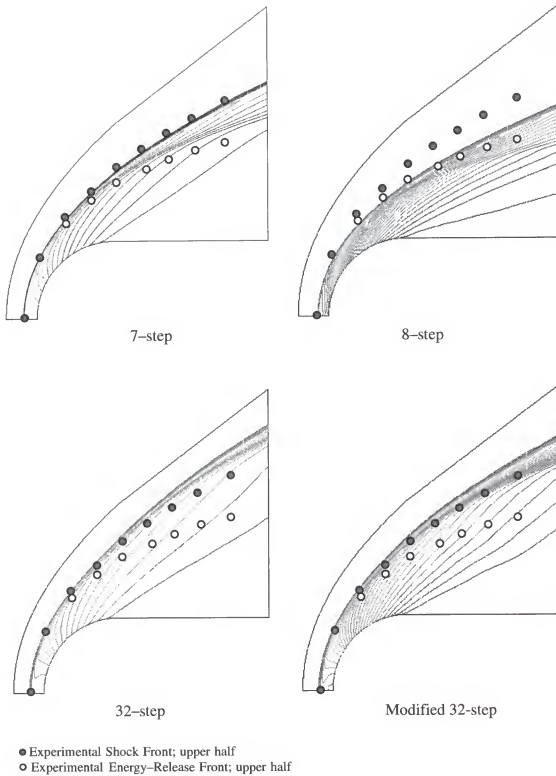
Figure 5.12. Density contours from the various reaction mechanisms for the M=6.46 case using the standard piecewise constant source term.

A detailed comparison using contours is difficult so the variation normal to the projectile body is used and presented in Figure 5.13. Here the variations in temperature
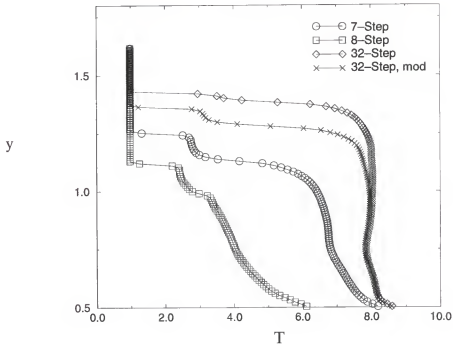
Figure 5.13. Lateral Variation in Temperature Computed With the Various H_2 / Air Mechanisms. Location is One Radius Downstream of Nose / Body Junction.

normal to the body computed by the various mechanisms are shown. The location of the traces is at a constant x of one radius downstream of the hemispherical nose-cylindrical body junction. At these locations, a distinct zone between the shock and energy-release fronts is evident in the temperature profiles for the 7, 8, and modified 32-step mechanisms. For the baseline 32-step model, there is a slight inflection point in the profile but no significant zone is detectable. These results are consistent with the contours of Figure 5.12. The lower temperatures seen by the 8-step which has a slower heat release rate is similar to the effects seen by Lee and Deiwert (1989) when they reduced all the rates in their 8-step mechanisms by 2 orders of magnitude. Also, the wall temperatures from the current calculations are in line with the value calculated by Lee and Deiwert (1989). Comparing the results using the

two 32-step mechanisms shows the modification in the rate for $H + O_2 \rightleftarrows OH + O$ produces a change in the profile such that a distinct zone between the shock and reaction front is evident. However, the final wall temperature produced by both is the same due to the similarity in the heat release rates.

It is useful to analyze the temperature variation normal to the body at other locations. Therefore, Figure 5.14 shows the variation in temperature along the stagnation line
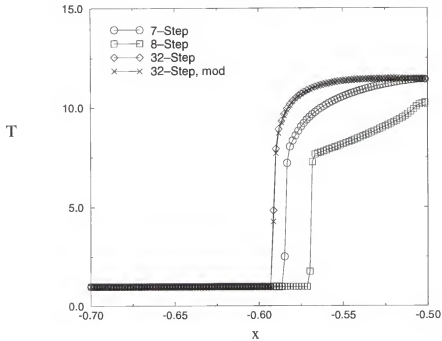
Figure 5.14. Variation in Temperature Along the Stagnation Line Computed With the Various H_2 / Air Mechanisms.

computed with the various reaction mechanisms. The first noticeable effect is the impact the heat release rates of the various mechanisms has on the shock standoff distance and wall temperature. The location x/d=−.5 corresponds to the stagnation point on the projectile. The temperature computed at the stagnation point using the current 7 and 32-step mechanisms are very similar to those computed in the previous study by Yungster et al. (1989) for the M=6.46 case. No plateau in temperature denoting the induction zone is seen in the profiles

for any of the mechanisms. This is unlike the profiles seen in the lateral field presented in Figure 5.13. Also, the results by Wilson and MacCormack (1990) for the Lehr problem at M=5.11 show a distinct induction zone on the stagnation line using the 32-step mechanism on an adapted grid. It is of interest to note that even though the induction zone is not resolved in this region of the flow field, the overall appearance of the density field matches those of the experiments when the 7-step model is used.

A comparison between the various mechanisms is made difficult first due to the fact that the resulting flow field structure such as the shock shape and location differ from solution to solution. This is evident in the density contours from the reacting cases as well as the nonreacting scenario presented in Figure 5.15. The 7-step and the two 32-step models are highlighted in the following analysis. The chemical reaction processes key in determining the overall combustion flow field are initiated by the temperature elevation produced by the shock. Therefore, the shock location in the flow field and the shock angle relative to the incoming flow is key since shock angle determines the conditions behind the shock and shock location determines where these jump conditions are applied. Based on these facts, shock angle relative to the incoming flow is used as a variable in the analysis procedure. Figure 5.16 shows a temperature-pressure space plot denoting the variation of both temperature and pressure behind the shock in the nonreacting M=6.46 case as a function of wave angle, β. The wave angle is defined such that $\beta = 0°$ corresponds to the stagnation line where the shock is normal to the incoming flow. To compare the various mechanisms, conditions corresponding to wave angles of $0°$, $20°$, $40°$, and $60°$ are used.

Figure 5.16 shows the results from the computational model compare well to the theoretical values for $\beta > 40°$. The discrepancy for angles less than that is due to the fact that the computational model, even for the nonreacting case, does include the dependence of specific heat of temperature. Therefore, in the nose region where temperatures are very high, these effects are evident. To incorporate these effects into the comparison of the reaction mechanism, flow field properties corresponding to the four locations in
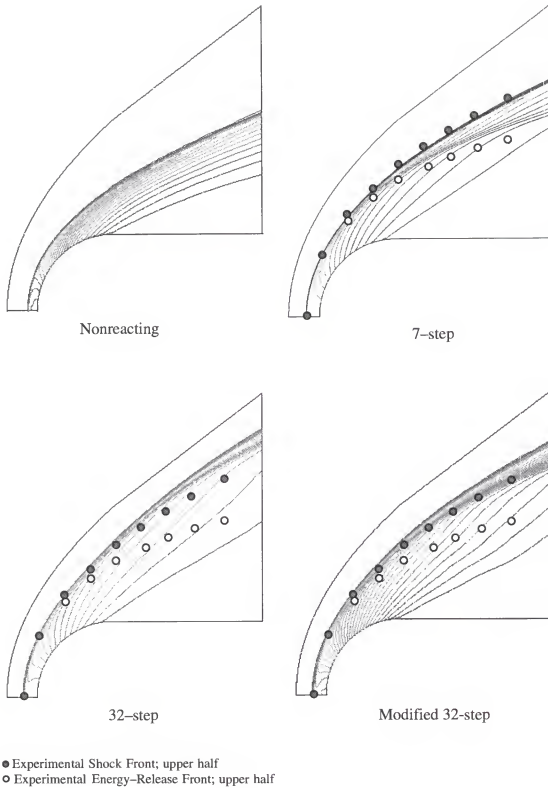
Figure 5.15. Shock locations and shapes produced by reacting and nonreacting models for the M=6.46 case using the standard piecewise constant source term.
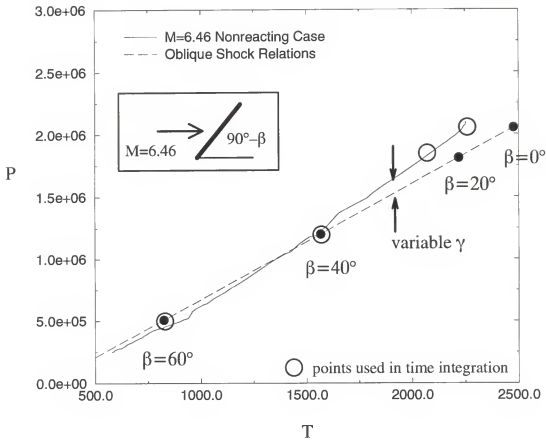
Figure 5.16. Conditions behind computed shock using current computational model and adiabatic oblique shock relationships for M=6.46.

temperature-pressure space denoted by open circles are used. Therefore, the conditions labeled 0° and 20° in the following analysis have pressures approximately equal to that calculated using the oblique shock relations but temperature values based on the computed nonreacting M=6.46 scenario.

　　　To compare the various reaction mechanisms using the various β conditions a method is needed by which to characterize each model. The key characteristics of any reaction mechanism is the time scales it reproduces and the accuracy of a given mechanism when compared to experimental results is dependent on these scales. Time scales associated with

chemical reactions are typically measures of characteristics in the temperature and species temporal profiles. Here, as in previous studies by Wilson and MacCormack (1990), Matsuo et al. (1993), Matsuo and Fujiwara (1993), Matsuo and Fujii (1995), and Matsuo and Fujii (1996a), the temperature profiles resulting from the combustion process are analyzed to determine correlations between their characteristics and the combustion flowfield. There are practical reasons to use temperature, the first being that the various reaction mechanisms many times assume different chemical compositions and intermediate species. Therefore a comparison of temperature profiles is more straight forward and encompasses the effects of the various reaction paths. Also, for a practical application, if a reduced mechanism can be used to model the same important chemical time scales, the computational time required for a useful simulation is greatly reduced. Furthermore, for various applications such as pre-design or for specific problems, issues may limit the information available as to the detailed composition of the chemicals being studied. Only more general information such as the induction time and heat release rates may be available. This is another reason to investigate the correlation of global aspects of the chemical characteristics to the resulting combustion scenario.

To characterize the various reaction mechanisms, analysis similar to that carried out by Matsuo and Fujii (1996a) is performed here. A zero-dimension time integration of the species conservation equations is performed neglecting convection and diffusion. The integration is carried out assuming total density and internal energy are constant. The initial conditions for the integration are taken to be those behind the shock at $\beta = 0°$, $20°$, $40°$, and $60°$. The temperature time histories from the 7, 8, 32 and modified 32-step mechanisms are shown in Figures 5.17 and 5.18. The 2-step mechanism is not included given its behavior shown earlier. It is important to note the x axis for the $\beta = 60°$ is a logarithmic scale. This indicates at these initial conditions, the induction time for the 32-step models is orders of magnitude larger than those of the 7 and 8-step mechanisms.
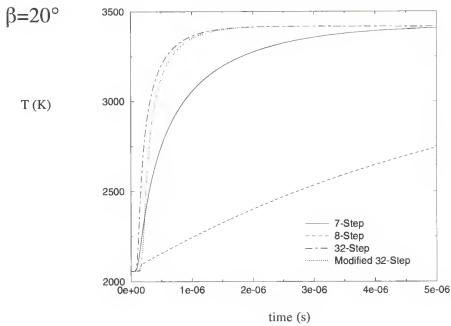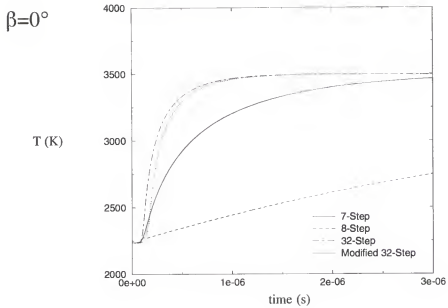
Figure 5.17. Temperature time history from the zero-dimension integration for the M=6.46 case using the 7, 8, and 32-step mechanisms at $\beta = 0°$ and $20°$.
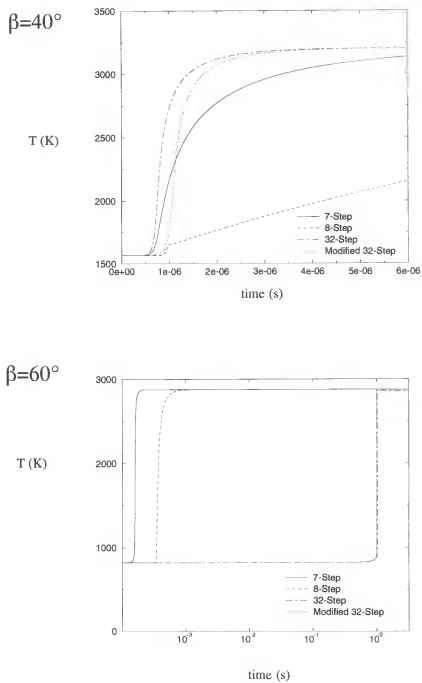
Figure 5.18. Temperature time history from the zero-dimension integration for the M=6.46 case using the 7, 8, and 32-step mechanisms at $\beta = 40°$ and $60°$.

Two key temporal scales associated with the chemical reactions are the induction time and the heat release rate, or reaction time, as found by Wilson and MacCormack (1990), Matsuo et al. (1993), Matsuo and Fujiwara (1993), Matsuo and Fujii (1995), and Matsuo and Fujii (1996a). This is true for both steady and unsteady combustion cases. Here the investigation focuses on the steady shock-induced combustion scenario captured by Lehr (1972). One goal of the current study is to determine the roles of these mechanism characteristics in determining the combustion scenario. To facilitate comparison of the current results with other studies, the definitions of these two scales must be well annotated. In their zero-dimension analysis, Sussman (1994) and Matsuo and Fujii (1996a) defined the induction time and time of reaction in similar fashions using the maximum temporal derivative of temperature. Here, the induction and reaction time are defined as by Sussman (1994),

$$\tau_{ind} = t_m - (T_m - T_0)/\left(\frac{dT}{dt}\right)_{max}$$

$$\tau_r = (T_\infty - T_0)/\left(\frac{dT}{dt}\right)_{max}$$

(5.34)

where t_m denotes the time when $\left(\frac{dT}{dt}\right)_{max}$ occurs, T_0 is the initial temperature, T_m is the temperature at t_m and T_∞ is the final temperature. Using these definitions the induction times and reaction times at the various wave angles are presented in Figures 5.19 and 5.20 respectively. Two graphs are shown in Figures 5.19, one using a logarithmic scale and one linear, to highlight the variation at lower values of β and dramatic difference at higher values of β.

It has been shown that a key parameter in quantifying high-speed flows is the Damköhler number, the ratio between fluid dynamic to chemical time scales. Therefore, a Damköhler number is calculated here based on the conditions for the various shock angles. The fluid dynamic scales is defined using the diameter of the projectile and the velocity magnitude behind the shock ($|\bar{u}_2|$) while induction time is used as the chemical time scale,
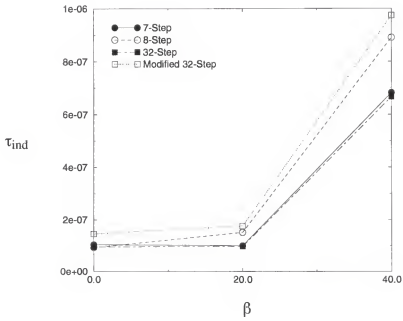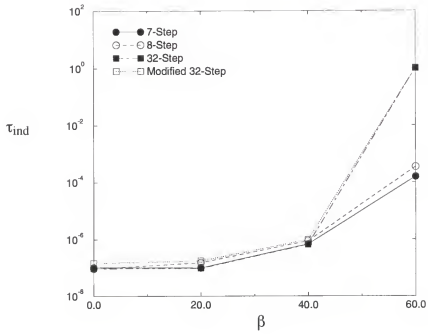
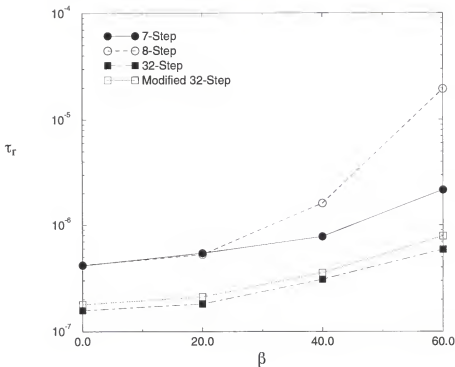Figure 5.19. Induction times produced by the different mechanisms for various shock angles.

Figure 5.20. Reaction times produced by the different mechanisms for various shock angles.

$$\mathfrak{D}_\beta = \tau_f/\tau_c = \left(d/|\vec{u}_2|\right)/\tau_{ind} \, . \tag{5.35}$$

The variation in the fluid dynamic time scale and the resulting Damköhler number as β increases is shown in Figure 5.21. As $\mathfrak{D}_\beta \to 0$ the time it takes for the chemical reactions to be initiated is much larger than the resident time of the fluid. For the shock-induced combustion flow scenario, if τ_f is defined appropriately, there is a critical value of β above which the chemical reactions are essentially turned off. The variation of $\mathfrak{D}_\beta$ with increasing shock angle is rather smooth in the case of the 7 and 8-step models but for the 32-step mechanisms, a sudden decrease is seen between 40° and 60°. Note, a logarithmic scale is used for $\mathfrak{D}_\beta$. Results from the 7, 32, and modified 32-step models are analyzed here to
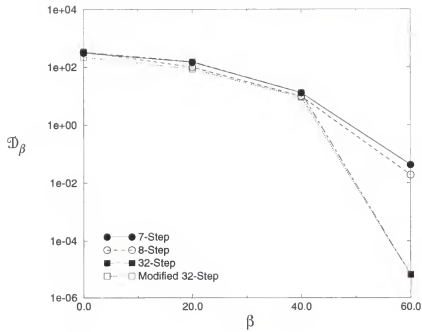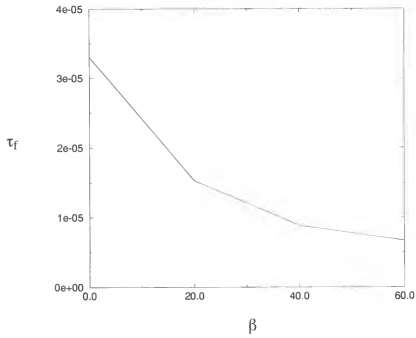
Figure 5.21. Fluid dynamic time scale and Damköhler number at various shock angles.

establish any correlation between the Damköhler parameter, $\mathfrak{D}_\beta$, and the computed flow field.

The premise that the computed flow field is dependent on $\mathfrak{D}_\beta$ is supported by the streamlines of Figures 5.22, 5.23, and 5.24 which are shown along with the corresponding
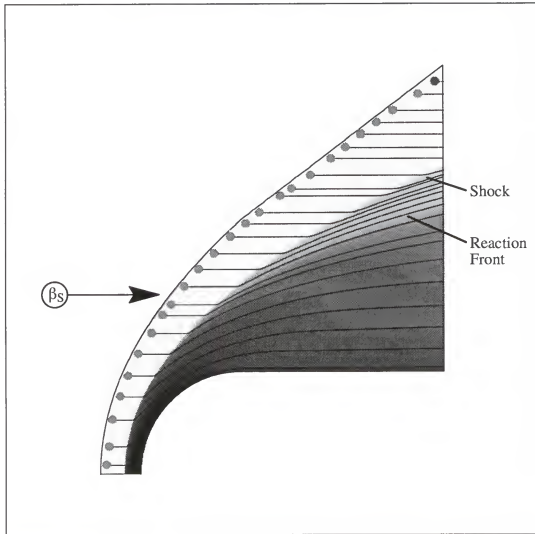

Figure 5.22. Streamlines and temperature field produced using the 7-step model.

temperature contours. In all cases the region between the shock and energy release front is denoted with light gray shading. This allows an estimation of the point where the two fronts begin to deviate and the corresponding shock angle. This separation point is highlighted
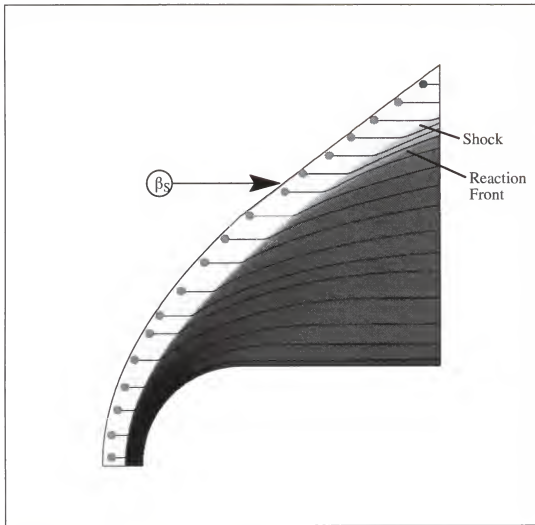
Figure 5.23. Streamlines and temperature field produced using the 32-step model.

since it is a predominant feature of the flow field and impacts the location of the fronts downstream. In the case of the 7-step model, the separation point occurs at a value of approximately $45°$. For the 32-step model, the value is approximately $50°$ with the value dropping back to $45°$ for the modified 32-step mechanism.

For all three cases it is clear that those streamlines which cross the shock outboard of the separation point do not cross the energy release front but remain in the zone between the two fronts. The separation point and position at which the streamlines begin to fail in
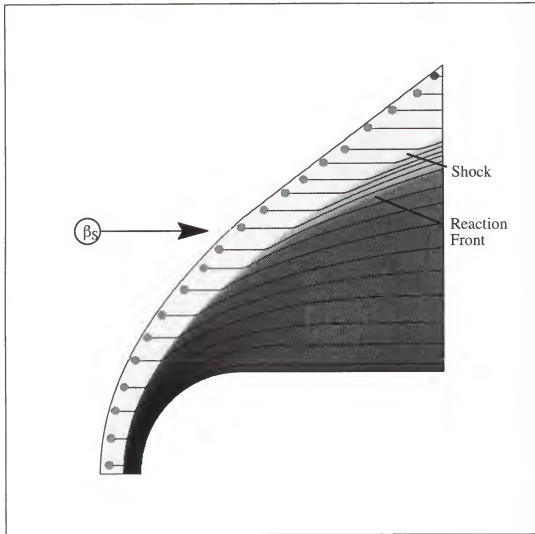
Figure 5.24. Streamlines and temperature field produced using the modified 32-step model.

crossing both fronts do not coincide exactly. However, the size of the zone between the shock and energy release fronts and this critical value of shock angle, β_S, are clearly dependent on the reaction mechanism. For fluid particles which cross the shock at locations for which $\beta > \beta_S$, the induction time is such that the mixture of hydrogen and air do not have time to react and are simply convected downstream.

For the shock-induced combustion scenario simulated here, the critical value of Damköhler number at which the reactions are essentially terminated is independent of the

particular reaction mechanism used. However, Figure 5.21 shows this threshold is traversed by either changing the dependence of τ_{ind} on β or by achieving larger values of β. The values of β for the 7-step computation range from 0° to approximately 70° which is due in part to the shock standoff in the nose region. Therefore, even though there is no sudden reduction in $\mathfrak{D}_\beta$ as β increases, the larger values of shock angle cause the production of a large zone between the shock and energy release front. In the case of the computations using the two 32-step models, the range of shock angles is 0° to approximately 60° and the reaction zone is highly dependent on the value of β corresponding to the critical value of $\mathfrak{D}_\beta$. Figure 5.21 indicates that when the rate for $H + O_2 \leftrightarrows OH + O$ is altered, the critical value of β is reduced. This results in a noticeable increase of the reaction zone evident in Figure 5.24.

The correlation between the rate of $H + O_2 \leftrightarrows OH + O$ and induction time is discussed next. However, first some conclusions can be drawn as to the performance of the various mechanisms in the nose region. The computed flow field when the 7-step mechanism is used does compare well with the experimental data captured by Lehr (1972). The results here suggest to produce an accurate simulation requires a correct reproduction of the shock location and shape, i.e., correct values of β. These shock characteristics are driven first by the shock standoff on the stagnation line and next by the curvature of the shock as you move away from the stagnation line. Figure 5.14 shows that, when compared to the 7-step results, the 32-step mechanism produces a much larger shock standoff which is due to the heat release rate generated by the model. The heat release rate also determines the shock curvature and all indications of the current study are that the 32-step mechanisms produce heat release rates larger than those which actually exist. A similar conclusion is made by Sussman (1994) for the 19-step reaction mechanism he uses to simulate the unsteady shock-induced combustion cases captured by Lehr (1972). As detailed in the literature review presented earlier, this conclusion is based on the modeled transition Mach number from the unsteady to the steady combustion scenario. The 19-step model used by Sussman (1994) produces heat release rates similar to the current 32-step model which, based on the computed shock

location and shape, is larger than that actually seen in the experiments. This is not to say the heat release rate is incorrectly modeled for all pressure and temperature conditions, but suggests for the higher regime more investigation is needed.

5.3.1 Pressure Effects on Reaction Rates

It is clear the computed flow field is dependent on the induction time produced by the reaction mechanism. Also, the 32-step mechanism is seen to have a sudden increase in induction time for certain values of pressure and temperature. These values are correlated to the rate of the reaction $H + O_2 \leftrightarrows OH + O$ given the fact that altering the rate of this reaction changes the induction time. This can be explained by considering the concept of the second explosion limit which is know to impact ignition delay (Oldenborg et al., 1990) and to be dependent on temperature and pressure. The reproduction of the second explosion limit by any reaction mechanism used is dependent on the rates associated with reactions

$$
\begin{align}
&\text{(br)} \quad H + O_2 \leftrightarrows OH + O \\
&\text{(tr)} \quad H + O_2 + M \leftrightarrows HO_2 + M
\end{align}
\tag{5.1}
$$
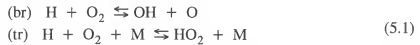
where reaction (br) is chain-branching and (tr) chain-terminating. In the current study, the chain-terminating step does not even appear in the 7-step mechanism and the modified 32-step mechanisms alters only the rate associated with the chain-branching step. Therefore, it is insightful to compare the explosion limits generated by the three mechanisms.

The second explosion limit in temperature-pressure space for the present simulations is depicted in Figure 5.25 along with an indication of where the oblique shock curve lies in temperature-pressure space. Even though the terminology of explosion is used, the combustion process on both sides of the limit is governed by the finite rate chemical processes defined earlier with the major difference being the ignition delay increase seen above the limit.

The curve denoting the second explosion limit is determined by the point where the rate of formation of free valences by the branching reaction balances the rate of removal of
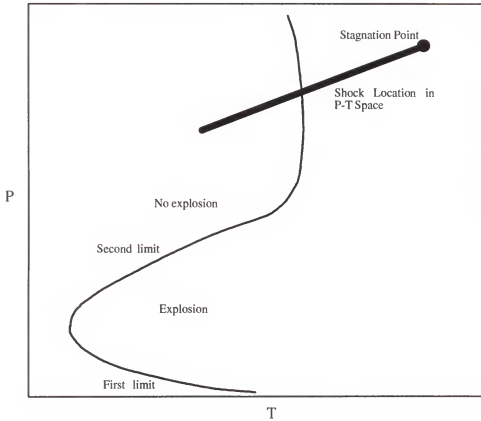
Figure 5.25. Depiction of the extrapolation of the second explosion limit into the regime of interest for the shock-induced combustion experiments.

these valences by the terminating reaction. In terms of the reactions in Eqn. (5.1), this is at the point where

$$2k_{br} = k_{tr}[M]_e \tag{5.2}$$

which can be used to determine the pressure corresponding to the second explosion limit as a function of temperature since $[M] \propto P/R_u T$ (Lewis and von Elbe, 1961). The factor of 2 enters the relationship due to the fact that the OH and O produced by the chain branching step of Eqn. (5.1) is used in reactions

$$\begin{aligned} OH + H_2 &\leftrightarrows H_2O + H \\ O + H_2 &\leftrightarrows OH + H \end{aligned} \tag{5.3}$$

to generate 2 additional H.

The fact that the second explosion limit is dependent on both temperature and pressure is important in the context of the shock-induced combustion scenario given the

observed effect of the shock angle. It is clear from the data presented so far, such as the streamline plots, that the location where the energy release front begins to deviate noticeable from the shock is dependent on the induction time. This point of separation impacts the front location downstream and the overall accuracy of the computed flow field. Knowing that for conditions above the second explosion limit ignition delay becomes long, the point along the shock at which this occurs is important.

The second explosion limit, in the context of a computational model, is determined by the selection of the reaction mechanism. Therefore, Eqn. (5.2) is used along with the relationship between third-body concentration and pressure to generate the limit curves, presented in Figure 5.26, produced by the 7, 32, and modified 32-step hydrogen-air mechanisms. In the case of the 7-step mechanism, the chain-terminating reaction is not included so a second explosion limit is not reproduced by the model. This is evident in the fact that there is no sudden increase in induction time for large shock angles. Therefore, the chain-terminating reaction of the 32-step model is used with the chain-branching reaction of the 7-step model to compare the difference in the rate of the branching reaction for the various mechanisms. Figure 5.26 shows that when the rate of the chain-branching reaction is altered, the location of the second explosion limit is shifted such that the shock curve crosses into the region of long induction delay earlier. This trend matches what is seen in the computed density and temperature fields presented earlier.

With the consideration of the modeled second explosion limit and the dependence of the overall computed flow field on this quantity, it is informative to review the derivation of the 32-step mechanism by Jachimowski (1988). In the derivation, after selecting the steps to be used in the reaction mechanism, the particular rate constants are refined to improve the comparison between calculated results and the experimental shock-tube ignition delay data reported by Slack (1977). The laminar burning velocity data assembled by Warnatz (1981) and reported by Milton and Keck (1984) are also used. The ignition delay produced by the mechanism is found to be highly sensitive to the reactions of Eqn. (5.1). Constants are
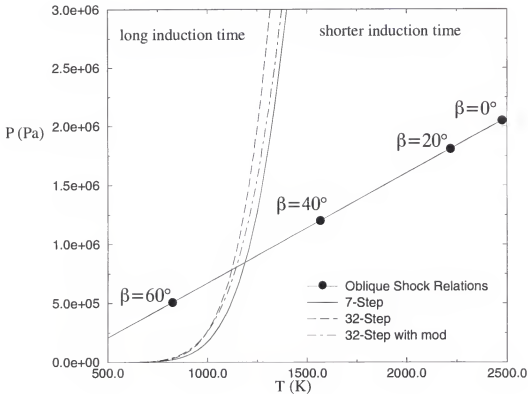
Figure 5.26. Explosion limits produced by the various hydrogen-air mechanisms and the location of the shock front in temperature-pressure space.

selected to give the best match to the experimental data, for a stoichiometric H_2-air mixture, in a temperature range of 700–1200 K and a pressure range of .5 to 2 atm. The burning velocities computed with the model for a stoichiometric H_2-air mixture compare well to the experimental data up to a pressure of 5 atm. In the region of 5 to 7 atm, the upper limit of the experimental data, the model under predicts the burning velocity. For the current shock-induced combustion case at M=6.46, the range of temperatures along the shock are approximately 600–2200 K and the pressure range is 2–20 atm. Therefore, the applicability of the mechanism, or any used in previous computations of the shock-induced combustion

scenario, is in question. This concern is not new but should be reiterated given the results of the current study.

It is evident that pressure effects on the reaction rates can be seen through the modeled second explosion limit. However, the reproduction of this limit is solely a function of the reaction rates as evident in Eqn. (5.2) and Figure 5.26. Therefore, it is worthwhile considering one possible source for the error manifested in the reaction rates at high pressure. Recombination reactions, such as the reaction $H + O_2 + M \rightleftharpoons HO_2 + M$ in the present problem, are known to be driven at different rates for low and high pressures (Gardiner and Troe, 1984). Reactions which exhibit this behavior typically require a third-body collision to provide the necessary energy for the reaction to occur in the low-pressure regime. This requirement is due to the fact that the time scale of the dissociation process, the reversal of the recombination, is much shorter than the time scale of the third-body collision. Therefore, in the low-pressure regime the recombination rate is directly proportional to the third-body which, as shown earlier, is directly proportional to the pressure. In the high-pressure regime, the third-body concentrations are such that the collision frequency is large compared to the dissociation rate and no pressure dependence is seen in the rate. Such a variation for a given reaction is depicted in Figure 5.27 where k_o and k_∞ are the low and high pressure limits respectively. The figure denotes the pressure dependence for a constant temperature so in pressure-temperature space, the rate of the reaction would be a surface. Both the low and high pressure limits of k can have an Arrhenius type form with the difference being the absence of the third-body concentration in the source term for high pressure. It is obvious from the depiction of Figure 5.27 that if the high-pressure effects are ignored, an overestimation of the chain-terminating rate is made. The pressure corresponding to the second explosion limit and the reaction rates are related as $P_e \propto 2k_{br}/k_{tr}$. Therefore, if the terminating rate is reduced the pressure limit increases which would cause the two fronts in the shock-induced combustion scenario to separate at a lower β and improve the comparison with experimental data. Alternate forms useful in representing the reaction rates which incorporate the
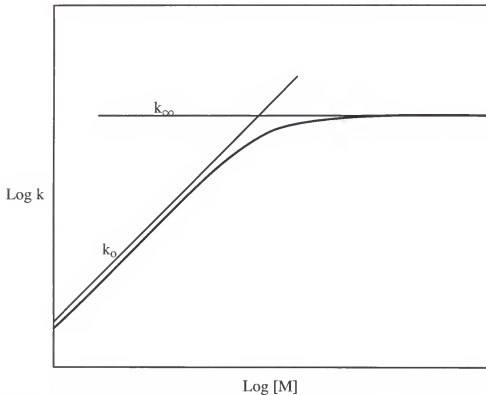
Figure 5.27. Depiction of the dependence of a single dissociation-recombination reaction on pressure at a given temperature.

transition from the low to high-pressure limit are discussed by Gardiner and Troe (1984). Based on the current study, it is clear that such alternatives should be investigated in the context of the shock-induced combustion scenario.

5.3.2 Summary of Reaction Mechanism Effects

Much attention has been placed here on the difference in the reaction mechanisms and particularly how these differences impact the computed flow field. Here a brief summary of these aspects is presented. The 7-step mechanism is seen to produce the best match to the experimental data in terms of the overall flow field. This is due in part to the computed shock location and shape which is dependent on the amount of heat release in the nose region and the interaction between pressure and the reaction rates. In the case of the 7-step model, there is a smooth change in induction time as the shocking angle varies, lowering the pressure and temperature behind the shock. The reaction time in the nose region is longer than that of the

32-step model, resulting in a shock with more curvature. This causes the induction time to exceed the resident time at a location such that the computed flow field compares well with the experimental data.

For the 32-step mechanisms, the shorter reaction time in the nose region results in a shock with less curvature. However, the sudden increase in induction time due to the second explosion limit is responsible for the overall character of the solution. It is clear that for both kinetics schemes, the zone between the shock and energy release fronts is a region, for all practical purposes, the reactions are "stopped" due to relatively long induction time. This is evident by the fact that beyond a certain shock angle, the fluid particles do not cross the reaction front. Therefore, the apparent reaction front observed is dominated by the chemical reaction in the nose region.

Given the current results and the findings of earlier investigations, there are some concerns as to the utility of the various mechanisms for shock-induced combustion calculations. This is due in part to the pressure and temperature range of the data used to deduce the rate constants used in the models. Therefore, more research needs to be conducted to investigate the higher temperature and higher pressure effects on the kinetic schemes.

5.4 Computations Using Turbulence Model

The final aspect of simulating the shock-induced combustion scenario to be assessed is the effect of the inclusion of the turbulence model. The key output from the turbulence model, when considering its effect on the computed flow field, is the turbulent kinetic energy, k, and the dissipation rate, ε, which combine to determine the eddy viscosity. This is of importance given the closures defined in Chapter 4 which relate the enhanced transport of species and heat to the turbulent viscosity. Also, the estimate of the temperature fluctuations and their impact on the reaction source term is directly dependent on k. No such quantities are available in the context of Lehr's (1972) experiments. Therefore, the computed values of k and ε, using the current multi-species code, are compared to these same

quantities from earlier computations using a perfect gas code for a similar flow scenario. The specific computations are presented in the work of Krishnamurty (1996).

The standard form of the k-ε model is used for the current set of computations. This is done in part to establish a benchmark case against which to compare future computations. Figure 5.28 shows the variation in the turbulent kinetic energy along the stagnation line for
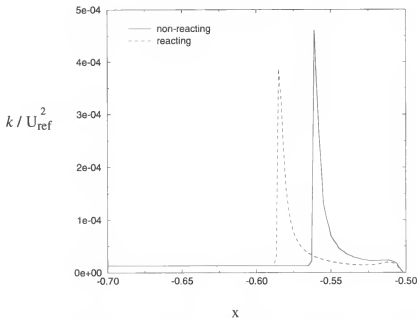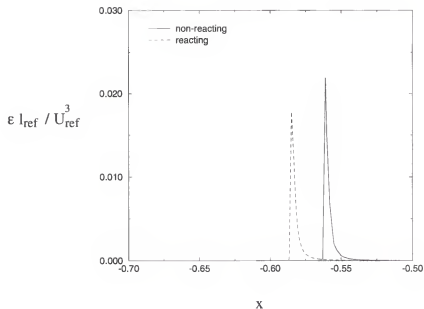

Figure 5.28. Variation in k along the stagnation line for both a non-reacting and reacting case of M=6.46 in a stoichiometric mixture of hydrogen and air.

both a nonreacting computation at M=6.46 and the current reacting case at the same Mach number. The computations with reactions have been performed using the 7-step mechanism with the source term treatment of Sussman (1993). The nonreacting case is also for a stoichiometric mixture of hydrogen and air. Figure 5.29 shows the corresponding values of the dissipation of the turbulent energy. The reference length used in nondimensionalization of the dissipation is $l_{ref} = d/2$ where d is the diameter of the projectile. In both Figure 5.28 and 5.29 the reference velocity is $U_{ref} = \left(M \sqrt{\gamma} \right)_{\infty}$. Both the magnitudes and profiles of k and ε are in-line with those of previous computations using a perfect gas model

Figure 5.29. Variation in ε along the stagnation line for both a non-reacting and reacting case of M=6.46 in a stoichiometric mixture of hydrogen and air.

(Krishnamurty, 1996). Similar profiles, peaks in k at the shock, are seen throughout the field. The grid used in the turbulent computations is the 80x120 grid presented earlier. This results in a y^+ of approximately 30 along the majority of the body except for a small region around the stagnation point.

The two goals pertaining to this portion of the current study have been first to couple the turbulence model with the multi-species fluid dynamic model and the finite rate chemistry model. The second has been to ascertain what impact an estimation of the turbulence has on the shock-induced combustion flow. The first goal has been met as is demonstrated by the computations presented here. Next, density and temperature profiles are used to quantify the impact of turbulence on the current flow scenario. The variation in density from the inviscid model, the computation using the standard k-ε turbulence model, and the simulation using this same model with the additional estimate for $\overline{\omega} = \overline{\omega(T + \delta T)}$ are shown in Figure 5.30. The profiles from both computation using the turbulence model
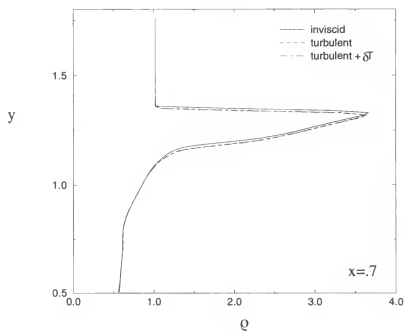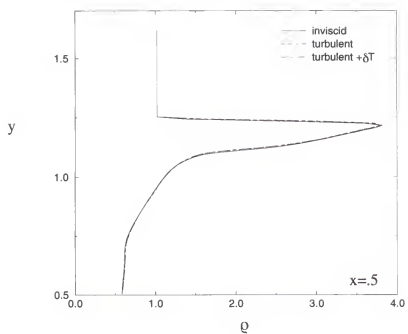
Figure 5.30. Density variations along a line normal to the body at x=.5 and x=.7 from the inviscid and turbulence models used with the 7-step mechanism and Sussman's source term treatment.

are indistinguishable. There is a slight change in these profiles from the inviscid calculation at the x=.7 location but nothing of significance. The complete density field from the computation using the standard k-ε turbulence model and the estimation for $\overline{\omega} = \overline{\omega(T + \delta T)}$ is shown in Figure 5.31.

Figure 5.31. Density field from computation using the standard k-ε turbulence model and the estimation for δT.
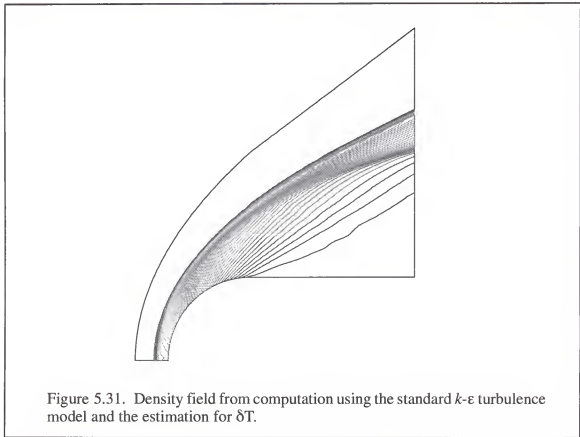
Figure 5.32 shows the variation in temperature computed with these same models. As in the case of the density profiles, the two turbulence computations are essentially the same and there is only a slight alteration from the inviscid computation. However, it is informative to highlight the temperature profile in the region of the shock and energy release front as is presented in Figure 5.33. At both x locations, the computations which include the model for turbulence has minimal impact on the shock location and, even though small, a more pronounced impact on the region between the initiation point and the final temperature. The profiles show that with the turbulence model included, the induction zone is slightly shorter which infers the enhanced transport of heat and species does impact the reaction
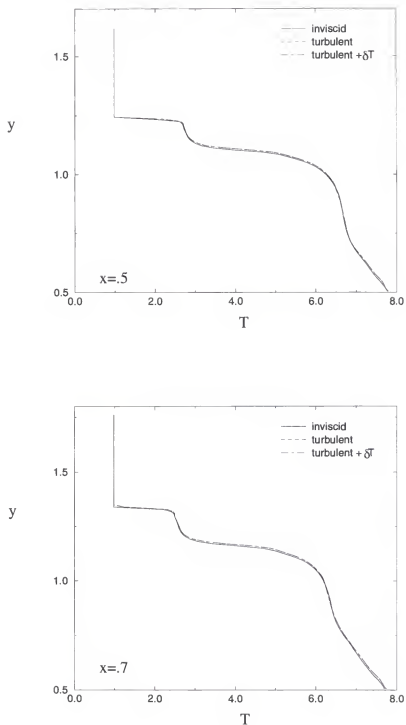
Figure 5.32. Temperature variations along a line normal to the body at x=.5 and x=.7 from the inviscid and turbulence models used with the 7-step mechanism and Sussman's source term treatment.

Figure 5.33. Temperature variation in the reaction zone along a line normal to the body at x=.5 and x=.7 from the inviscid and turbulence models used with the 7-step mechanism and Sussman's source term treatment.
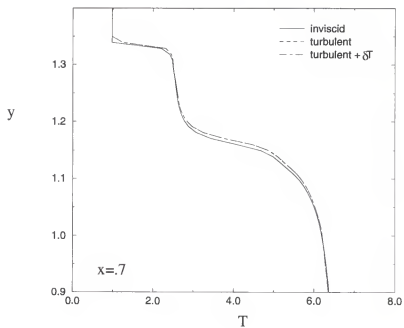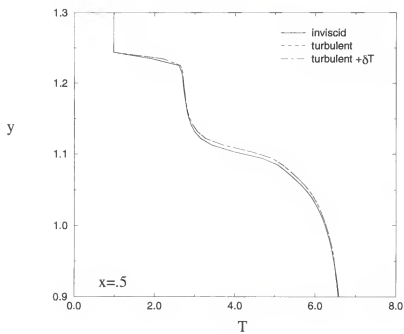
process. As is evident in the profiles presented here, the turbulence aspects of the current shock-induced combustion flow scenario are indeed secondary. This is not too surprising given the success of earlier inviscid computations of this same flow scenario.

5.5 Summary

In this chapter both the numerical and phenomenological aspects of simulating the shock-induced combustion scenario have been investigated. The numerical aspects which have been focused on are first techniques for addressing the known effect of grid resolution on the source term representation and second, solution methods for the governing equations. The phenomenological facets highlighted have been the reaction mechanisms and the role of turbulence. These aspects are summarized here in the context of the solution of the $M=6.46$ steady combustion case.

One of the first noticeable trends is that the resolution of the energy release front is highly dependent on the numerical aspects of the model. It has been shown that the predominate source of the error is due to the misrepresentation of the variation in the source term across a given computational cell. This can be addressed in one of several ways and the technique evaluated here is the scaling factor scheme proposed by Sussman (1993). The logarithmic extrapolation proposed by Shang et al. (1995) has also been evaluated but it is shown this technique can be cast in the same form as that proposed by Sussman (1993) and has similar effects. The scaling scheme produces good results when used in conjunction with the 7-step mechanism but produces less satisfactory results when the 32-step model is used. Also evaluated in this chapter is the Strang splitting scheme which has proven to give results comparable to the fully implicit scheme.

The comparison of the various reaction mechanisms shows the computed flow field is highly dependent on the modeled heat release rate and induction times. The conclusion that the 32-step mechanism produces heat release rates larger than those seen in reality is supported by the computed shock location and shape as well as the earlier work by Sussman (1994). Another key factor in determining the overall flow field is modeling where the

induction time of the reactions is much larger than the fluid dynamic time scale and this is seen to be dependent on the second explosion limit when the 32-step mechanism is used. In the context of the shock-induced combustion flow scenario, problems seem to be associated with the performance of 32-step mechanism at high pressures. High pressure effects are known to exist in various recombination reactions (Gardiner and Troe, 1984) which determine the second explosion limit. This indicates further investigation is needed into both the heat release rates and modeled second explosion limit. The earlier studies by Wilson and MacCormack (1990) and Wilson and Sussman (1993) and the current results suggest more investigation is needed to help separate the role of grid refinement and reaction mechanism in when the 32-step model is used.

The final aspect investigated in the context of the shock-induced combustion problem is the impact of the turbulence. Here a two-equation model, the standard k-ε turbulence model has been integrated with the multi-species fluid dynamics and finite rate chemistry models. An algebraic model for estimating the role of temperature fluctuations on the reaction source term has also been evaluated. For the current shock-induced combustion problem, these effects are found to be minimal. However, the computational code developed and tested here offers a solid tool for application to a wide range of problem scenarios and can be used to test the applicability of the k-ε model and the estimation for δT for alternate flow scenarios.

It is clear from the various aspects investigated here that both the numerical and phenomenological traits of the various models impact computational accuracy. It is also evident that for the various physical and chemical processes a range of models are available. When solving full scale engineering problems such as the munition scenario, represented here by the shock-induced combustion flow, a balance must be made between sophistication and efficiency. The code developed and described here strikes that balance by incorporating reduced kinetic schemes, by introducing the modified source term treatments, and with the incorporation of the two-equation turbulence model.

CHAPTER 6
GUN BLAST AND FLASH LITERATURE REVIEW

One of the munition problems of interest in the current effort is the phenomena of gun muzzle blast. The problem scenario has been described earlier and here a review of previous investigations into this problem is provided. This problem has been studied with both experimental and computational tools by several investigators. A comprehensive review of experimental and computational work addressing gun muzzle blast is provided in the compilations by Stiefel (1988) and by Klingenberg and Heimerl (1992). The majority of work in studying the blast signatures of conventional guns has employed experimental investigations. These investigations have been used to formulate some empirical models with which to estimate the overpressure signature generated by a given gun. These models are formulated for the bare muzzle configuration and prove unreliable if a muzzle device is used or in regions near the muzzle. Here a brief review of both experimental and computational work which is relevant to the current effort is provided. Those efforts which have focused primarily on the gas dynamics aspects are reviewed first followed by a review of the most notable work in computing flash. Finally, the advancements of the current model are detailed.

6.1 Gun Muzzle Blast

The experimental investigations into gun muzzle flows have used a wide variety of techniques to capture the pressure and temperature field as well as the velocity profiles. One example is the work by Klingenberg et al. (1983) in which pressure probes are used along with spectroscopy and Laser-Doppler velocimetry (LDV) measurements. Using pressure measurements, distinct features such as the precursor and main blast wave are detectable as

well as the gun gas / air interface and the shock disk which forms. The LDV measurements are useful in obtaining the turbulence intensities as well as other flow features such as the slip stream and shock disk. Such data is useful in developing theoretical models such as the work by Erdos and Del Guidice (1975). In their work, blast wave theory and unsteady shock-layer analysis are used to develop descriptions of the movement of key features such as the shock disk. Other modeling approaches (Fansler and Schmidt, 1983) use scaling parameters based on gun caliber and the energy output from the muzzle to predict the overpressure in the farfield around guns. Given the assumptions of these models, their utility is limited to bare muzzle configurations and distances far from the muzzle exit.

Investigations such as the work of Carofano (1993) into muzzle brakes show that the presence of any muzzle device drastically changes the overpressure field around the gun system. The overpressure signatures generated by devices using venting techniques, such as those tested by Carofano (1993), do not lend themselves to be easily represented with simplified analysis. In addition to venting devices, a popular muzzle device is that which is labeled a muffler. These are typically composed of a series of cavities such as the device depicted in Figure 6.1. The particular dimensions and configuration given are used later in
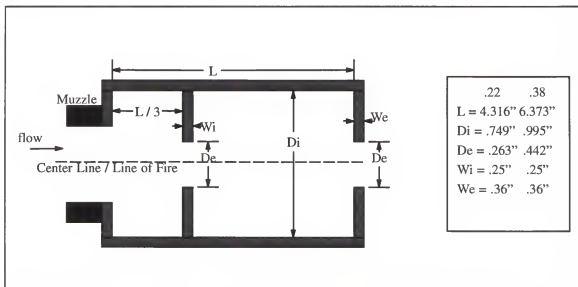

Figure 6.1.   Schematic of a cylindrical baffled suppressor typically termed a muffler. The dimensions (in inches) are for particular configurations used later.

the current study. Fansler and Lyon (1989) investigated various aspects of such muffler devices. Two parametric studies they have carried out had been to first keep the overall length of the device constant and vary the placement of a single internal wall to produce two cavities of different lengths. It is found that there are optimum sizes for the cavities. A similar conclusion can be drawn by studying the data presented by Fansler and Lyon (1989) from systematically increasing the number of baffles, keeping the overall length of the device constant. As baffles are added, the overpressures measured at various locations in the external field go down. However, there is a point at which the addition of baffles causes the overpressures to rise. This insinuates again that for a given gun system, i.e. muzzle exit conditions, there is an optimum cavity size below which the core flow from the muzzle does not have time to expand and the fluid dynamic processes which work to reduce the overpressures do not occur. It is to become clear that one of the key processes is the reflection of the blast waves off the face of the baffle walls.

As with the venting devices, the blast signatures from the muffler configurations are not predictable with simplified models. This is clear in the comparisons by Fansler and Lyon (1989) of their experimental measurements with predictions using a simplified expansion model. It is for this reason the gun blast problem has been addressed using computational techniques. Buell and Widhopf (1984) use a three-dimensional inviscid model to simulate the flow through a baffled muffler configuration. The computed peak pressures at various locations on the walls of the muffler compare fairly well with experiments. Computations with and without a model of the ammunition shell are presented. The presence of the shell routinely causes the computed peak pressure to be higher. No time dependent data or measurements in the exterior field are presented.

Carofano (1984) develops a computational model for gun muzzle flow which solves the axisymmetric Euler equations using Harten's Total Variation Diminishing (TVD) scheme. The flow is modeled as two ideal gases, one to represent the gun gas and the second to simulate the ambient air. This model is used by Carofano (1988) to simulate a cannon with

a perforated muzzle brake. The interior domain is simulated using a one-dimensional model with a source term to represent the venting holes. The exterior flow field is solved using the axisymmetric model incorporating the output from the one-dimensional model at the appropriate locations to simulate the venting holes. The results presented are computed density contours and shadowgraphs from the accompanying experiments and the general flow field features compare very well.

Fansler et al. (1990) use an inviscid model which also employs Harten's TVD scheme to simulate a multi-compartmented gun muffler. The computed pressure at several locations on the interior of the muffler walls is compared to experimental data. Time histories are provided for the computed pressures and other field quantities. The computations are reported to be in general agreement with the experimental data for the spatial locations nearest the gun muzzle and at times early in the flow field development. They attribute the differences to neglecting the reaction of the propellant with the air.

Carofano (1990) compares computations of a 20-mm and 105-mm cannon blast flow using both the Abel as well as the perfect gas equation of state with experiments. Both models give similar results for the computed overpressures with the perfect gas model giving slightly higher pressures for the larger gun. Carofano (1992) also presents computations detailing the time history of the blast associated with a small caliber cannon. The inviscid model used is seen to produce a secondary shock which is not present in experimental data. Carofano uses an ad hoc scheme which employs a first order flux representation in specific regions of the flow in an effort to mimic the dissipative processes. It is concluded that a more realistic model of the dissipative processes is needed. Carofano (1993) also presents an extensive comparison of computed and experimentally measured blast fields from venting devices. A variety of venting techniques are tested and the inviscid model does a reasonably good job of predicting the peak overpressures and the initial pressure signal at various locations.

It is clear from this brief review that investigations into the problem of gun muzzle blast have found computational tools useful and necessary. This is particularly true in the

cases where muzzle devices such as venting schemes and mufflers are used. Simplified models have proven to be limited in their applicability. The computations performed to date have used primarily inviscid models with fairly good success. However, it is clear from these earlier studies that some of the discrepancies between computations and experiments are attributed to the absence of any model of the dissipative mechanisms and the chemical processes. These are the two areas in which the current study is focused.

6.2 Gun Muzzle Flash

Even though the current study is primarily to address the overpressure signature, the mechanisms which generate flash cannot be ignored since these are the chemical processes to which discrepancies in some earlier studies have been attributed. Here, a brief review of the primary computational efforts performed in the past to address flash is given. An extensive review of the experimental efforts into the problem of muzzle flash is provided by Klingenberg and Heimerl (1992).

The first model developed in an attempt to predict flash is the model described by Carfagno (1961) which he attributes to Dr. G.P. Wachtell (Klingenberg and Heimerl, 1992). This model, with the modification by May and Einstein (1980) uses a simplified flow scenario to predict the mixing of the gun gas and air and the resulting temperature. If the resulting temperature exceeds an experimentally determined critical ignition temperature, then flash is predicted to occur. However, this model has become recognized to not be a predictive tool.

The model of Yousefian (1982) for flash treats the flow field development at one instance in time and uses different models for the various regimes. The regions are first the interior ballistics region, followed by the expansion region, and finally the turbulent mixing region downstream of the shock disk which is known to form. The model uses different analysis tools for each region and various solution matching techniques have to be employed at the interfaces. The chemical reactions are simulated in the turbulent mixing region using one of the many plume prediction models. The final temperature calculated by this

three-segment model is used to determine if muzzle flash occurs. Fairly good correlations between predictions and experiments are reported for some gun systems (Klingenberg and Heimerl, 1992). However, the modeling process is not ideal for a design code to address a wide variety of gun systems and the steady-state assumptions and neglect of the blast wave raise concerns.

To simulate all the intricacies of flash requires first a finite rate chemistry model, such as the one developed here. Also, the dominant role of turbulence in the mixing of the gun gas and ambient air must be accounted for. Even with those aspects included, a detailed model of the chemical composition of the gun gas and the mechanism of the reaction between this gas and the air is needed. This in itself can be computationally intensive given the hydrocarbon makeup of the gun gas. Since the focus of the current study is to ascertain the impact of viscous effects and chemical reactions on the muzzle blast, the key aspect which must be captured by the current model of the chemical reaction process is the energy release. This is key since this energy release occurs behind the main blast wave and can work to sustain the blast to regions further out from the gun system. The reduced kinetic model to be used is described later. Even though a reduced kinetics scheme is to be used to better quantify the effects of reactions on the overpressures, the current model presents a viable tool for predicting muzzle flash given the finite rate chemistry model in place and the inclusion of the viscous effects.

6.3 Summary

The problem of gun muzzle blast and flash is driven by many of the same phenomenological aspects already addressed in the shock-induced combustion study. Also, the same numerical issues are present. Here, comparison of phenomenological models is not carried out as in the case of the shock-induced combustion computations. The goal of this facet of the current study is to first determine how the inclusion of the viscous and reaction aspects of the problem impact the computed overpressure field. If promising, alternate reaction mechanisms as well as other physical models can be addressed. Since there is a

desire to construct an engineering tool for muzzle device design, the computational efficiency requires the utmost attention. The particular models used as well as the results are discussed in the next chapter.

CHAPTER 7
GUN MUZZLE BLAST RESULTS AND DISCUSSION

As mentioned in the earlier description of the gun muzzle blast problem, the reduction of overpressures is desired in both large and small caliber gun systems for somewhat different reasons. With this in mind, the code developed here is evaluated for both a large caliber howitzer system as well as smaller firearms. The particular aspects of each computation are given and the simulated overpressures are compared to experimental data to ascertain the accuracy of the model and to discern the role of the the various physical and chemical processes.

7.1 Large Caliber Howitzer Simulations

The first gun system simulated is a 105mm howitzer which has been fired with a muzzle device. The device is essentially an extension mounted on the end of the muzzle as depicted in the drawing of Figure 7.1. The first issue in the simulation is the representation of the gun gas and the boundary conditions needed to represent the interior ballistic phase. The methodology of the current code is to simulate only the launch and exterior ballistic phases and account for the interior ballistic process by imposing time dependent boundary conditions at a plane just upstream of the muzzle exit. This is done to eliminate the need to recompute this initial process for each computation. From a physical standpoint, this is doable given the fact that the flow in the muzzle is supersonic over the time the computation is to be carried out. From a practical standpoint, the design or evaluation of a muzzle device is typically for a single gun (i.e. caliber) and a specific round of ammunition. The ammunition is easily changed by altering the boundary conditions.
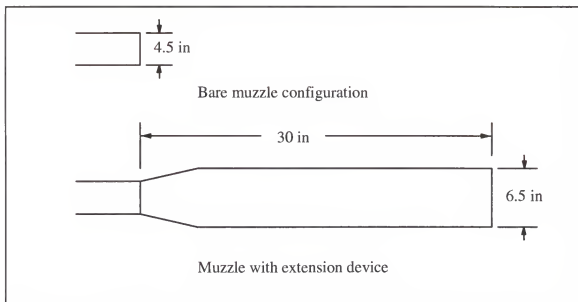
Figure 7.1.   Schematic of 105-mm howitzer and muzzle device used in current study.

7.1.1 Flow Field Model and Boundary Conditions

In the present effort the flow field is considered to be composed of four species, these being the O_2 and N_2 found in the ambient air, the gun propellant gas (F), and the product of reaction (P) between the O_2 and propellant gas. The number of species directly impacts the size of the set of equations to be solved. Therefore, since one goal of the current project is to develop a design code, a limited set of equations is desired. The properties for oxygen and nitrogen have been presented earlier. The ammunition being modeled here uses the M1 propellant described by Stiefel (1988) and the muzzle effluent is known to be composed primarily of the active agents CO and H_2 as well as the inert N_2 and the combustion products H_2O and CO_2. Therefore, the properties used for species F are formulated to represent a mixture of CO and H_2 and those for species P to represent a mixture of CO_2 and H_2O which is produced by any further reaction between the gun gas and the oxygen in the ambient air. The specified boundary conditions in the muzzle include appropriate values for the species mass fractions based on available interior ballistics data. The values of the molecular weight and heat of formation used in the current model are provided in Table 7.1

Table 7.1. Coefficients used in the gun blast computations to calculate specific heats for the various species and their molecular weights.

n	M_n	c_1	c_2	h_f^o
O_2	32.	3.636	4.33×10^{-4}	0.
F	22.13	4.74	4.0×10^{-4}	−32.42
P	24.51	4.025	1.18×10^{-3}	−93.73
N_2	28.013	3.5027	3.74×10^{-4}	0.

Cp_n in cal / (mole K) h_f^o in kcal / mole $T_R = 298$ K

Given the attention to computational efficiency in the context of a design code, here the specific heats of the various species are modeled with a linear dependence on temperature. As mentioned earlier in the description of the models, temperature must be extracted from the conserved quantities. If a linear representation of specific heat is used then a simple algebraic equation is solved in each computational cell. The use of a higher order representation requires the employment of an iterative scheme to extract temperature. The specific values used in the current computations for gun muzzle blast are provided in Table 7.1 with $Cp_i = c_1 + c_2 T$.

For the current study a simple one-step reaction of the form

$$F + O_2 \underset{k_b}{\overset{k_f}{\rightleftarrows}} P \tag{7.1}$$

with constants

$$A = 1 \times 10^{14} \text{ cm}^3/(\text{moles } {}^o K)$$
$$E_a/R_u = 21400 \, {}^o K \tag{7.2}$$

is used. This simplified reaction mechanism does not reproduce some of the physical occurrences represented by more detailed kinetics schemes, such as the induction delay, which is important to correctly simulate all the facets of muzzle flash. However, since the goal of the current study is to more accurately simulate the gun blast, any representation of

the energy release associated with further combustion behind the main blast wave is an improvement over the current state-of-the-art.

During the description of the gun blast and flash problem, issues which are impacted by turbulence such as the entrainment of air into the cloud of gun gas have been mentioned. The flow field, as pertaining to turbulence, can be thought of as being composed of two regions, the internal flow field bounded by the muzzle device, and the external field. The first region is dominated by the wall bounded nature of the flow where as the external field is more similar to a round jet type flow scenario. In the computations presented earlier for shock-induced combustion, a k-ε model has been used and such a model can be applied to both regions. Here, though, a more simplified representation for turbulence is used in this initial investigation into the role of viscous effects and chemical reactions in the occurrence of gun blast. The impact of turbulence on the internal regime is ignored for the present and the effects in the external field are represented using a mixing length model based on Prandtl's mixing length hypothesis discussed earlier (Hinze, 1959). The turbulent viscosity is represented using

$$\mu_t = \varrho l_{mix}^2 \left| \frac{du}{dy} \right| \tag{7.3}$$

where the mixing length is given by $l_{mix} = .075\delta$ based on the known mixing length for round jets (Launder and Spalding, 1972). The shear layer is calculated using

$$\delta = \frac{1}{|\omega|_{max}} \int_{-\infty}^{\infty} |\omega| \, dy \ , \ \omega = -\frac{\partial u}{\partial y} \tag{7.4}$$

based on the work of Papamoschou and Roshko (1988). For the large caliber gun computations, the turbulent Prandtl and Schmidt number are set to unity. One of the issues to be addressed is the adequacy of this reduced model. Regardless, the explicit representation of the dissipative mechanisms in the gun muzzle blast flow scenario is a marked improvement over previous investigations in which these processes are ignored or represented in an ad hoc fashion as mentioned earlier.

The current code simulates the launch and exterior phase of the gun propulsion problem. Therefore, boundary conditions representing the interior ballistics phase are imposed at the transition point which is defined here as a location just upstream of the exit of the bare muzzle. At this location, boundary conditions for the gas velocity, temperature, and pressure are imposed as well as the chemical composition. After studying data pertaining to large caliber gun systems, it has been determined that the appropriate boundary conditions to impose for the chemical composition are $\alpha_F = .64$ and $\alpha_{N_2} = .36$. Given the fact that the flow is being represented with as few species as necessary, the nitrogen boundary condition in the muzzle is used to mimic those inert by-products of the interior ballistics cycle.

The boundary conditions used for the remaining dependent variables have been determined from the lumped parameter interior ballistics code, XKTC, which is discussed by Horst, et al. (1990). The particular conditions used are shown in Figure 7.2 with each

Pmax = 3149 psi
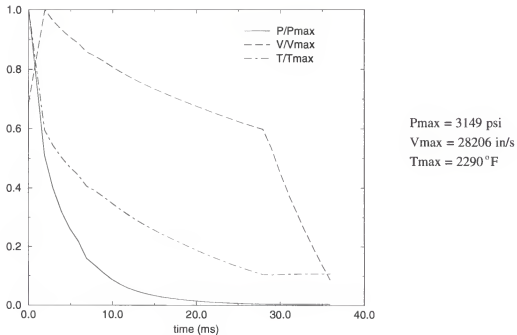Vmax = 28206 in/s
Tmax = 2290 °F

Figure 7.2.   Time dependent boundary conditions imposed at the exit of the muzzle.

quantity nondimensionalized by the maximum value. For lack of any detailed information on the profile of the variables at the transition point, a power law representation across the exit plane described by Kays and Crawford (1993) is used for the velocity and temperature distribution. Extrapolation boundary conditions are applied to the conserved variables (Q) along the boundaries of the computational domain and computations showed no artificial reflection of the pressure wave at these boundaries.

7.1.2 Experimental Overview

An experimental effort has been carried out in parallel to validate the present numerical code. During the initial tests, only the overpressures have been measured. However, this data can be used to compare to the pressures predicted by the numerical models and make judgements on what physical models better represent the actual flow field. The experimental setup consisted of a 105mm (M101) barrel mounted on a portable launcher depicted in Figure 7.3. This portable launcher is operated by the Ballistics Experimentation
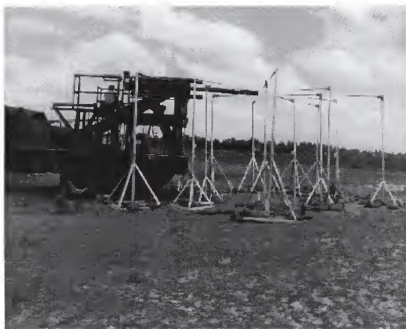

Figure 7.3. Portable launcher and experimental setup.

Facility (BEF) which is part of Wright Laboratory Armament Directorate, Eglin AFB, Florida. The launcher has the cannon mounted horizontally approximately 12 feet above the

ground. This minimizes any ground effect and possible corruption of the peak pressure pulse generated by the main blast wave. The rounds fired are 105mm M1A1 with inert projectiles. The rounds have been launched at velocities around 490 m/s.

Surrounding the muzzle are fifteen free air pressure probes which can be seen in the figure. A schematic in Figure 7.4 defines the coordinate system to be used in the next section and the positions of the eight probes closest to the gun are given. In addition to the free air probes, a pressure tap has been mounted on the barrel upstream of the muzzle device. This is used to validate the interior ballistic information. The muzzle device used during the test is the one currently used on the howitzer on-board the AC-130 Gunships which is essentially an extension tube 30" long with an inner diameter of 6.5" shown in Figure 7.1. One of the key observations during the experiments has been first the movement of the gage supports after the arrival of the main blast wave. Therefore, the confidence in pressure data other than the peak values is low. This is not that restrictive to the current study since comparison between computed and measured peak pressures is a key indicator as to the accuracy of the computational model. The second key observation has been the occurrence of intermediate flash. The importance of this is made clear later.

7.1.3 Computational Results

Computed peak pressures from eight locations in the field (Figure 7.4) are compared with the experimental measurements. The computational domain used in the simulations represents a physical region approximately 12 feet long and 6 feet wide using a grid size of 150 x 100 cells. Only half the field is computed given the axisymmetric nature of the problem. This resolution produces grid independent solutions which have been judged based on the calculated peak pressures for various grid refinements. The grid is clustered around the solid walls of the muzzle and extension. All computations have been carried out using the Strang splitting scheme discussed earlier.

The first issue in the computational study is to compare the results from the current model with known flow field features and results from earlier computational studies.

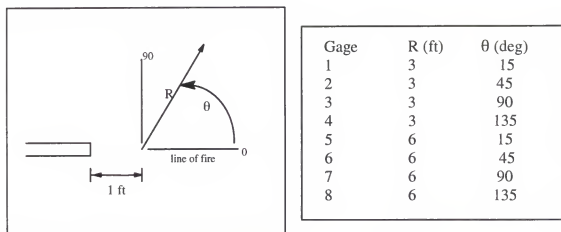| Gage	R (ft)	θ (deg)
1	3	15
2	3	45
3	3	90
4	3	135
5	6	15
6	6	45
7	6	90
8	6	135

Figure 7.4.   Schematic of flow field coordinate system along with the positions of the pressure gages.

Therefore, Figure 7.5 shows the density and pressure fields at a particular instant in time after the gun has fired. These computations have been carried out using the second-order upwind scheme discussed earlier and with the viscous and chemical processes neglected. Note, the current computations do not include a model of the projectile and the impact this has on the computed quantities is addressed later. The salient features known to be present in experimental measurements and which have been reproduced by earlier computations (Carofano, 1992) are evident. The first is the expansion region (er) which forms between the exit of the muzzle extension and the shock disk (sd) which is a second key feature. Also evident is the barrel shock (bs) which bounds the expansion region and intersects the shock disk at the triple point (tp). The contact surface (cs) which forms behind the main blast wave is evident in the density contour but not in the pressure field as should be. The plume boundary (pb) of the gun gas is also seen in the density field and at approximately halfway between the exit and the shock disk, this boundary thickens (th). This is observed in shadowgraphs from experiments and earlier computations (Carofano, 1992). The fact the current model reproduces these various features heightens the confidence in its ability to
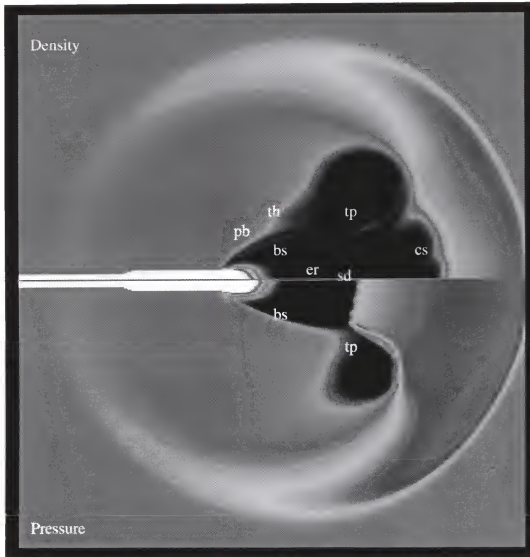
Figure 7.5. Density (upper half) and pressure field (lower half) computed with inviscid, nonreacting model.

simulate the gun muzzle blast problem. Also, given the fact that these inviscid, nonreacting results capture key flow field features the impact of the addition of viscous effects and chemical reactions must be quantified. This is addressed next.

A comparison between the peak pressures from simulations using solution schemes of first and second-order accuracy in the inviscid, non-reacting model can been seen in Figure 7.6. It should be noted that high temperature gas effects, such as variable specific heat, are included in the inviscid, non-reacting computations. The added numerical dissipation in
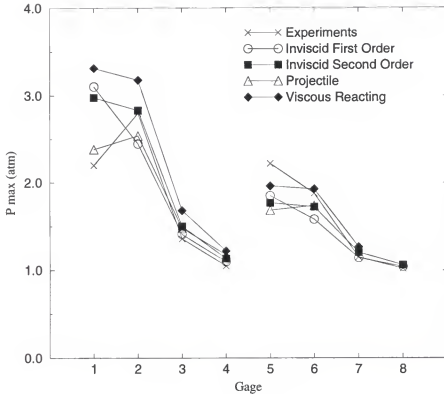
Figure 7.6. Comparison of peak pressures from the experiments and the simulations using the various models.

the first order scheme does cause a reduction in the peak pressures in some regions particularly along $\theta=45°$. This is of interest given the fact that in this region key physical phenomena such as the plume boundary lie. Also, as is evident in Figure 7.7 the order of accuracy impacts the predicted pressure time history. This is key for applications where not only are the peak overpressures of importance but where the transient characteristics are needed from the simulations. The remainder of the computations which include the viscous effects and reactions use the second-order scheme. The overprediction in the pressure at gage 1 is due to neglecting the projectile. This is evident by comparing these values to computed overpressure, shown in Figure 7.6, for which a model of the projectile has been included. The particular model used for the projectile assumed the projectile body to be a right circular
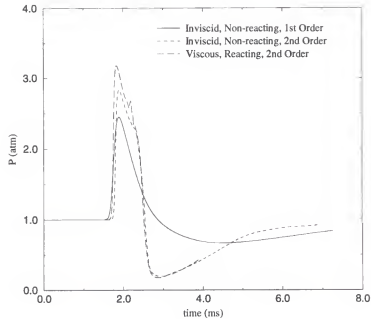
Figure 7.7.   Computed time histories from the various models showing the impact of both numerical and physical models on the simulated pressures.

cylinder and that during its fly-out through the computational domain, the velocity is constant. This is reasonable given available ballistic data and is similar to earlier models by Carofano (1990) and Buell and Widhopf (1984). The projectile is modeled by orientating a grid line to coincide to the radius of the cylindrical projectile. The face and base of the cylinder are tracked during the computation and boundary conditions for an impermeable surface are imposed at the appropriate locations. Also, in those cells containing the face and base of the projectile, an additional source term for volume change is imposed. The presence of the projectile disturbs the main blast wave in the region of the field near the line of fire ($R=3$ ft, $\theta \leq 45°$). This results in a somewhat lower peak overpressure. The computations which included the projectile have used the inviscid, nonreacting model.

The final curve of Figure 7.6 is the computed peak pressure using the model which includes viscous and reaction effects. The addition of the reactions produces an overprediction at those gage locations nearest the muzzle device exit while the values in the far field (R=6 ft, $\theta \leq 45°$) are more in line with the experiments. This implies there is some contribution to the blast signature from the further energy release associated with reactions between the gun gas and ambient air. The impact of chemical reactions can also be seen in the pressure time histories presented in Figure 7.7. Not only is the magnitude of the initial pressure pulse from the main blast wave increased over that of the non-reacting simulations, but also, a second peak is evident at the location of the reaction front. To determine the source of the overprediction in the near field but the improved computations at the locations further out, the other field quantities must be studied.

Figure 7.8 shows a comparison in the development of the flow field from the inviscid, non-reacting and the viscous, reacting computations by presenting temperature contours at discrete instances in time. The upper half of each contour is the inviscid, non-reacting solution while the lower half is the results from the viscous, reacting model. As seen in Figure 7.8, the additional heat release in the computations with the reaction model is evident by the increase in the temperatures over that computed with the inviscid, non-reacting model. It is important to note the reactions are initiated as soon as the gun gas exits the muzzle device.

As detailed in the description of gun muzzle flash presented earlier, typically when conventional guns are fired, any reaction between the gun gas and ambient air is first evident downstream of the shock disk which is the initiation source. In hopes of better representing the actual combustion process, in the current computations reactions between the gun gas and air are allowed to occur only in the exterior flow field and not in the interior of the muzzle device. However, as is evident in the contours of the reaction product mass fraction shown in Figure 7.9, the computations here show no delay after the gas exits the device before the reactions are initiated. There is also a considerable amount of reaction products evident in
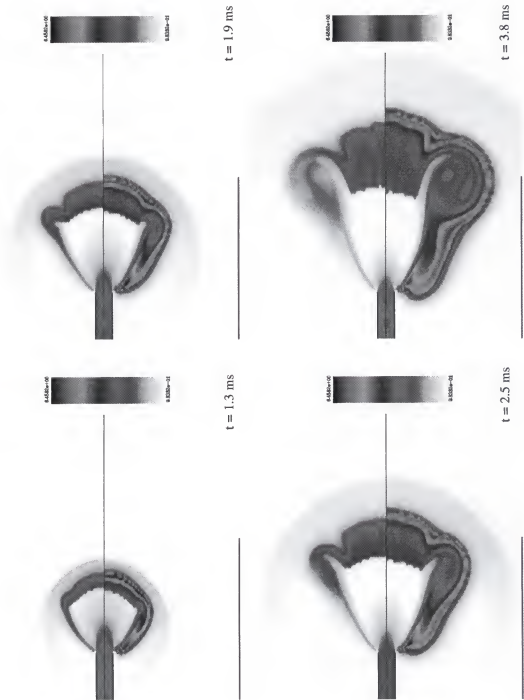
Figure 7.8. Comparison between the computed temperature field development from the inviscid, nonreacting (upper half of each contour) and viscous, reacting (lower half of each contour) models.
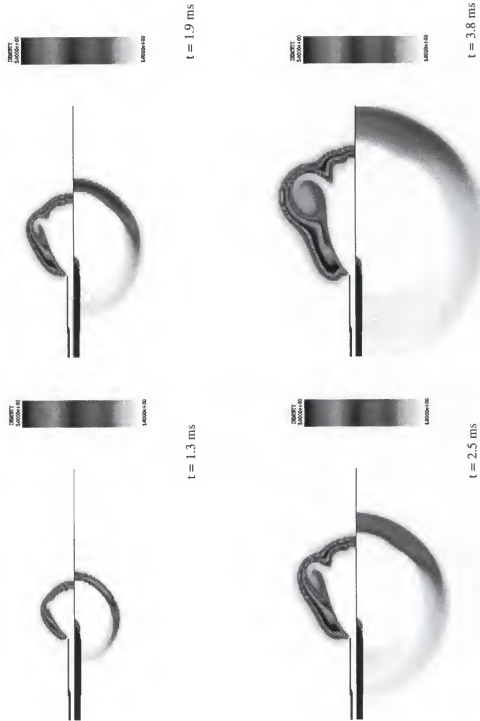
Figure 7.9.   Evolution of the reaction product mass fraction (upper half of each contour) and density (lower half of each contour) field from the viscous, reacting computations.

the lateral field. This under representation of the initiation process is a direct function of the simplified reaction mechanism used. Also included in Figure 7.9 are density contours which highlight the location of the main blast wave and show the reaction process is occurring behind the blast front where the interface of the gun gas and ambient air is located. The contour scale denotes the variation in density in the exterior field and the product mass fractions range from 0. to 0.15.

Though the one-step mechanism used here represents the combustion effects globally, this simplified model does not reproduce the correct evolution of the chemical reaction processes throughout the flow field. This is the most probable source of the overpredictions for the locations along the 3 ft arc and the improvement for those locations along the 6 ft arc. This supposition is supported by reviewing the role and the computed location of the shock disk. The shock disk forms at some distance from the muzzle, or in this case the muzzle device, and is essentially stationary until later in the blast process when the back pressure in the muzzle begins to drop off. Due to the nature of the chemical processes, intermediate flash is typically not initiated until some time after the disk becomes stationary. In the current computations, the shock disk forms at approximately 4 feet from the exit of the muzzle device. This is right in line with the gages along the 3 ft arc. Therefore, it is reasonable to expect the computed pressures to be higher than those measured given the fact the model is producing an additional energy source before it actually occurs. However, since the measurements made at the 6 ft point are outside the location where the combustion process does occur, any estimation for the addition of energy behind the main blast wave before it reaches this point would improve the computed values. It is also noticeable in the computed overpressures using the viscous, reacting model, there exists an overprediction for all gages along the 3 and 6 ft arc for $\theta \geq 90°$. This is not surprising when the reaction product mass fractions depicted in Figure 7.9 are considered. They show the one-step model is producing reactions in the lateral field upstream of the shock disk which is known to not be true in typical gun muzzle blast flows with intermediate flash.

Figure 7.10 shows the evolution of the pressure field computed with both models. The general characteristics of the pressure contour are the same for both sets of computations with the differences being in the magnitudes. Note the contour scales have been changed for each time interval to highlight the range of pressures in the exterior flow field. The most noticeable effect of the computations which include the reaction processes is that the pressure in the region behind the main blast wave is higher than the computations which neglect the reactions. This aspect is the key factor which improves the simulated peak overpressures in the farfield since the higher pressure works to sustain the main blast wave as it progresses through the field. Hence, even though the qualitative features of the pressure field predicted by the inviscid, non-reacting and the viscous, reacting models are comparable, the substantial differences in thermal characteristics depicted in Figure 7.8 cause significant quantitative differences.

The final facet assessed is the simplified model for turbulence. This is done by evaluating the magnitude of turbulent viscosity which is found, in the exterior field, to range from 1 to 20 times that of the molecular viscosity. This is considerably less than values seen in other high-speed, compressible flows using more sophisticated models. Comparisons between computed pressures using simply the laminar viscous terms and the mixing length model are indistinguishable. Given this finding as well as those pertaining to the chemical reaction model, a more sophisticated option is needed for both. However, given the framework of the code and the two-equation turbulence model used in the shock-induced combustion computations, both these improvements have no conceptual difficulties.

7.2 Small Caliber Sound Suppressor Simulations

In addition to the large scale howitzer case, the present code has also been used to study the effects of small caliber sound suppressors. The suppressor studied is a cylindrical cylinder with two internal baffles as illustrated in Figure 6.1. The simulations for the small caliber case have been carried out using only the inviscid and high temperature gas effects aspects of the code along with a constant velocity projectile assumption. This has been done
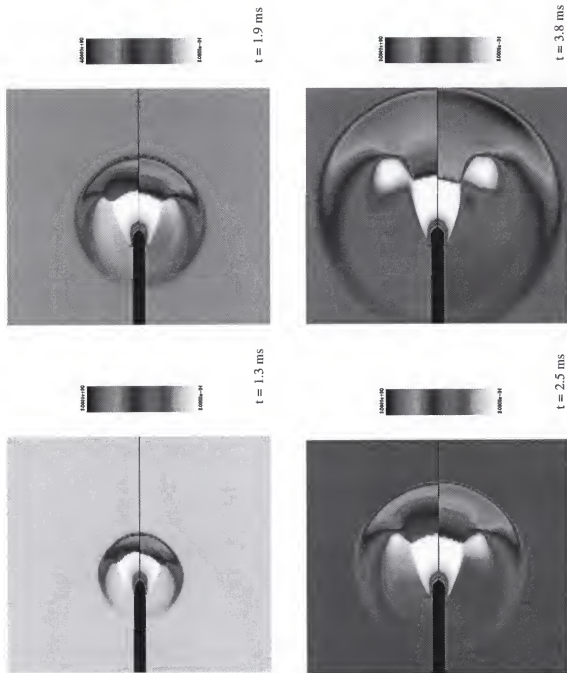
Figure 7.10. Development of the computed pressure filed from the inviscid, nonreacting (upper half of each contour) and viscous, reacting (lower half of each contour) models.

in part due to the fact the accompanied experiments (Hudson et al., 1996) have been carried out in parallel so limited information had been available as to the particulars of the ammunition or any observations on whether flash did occur. Therefore, given the nature of the one-step mechanism already discussed, it has been decided to use the baseline model, i.e. inviscid with no reactions. The goal of this portion of the current effort has been to determine the utility of the computational code developed here in designing sound suppressors for small caliber guns. No prior computational study into this caliber class has been found in the available literature.

This study into small caliber sound suppressors has used both a 38 / 9 mm competition handgun and a 22 rifle. Details of the experiments are available in the work of Hudson et al. (1996). The specifics of the propellant are not readily available so the properties used in the large caliber simulates are used here. Given the parallel experimental and computational effort, some assumptions have been made as to the boundary conditions based on data on similar size gun systems. The particular boundary conditions used for the simulations of the 38 / 9 mm are a peak pressure of 6,000 psi, peak velocity of 1000 fps, and a peak temperature of 2400 °F. It is assumed that all quantities decayed to atmospheric conditions over a time period of approximately 4 ms. For the 22, the peak pressure is lowered to 2,000 psi but the remaining variables were kept the same.

The only quantitative experimental data available for code evaluation is the peak pressures measured in the experiments. These measurements have been made at the locations denoted in Table 7.2 using a microphone. The distances are measured from the exit of the muzzle in the cases with no suppressor and from the exit of the suppressor when it is used. Qualitative observations made in the experiments include the following. The firings of the unsuppressed firearms show a single high-intensity peak in pressure. When the cylindrical suppressor is used, the magnitude in peak pressure is reduced but there also appears a series of smaller peaks in the signal. The utility of the computational code in assessing small caliber sound suppressor must be judged on both the quantitative and

Table 7.2. Placement of pressure gages for the experiments and simulations. X denotes distance from the exit of the muzzle (or suppressor) and Y the distance from the line of

Caliber	Gage	X (in)	Y (in)
22	1	0	7.5
22	2	3.5	7.5
22	3	7	7.5
22	4	0	10
22	5	5	10
22	6	10	10
38	1	0	10
38	2	5	10
38	3	10	10

qualitative data. Using this a decision can be made as to whether the code correctly simulates the general effect of the suppressors in reducing the pressure levels and in turn the acoustic signal. This data can also be used in determining to what extent the inviscid and real gas effects being modeled determine the peak pressures and the acoustic signals.

A comparison between the simulated and measured pressures for the bare muzzle 38 / 9 mm is presented in Figure 7.11 as well as data for the 38 / 9 mm with the suppressor. The computation is found to do a fairly good job in predicting the reduction in peak pressures. The peak pressures from the simulation for the 22 caliber case are presented in Figure 7.12. The first observation is that even though the simulation captures the trend in overpressures for the bare muzzle case, the values are lower than those measured at all gage locations. This indicates either the pressure assumed for the boundary conditions in the simulation is somewhat lower than those achieved during the experiments or the inviscid non-reacting flow model is not capturing some of the driving physics. It has been shown in the large caliber computations presented earlier that the chemical reaction processes can generate higher overpressures. However, before adding reaction for the small caliber cases presented here, a closer assessment of the true boundary conditions should be made. It is of importance to note no muzzle flash has been reported in the experiments which suggest the discrepancy is not due to the absence of reactions.
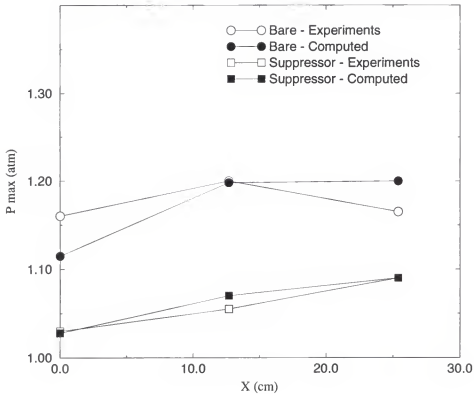
Figure 7.11. Comparison of peak pressures from the experiments and the simulations for the 38 / 9 mm gun.

The simulations of the 22 with suppressor do capture the general trend of the baffle design producing lower pressures and in turn lower sound levels. However, the simulated peak pressure values are somewhat larger than the measurements for gages 3 and 6. It is believed that some of the discrepancy is due to the assumed projectile velocity but further investigation is needed. If the time evolution of the suppressor's internal flow field is viewed, it is evident that shocks are continuously reflecting off the face of the suppressor walls normal to the line of fire. Given the fact that this interaction is highly non-linear, any errors in the boundary conditions can result in discrepancies in the exterior field and the trends of these discrepancy are difficult to predict. This periodic motion within the baffled suppressor is also most likely the driving force behind the pulsating pressure signature observed in the
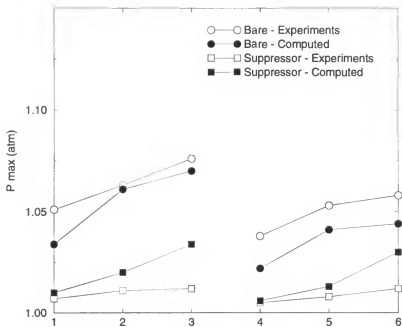
Figure 7.12. Comparison of peak pressures from the experiments and the simulations for the 22 rifle.

experimental results. This phenomena is also observed in the simulations and can be seen in Figure 7.13 which shows a pressure time history at gage location 2 for the 22 simulation. It also hints to the reason why there is an optimum length for the baffle chambers which has been mentioned in the earlier literature review of studies into gun muzzle blast. Even given these regions of over prediction, the simulation does capture the effects of the baffle design in reducing the pressure levels and in turn the sound generated. These results suggest the current code offers a viable tool for small caliber sound suppressors design.

7.3 Summary

The computational code developed here has been used to simulate both large and small caliber gun systems. Here some simplification in the area of the chemical kinetics and
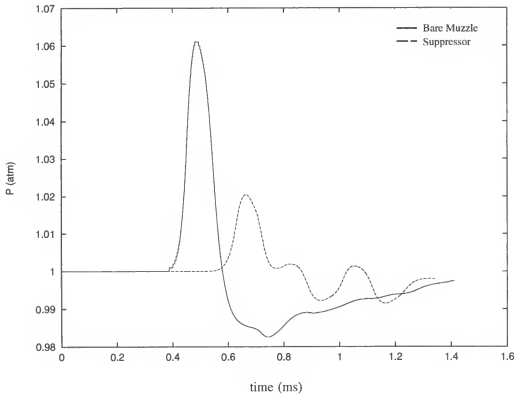
Figure 7.13. Simulated pressure time history at gage location 2 for the 22 with and without suppressor.

turbulence beyond those used in the shock-induced combustion computations have been employed. The computational times required to perform these simulations have all been on the order of hours using a desktop workstation. This suggest the code is a viable design tool. Based on the computations of the 105 mm howitzer, to better resolve the blast signature near the muzzle, a different reaction mechanisms is needed. This is also true if a concerted effort is to be made in simulating flash.

The computations of the small caliber gun systems have demonstrated this same code can be used to evaluate the acoustic signature of various sound suppressors. The distinct signal generated by the baffle suppressor is reproduced by the inviscid, nonreacting model which suggests this aspect is driven in a large part by the shock dynamics internal to the

suppressor. However, it should be noted that in the case of the small caliber systems, no flash has been reported, unlike in the case of the howitzer. This implies a reaction model may not be needed for some small caliber systems.

CHAPTER 8
CONCLUSIONS AND FUTURE WORK

This current effort has investigated two munition problems, a shock-induced combustion scenario Lehr (1972) and the occurrence of gun muzzle blast. Both the aspects of modeling these problems have been studied and some of the salient phenomenological issues have been addressed. Based on the current effort, some conclusions and suggestions for future work can be made on solving high-speed flows with chemical processes as well as the particular scenarios simulated here. The general conclusions and suggestions pertaining to the solution of this class of problems are presented along with comments on the particular shock-induced combustion case studied here. This is followed with a summary of the gun muzzle blast work.

8.1 Shock-Induced Combustion

Studied in the context of the shock-induced combustion scenario is the impact of the small chemical time and length scales on the solution of high-speed reacting flows. It has been detailed that the time scales of chemical processes directly impact computational parameters such as the temporal integration step. The Strang splitting method employed here offers a viable numerical technique to reduce computational time. This scheme allows the solution to be advanced at scales determined by the fluid dynamics aspect. The chemical processes are coupled to the fluid dynamics in a second-order manner. However, the splitting of the operators allows special attention to be paid to the chemical processes which now only requires the solution of a set of point-implicit ordinary differential equations (ODEs). For the steady-state case computed here, this allows scaling to be applied in the early stages of the flow field evolution to ensure nonphysical solutions are not encountered.

For unsteady scenarios, an iterative technique can be used in the ODE solution process to integrate the ODEs over the temporal scale set by the fluid dynamic aspects. One method which warrants investigation is the application of constrained optimization techniques. This is due to the fact that in the solution of the ODE, the primary problem is the overshooting of the solution into nonphysical regions. The set of ODEs governing the production of species has well established constraints, i.e. $0 \leq \alpha_n \leq 1$ and $\sum_{n=1}^{NS} \alpha_n = 1$, which may be used to aid in the convergence to the solution of the ODEs. Another possible improvement is to investigate how to better represent the temporal variation of the dependent variables. Currently, a linearization process is used to derive the set of ODEs by expressing Q^{n+1} as a function of Q^n. The variation is known to be more logarithmic in nature and this linearization process is another facet which produces nonphysical solutions.

Another impact of the logarithmic variation of the species concentrations is seen in the characteristic length scales of the chemical process. It is clear that the numerical error introduced by representing a highly nonlinear source term in a piecewise manner can be substantial. In short, the error is introduced by calculating the source term in a given cell as a function of the cell averaged dependent variables instead of actually calculating the cell averaged source term. The discrepancy in these two quantities is small in the case of slowly varying dependent variables. However, in the case of highly nonlinear variations, as found in reacting flows, the differences are quite large.

The source term modification scheme using scaling factors has been reviewed extensively here and offers a viable solution without increasing the computational mesh or applying grid adaptation. The current estimation of the effective production rate which enters the scaling proves adequate when reduced kinetic models are used. Alternative estimates of the effective rate used in the scaling should be studied. Since this effective rate is dependent on the relationship between the individual mass fractions and the source term, characteristics of the source term Jacobian may prove useful in the estimation process. Also,

a technique may be obtainable if indeed the cell average of the nonlinear varying source term is calculated.

It is clear from the current study that the impact of the chemical time and length scales on the computation of high-speed reacting flows must be addressed with special numerical treatments. However, these treatments must be considered along with the phenomenology of the models. The splitting scheme and source term treatments used here prove advantageous and warrant further investigation for not only the current finite rate chemical reactions but also other physical and chemical processes. The impact of any such treatments on the reproduction of the phenomenological aspects must be well understood. Many times it is not required to reproduce all the physical and chemical aspects which typically generate the computational restrictions. For example, in the current computations, the induction zone is not explicitly resolved along the stagnation line but this does not hinder a satisfactory computation of the overall flow field when the source term treatment is used. Also, the reduced kinetic schemes which do not consider some of the intermediate species produce good agreements with experimental data. If a more extensive mechanism is used, then the additional time scales associated with the production and destruction of these intermediate species are orders of magnitude smaller and are the scales which can limit the integration time step. It is shown here that such intermediate processes can be ignored if a satisfactory job is done in reproducing key characteristics such as induction times and heat release rates.

Another facet of solving this class of problems which has been investigated is the role of the reaction mechanism on solution accuracy. Mechanism characteristics such as the induction times and heat release rates they produce are found to impact the computation of key flow field features. Also, the second explosion limit produced by the 32-step mechanisms is found to impact the chemical time scales and in-turn the computed flow field. The current study has identified key characteristics that any mechanism must reproduce. For example, the ratio between induction time as a function and resident time as a function of the conditions behind the shock, directly determine the positioning of the reaction front seen

in the experimental images. However, the results presented here also suggest further investigation is needed into the applicability of these mechanisms in the high-pressure regime.

Many times trade-offs must be made to balance the complexity of the physical or chemical model against computational requirements of the model. Here we have seen the use of a two-equation turbulence model which offers an improved representation of the turbulent aspects of the problem with minimal increase in computational requirements. This model has been used to both represent the enhanced dissipation of species and heat as well as estimate the magnitude of the temperature fluctuations. Also, a model for the role of these fluctuations on the chemical reaction source term has been implemented. The impact of the turbulence has been found to be minimal for the current steady shock-induced combustion scenario. This is most likely not true for other flow scenarios such a flame holder situation or for the unsteady shock-induced combustion regime. Therefore, the current model should be further tested on other flow scenarios. More detailed models for the coupling of the turbulence and scalar fields should be assessed. The assumption of turbulence Prandtl and Schmidt numbers dictate that only one time scale, associated with the momentum field, is important. Models which explicitly represent the scales of the scalar field may prove advantageous. This requires the solution of additional equations so both accuracy and computational aspects of such models should be investigated.

8.2 Gun Muzzle Blast

Both large and small caliber gun systems have been simulated using the computational models developed here. In the case of the 105 mm howitzer simulations, the role of combustion between the gun gas and air is found to be key in establishing the overpressure field. The reduced kinetic scheme developed and tested offers a viable option to more detailed mechanisms for use in a design code. It is evident the kinetic scheme needs to be altered to better reproduce induction delay times. This is manageable in the context of the reduced mechanism. It is also clear the algebraic model tested for turbulence is

inadequate and a model more akin to the two-equation model used in the shock-induced combustion flow is needed.

The small caliber firearm computations have shown the current code can capture the reduction in magnitude of the acoustic signal generated by a muffler. It is also evident that the acoustic signal of the muffler, the periodic wave pattern, is driven to a large extent by the fluid dynamic aspects of the flow internal to the muffler. Further testing is warranted to quantify the role of chemical reactions and viscous effects in the small caliber firearm scenario. However, a more complete survey of both boundary conditions and propellant composition is needed.

8.3 Summary

The current study has addressed both the phenomenological and numerical aspects of computing high-speed reacting flows. This investigation has been carried out in the context of solving full-scale engineering problems to ensure both accuracy and efficiency are considered paramount. It is clear that when solving such problems, the physical, chemical, and numerical facets must all be considering in concert. The computational code developed here offers both a framework into which future models can be integrated for the various phenomenological processes and a viable engineering analysis tool.

APPENDIX
JACOBIANS AND EIGENVECTORS

Here the eigenvectors of the inviscid flux Jacobians are presented. These vectors are needed for the flux vector splitting scheme discussed earlier. Many of the terms in the Jacobians are the derivative of pressure with respect to the dependent variables. These are provided for the equation-of-state used in the current computations. However, the code developed here is structured such that these derivatives are calculated in a specific routine which can be changed to accommodate a different state equation without altering the routines which calculate the flux Jacobians.

$$
T_k^{-1} = \begin{bmatrix}
1 - \dfrac{P_1}{c^2} & -\dfrac{P_2}{c^2} & -\dfrac{P_3}{c^2} \\[2ex]
\tilde{k}_y u - \tilde{k}_x v & -\tilde{k}_y & \tilde{k}_x \\[2ex]
\frac{1}{2}\left(\dfrac{P_1}{c} - \theta_k\right) & \frac{1}{2}\left(\tilde{k}_x + \dfrac{P_2}{c}\right) & \frac{1}{2}\left(\tilde{k}_y + \dfrac{P_3}{c}\right) \\[2ex]
-\frac{1}{2}\left(\dfrac{P_1}{c} + \theta_k\right) & \frac{1}{2}\left(\tilde{k}_x - \dfrac{P_2}{c}\right) & \frac{1}{2}\left(\tilde{k}_y - \dfrac{P_3}{c}\right) \\[2ex]
-\alpha_1 & 0 & 0 \\
-\alpha_2 & 0 & 0 \\
\vdots & \vdots & \vdots \\
-\alpha_{NS-1} & 0 & 0
\end{bmatrix}
$$

$$
\begin{bmatrix}
-\dfrac{P_4}{c^2} & -\dfrac{P_{c_1}}{c^2} & -\dfrac{P_{c_2}}{c^2} & & -\dfrac{P_{c_{NS-1}}}{c^2} \\
0 & 0 & 0 & & 0 \\
\dfrac{P_4}{2c} & \dfrac{P_{c_1}}{2c} & \dfrac{P_{c_2}}{2c} & & \dfrac{P_{c_{NS-1}}}{2c} \\
-\dfrac{P_4}{2c} & -\dfrac{P_{c_1}}{2c} & -\dfrac{P_{c_2}}{2c} & \cdots & -\dfrac{P_{c_{NS-1}}}{2c} \\
0 & 1 & 0 & & 0 \\
0 & 0 & 1 & & 0 \\
\vdots & \vdots & \vdots & & \vdots \\
0 & 0 & 0 & & 1
\end{bmatrix} \tag{A.1}
$$

$$
T_k =
\begin{bmatrix}
1 & 0 & \dfrac{1}{c} & -\dfrac{1}{c} \\
u & -\tilde{k}_y & \tilde{k}_x + \dfrac{u}{c} & \tilde{k}_x - \dfrac{u}{c} \\
v & \tilde{k}_x & \tilde{k}_y + \dfrac{v}{c} & \tilde{k}_y - \dfrac{v}{c} \\
H - \dfrac{c^2}{P_4} & \left(\tilde{k}_y P_2 - \tilde{k}_x P_3\right)\dfrac{1}{P_4} & \theta_k + \dfrac{H}{c} & \theta_k - \dfrac{H}{c} \\
\alpha_1 & 0 & \dfrac{\alpha_1}{c} & -\dfrac{\alpha_1}{c} \\
\alpha_2 & 0 & \dfrac{\alpha_2}{c} & -\dfrac{\alpha_2}{c} \\
\vdots & \vdots & \vdots & \vdots \\
\alpha_{NS-1} & 0 & \dfrac{\alpha_{NS-1}}{c} & -\dfrac{\alpha_{NS-1}}{c}
\end{bmatrix}
$$

$$
\begin{bmatrix}
0 & 0 & 0 \\
0 & 0 & 0 \\
0 & 0 & 0 \\
-\dfrac{P_{c_1}}{P_4} & -\dfrac{P_{c_2}}{P_4} & \cdots & -\dfrac{P_{c_{NS-1}}}{P_4} \\
1 & 0 & 0 \\
0 & 1 & 0 \\
\vdots & \vdots & \vdots \\
0 & 0 & 1
\end{bmatrix} \tag{A.2}
$$

where

$$
\theta_k = \tilde{k}_x u + \tilde{k}_y v
$$
$$
\tilde{k}_x = \frac{k_x}{|\nabla k|} \ , \ \ \tilde{k}_y = \frac{k_y}{|\nabla k|} \ , \ \ |\nabla k| = \sqrt{k_x^2 + k_y^2} \ . \tag{A.3}
$$

The above formulation gives the eigenvectors for A_1 when $k=\xi$ and B_1 when $k=\eta$. Note,

$$\xi_x = \frac{y_\eta}{J} \quad , \quad \xi_y = \frac{-x_\eta}{J}$$

$$\eta_x = \frac{-y_\xi}{J} \quad , \quad \eta_y = \frac{x_\xi}{J} \quad . \tag{A.4}$$

The derivatives of pressure, for the current equation-of-state, are

$$P_1 = P_\varrho + \frac{P_e}{\varrho}\left(-E + u^2 + v^2\right)$$

$$P_2 = -\frac{uP_e}{\varrho}$$

$$P_3 = -\frac{vP_e}{\varrho} \tag{A.5}$$

$$P_4 = \frac{P_e}{\varrho}$$

$$P_{c_i} = P_{\varrho\alpha_i} = R_uT\left(\frac{1}{M_i} - \frac{1}{M_{NS}}\right) - \frac{R_u}{Mc_v}\left(e_i - e_{NS}\right)$$

with

$$P_\varrho = \frac{R_uT}{M_{NS}} + \frac{R_u}{Mc_v}\sum_{i=1}^{NS-1}\alpha_i\left(e_i - e_{NS}\right)$$

$$P_e = \frac{\varrho R_uT}{Mc_v} \tag{A.6}$$

where R_u is the universal gas constant. The frozen speed of sound is calculated using

$$c^2 = P_\varrho + \frac{P_e P}{\varrho^2} + \sum_{i=1}^{NS-1}\alpha_i P_{c_i} \tag{A.7}$$

The Jacobian of the source term vector is

$$\frac{\partial\Omega}{\partial Q} = \begin{bmatrix} 0 & 0 & 0 & 0 & 0 & 0 \\ 0 & 0 & 0 & 0 & 0 & 0 \\ 0 & 0 & 0 & 0 & 0 & 0 \\ 0 & 0 & 0 & 0 & 0 & 0 \\ 0 & 0 & 0 & 0 & 0 & 0 \\ \frac{\partial\dot\omega_1}{\partial\varrho} & \frac{\partial\dot\omega_1}{\partial\varrho u} & \frac{\partial\dot\omega_1}{\partial\varrho v} & \frac{\partial\dot\omega_1}{\partial\varrho E} & \frac{\partial\dot\omega_1}{\partial\varrho\alpha_1} & \cdots & \frac{\partial\dot\omega_1}{\partial\varrho\alpha_{NS-1}} \\ \frac{\partial\dot\omega_2}{\partial\varrho} & \frac{\partial\dot\omega_2}{\partial\varrho u} & \frac{\partial\dot\omega_2}{\partial\varrho v} & \frac{\partial\dot\omega_2}{\partial\varrho E} & \frac{\partial\dot\omega_2}{\partial\varrho\alpha_1} & \frac{\partial\dot\omega_2}{\partial\varrho\alpha_{NS-1}} \\ \vdots & \vdots & \vdots & \vdots & \vdots & \vdots \\ \frac{\partial\dot\omega_{NS-1}}{\partial\varrho} & \frac{\partial\dot\omega_{NS-1}}{\partial\varrho u} & \frac{\partial\dot\omega_{NS-1}}{\partial\varrho v} & \frac{\partial\dot\omega_{NS-1}}{\partial\varrho E} & \frac{\partial\dot\omega_{NS-1}}{\partial\varrho\alpha_1} & \frac{\partial\dot\omega_{NS-1}}{\partial\varrho\alpha_{NS-1}} \end{bmatrix} \tag{A.8}$$

where the components of the matrix are

$$\frac{\partial \dot{\omega}_i}{\partial \varrho} = \frac{(u^2 + v^2 - E)}{\varrho c_v} \frac{\partial \dot{\omega}_i}{\partial T}$$

$$\frac{\partial \dot{\omega}_i}{\partial \varrho u} = -\frac{u}{\varrho c_v} \frac{\partial \dot{\omega}_i}{\partial T}$$

$$\frac{\partial \dot{\omega}_i}{\partial \varrho v} = -\frac{v}{\varrho c_v} \frac{\partial \dot{\omega}_i}{\partial T}$$

$$\frac{\partial \dot{\omega}_i}{\partial \varrho E} = \frac{1}{\varrho c_v} \frac{\partial \dot{\omega}_i}{\partial T} \tag{A.9}$$

$$\frac{\partial \dot{\omega}_i}{\partial \varrho \alpha_j} = M_i \sum_{n=1}^{NR} \left(v''_{nj} - v'_{nj} \right) \times \left[\frac{v'_{nj}}{\varrho \alpha_j} k_{f_n} \prod_{l=1}^{NS} X_l^{v'_{nl}} - \frac{v''_{nj}}{\varrho \alpha_j} k_{b_n} \prod_{l=1}^{NS} X_l^{v''_{nl}} \right]$$
$$- \frac{\left(e_j - e_{NS} \right)}{\varrho c_v} \frac{\partial \dot{\omega}_i}{\partial T}$$

with

$$\frac{\partial \dot{\omega}_i}{\partial T} = M_i \sum_{n=1}^{NR} \left(v''_{nj} - v'_{nj} \right) \times \left[\frac{k_{f_n}}{T} \left(b_{f_n} + \frac{E_n}{R_u T} \right) \prod_{l=1}^{NS} X_l^{v'_{nl}} \right.$$
$$\left. - \frac{k_{b_n}}{T} \left(b_{b_n} + \frac{E_n}{R_u T} \right) \prod_{l=1}^{NS} X_l^{v''_{nl}} \right]. \tag{A.10}$$

The coefficients b_{f_n} and b_{b_n} are the corresponding pre-exponential powers of T in the Arrhenius rate term and the internal energy associated with an individual species, e_i, is

$$e_i = h_i - \frac{R_u T}{M_i} \ . \tag{A.11}$$

REFERENCES

Ahuja, J.K. and Tiwari, S.N., 1993, "Numerical Simulation of Shock-Induced Combustion in a Superdetonative Hydrogen-Air System," AIAA Paper 93-0242.

Alpert, R.A. and Toong, T.Y., 1972, "Periodicity in Exothermic-Hypersonic Flows about Blunt Projectiles," *Astronautica Acta*, Vol. 17, pp. 539–560.

Anderson, J., 1989, *Hypersonic and High Temperature Gas Dynamics*, McGraw-Hill, New York.

Bermudez, A. and Vazquez, M., 1994, "Upwind Methods for Hyperbolic Conservation Laws With Source Terms," *Computers and Fluids*, Vol. 23, pp. 1049–1071.

Buell, J.C. and Widhopf, G.F., 1984, "Three-Dimensional Simulation of Muzzle Brake Flowfields," AIAA Paper 84–1641.

Candler, G.V., 1988, *The Computation of Weakly Ionized Hypersonic Flows in Thermo-Chemical Nonequilibrium*, Ph. D Thesis, Stanford University.

Carofano, G.C., 1984, "Blast Computation Using Harten's Total Variation Diminishing Scheme," ARCCB–TR–84029.

Carofano, G.C., 1988, "The Blast Field Produced by a Cannon Having a Perforated Muzzle Brake," ARCCB–TR–88043.

Carofano, G.C., 1990, "A Comparison of Experimental and Numerical Blast Data For Perforated Muzzle Brakes," ARCCB–TR–90034.

Carofano, G.C., 1992, "A Note on the Blast Signature of a Cannon," ARCCB–TR–92014.

Carofano, G.C., 1993, "Blast Field Contouring Using Upstream Venting," ARCCB–TR–93009.

Carfagno, S.P., 1961, *Handbook on Gun Flash*, The Franklin Inst., Philadelphia, PA.

Chakravarthy, S.R. and S. Osher, S., 1985, "A New Class of High Accuracy TVD Schemes for Hyperbolic Conservation Laws," AIAA Paper 85–0363.

Chen, Y.S. and Kim, S. W., 1987, "Computation of Turbulent Flows Using an Extended k-ε Turbulence Closure Model," NASA CR–179204.

Chen, Y.S., Liaw, P. and Shang, H.M., 1993, "Numerical Analysis of Complex Internal and External Viscous Flows with a Second-Order Pressure-Based Method," AIAA Paper 93–2966.

Cinnella, P., 1989, *Flux-Split Algorithms for Flows With Non-Equilbrium Chemistry and Thermodynamics*, Ph.D. Dissertation, Virginia Polytechinic Institute and State University.

Correa, S.M. and Shyy, W., 1987, "Computational Models and Methods for Continuous Gaseous Turbulent Combustion," *Progress in Energy and Combustion Sceince*, Vol. 13, pp. 249–292.

Davies, C.B. and Venkatapathy, E., 1992, "The Multidimensional Self-Adaptive Grid Code, SAGE," NASA TM–103905.

Drummond, J.P., 1988, "A Two-Dimensional Numeric Simulation of a Supersonic, Chemically Reacting Mixing Layer," NASA TM–4055.

Drummond, J.P., 1990, "Supersonic Reacting Internal Flow Fields," NASA TM–103480.

Drummond, J.P., Rogers, R.C. and Hussaini, M.Y., 1986, "A Detailed Numerical Model of a Supersonic Reacting Mixing Layer," AIAA Paper 86–1427.

Erdos, J.I. and Del Guidice, P.D., 1975, "Calculation of Muzzle Blast Flowfields," *AIAA Journal*, Vol. 13, pp. 1048–1055.

Erlebacher, G., Hussaini, M.Y., Speziale, C.G. and Zang, T.A., 1992, "Toward the Large-eddy Simulation of Compressible Turbulent Flows," *Journal of Fluid Mechanics*, Vol. 238, pp. 155–185.

Evans, J.S. and Schexnayder, C.J., 1980, "Influence of Chemical Kinetics and Unmixedness on Burning in Supersonic Hydrogen Flames," *AIAA Journal*, Vol. 18, pp. 188–193.

Fansler, K.S. and Lyon, D.H., 1989, "Attenuation of Muzzle Blast Using Configurable Mufflers," BRL–TR–2979.

Fansler, K.S. and Schmidt, E.M., 1983, "The Prediction of Gun Muzzle Blast Properties Utilizing Scaling," ARBRL–TR–02504.

Fansler, K.S., Cooke, C. H., Thompson, W. G. and Lyon, D. H., 1990, "Numerical Simulation of a Multi–Compartmented Gun Muffler and Comparison with Experiments," BRL–TR–3145.

Galperin, B. and Orszag, S., 1993, *Large Eddy SImulation of Complex Engineering and Geophysical Flows*, Cambridge, New York.

Gardiner, W.C., Jr., and Troe, J., 1984, "Rate Coefficients of Thermal Dissociation, Isomerization, and Recombination Reactions," *Combustion Chemistry*, edited by W.C. Gardiner, Jr., Springer-Verlag, New York, pp. 173–196.

Gaviglio, J., Dussauge, J., Debieve, J. and Favre, A., 1977, "Behaviour of a turbulent flow, strongly out of equilibrium, at supersonic speeds," *Physics of Fluids*, Vol. 20, pp. 179–192.

Germano, M., 1992, "Turbulence : the Filtering Approach," *Journal of Fluid Mechanics*, Vol. 238, pp. 325–336.

Glaister, P., 1988, "An Approximate Linearised Riemann Solver for the Euler Equations for REal Gases," *Journal of Computational Physics*, Vol. 74, pp. 382–408.

Gore, R., Hanson, D. and Vaughn, L., 1993, "Coupling Hydrodynamics, Turbulence, and Chemistry to the Design of Reactive Munitions," Proceedings of 43rd Bomb and Warhead Technical Meeting.

Grossman, B. and Cinnella, P., 1990, "Flux-Split Algorithms for Flows with Non-equilibrium Chemistry and Vibrational Relaxation," *Journal of Computational Physics*, Vol. 88, pp. 131–167.

Hinze, J.O., 1959, *Turbulence*, McGraw Hill, New York.

Hirsch, C., 1990a, *Numerical Computation of Internal and External Flows, Vol 2., Computational Methods for Inviscid and Viscous Flows*, Wiley & Sons, New York.

Hirsch, C., 1990b, *Numerical Computation of Internal and External Flows, Vol 1., Computational Methods for Inviscid and Viscous Flows*, Wiley & Sons, New York.

Horst, A., Keller, G.E. and Gough, P., 1990, "New Directions in Multiphase Flow Interior Ballistic Modeling," BRL–TR–3102.

Hudson, M.K., Luchini, C., Clutter, J.K. and Shyy, W., 1996, "CFD Approach to Firearms Sound Suppressor Design," AIAA Paper 96–3020.

Jachimowski, C.J., 1988, "An Analytical Study of the Hydrogen-Air Reaction Mechanism with Application to Scramjet Combustion," NASA TP–2791.

Jameson, A. and Yoon, S., 1987, "Lower-Upper Implicit Schemes with Multiple Grids for the Euler Equations," *AIAA Journal*, Vol. 25, pp. 929–935.

Janus, J.M., 1989, *Advanced 3-D CFD Algorithm for Turbomachinery*, Ph.D Thesis, Mississippi State University.

Janus, J.M., Cox, C.F., Arabshahi, A., Cinella, P. and Whitfield, D.L., 1992, "Numerical Solution and Algorithm Analysis for the Unsteady Navier-Stokes Equations on Dynamic Multiblock Grids Including Chemical Equilibrium, Vol II," WL–TR–92–7044.

Jones, W.P. and Launder, B.E., 1973, "The Calculation of Low-Reynolds-Number Phenomena with a Two-Equation Model of Turbulence," *International Journal of Heat and Mass Transfer*, Vol. 16, pp. 1119–1130.

Kays, W.M. and Crawford, M.E., 1993, *Convective Heat and Mass Transfer*, McGraw-Hill, New York.

Klingenberg, G. and Heimerl, H.M., Editors, 1992, *Gun Muzzle Blast and Flash*, AIAA, Washington D.C.

Klingenberg, G., Mach, H. and Smeets, G., 1983, "Flow Field Measurements of an Unsteady Reacting Muzzle Exhaust Flow," *ASME Journal of Heat Transfer*, Vol. 105, pp. 884–888.

Krishnamurty, V.S., 1996, *Effect of Compressibility on the Turbulence Structure and its Modelling*, Ph. D. Dissertation, University of Florida.

Launder, B.E. and Spalding, D.B., 1972, *Mathematical Models of Turbulence*, Academic Press, New York.

Lee, S. and Deiwert, G.S., 1989, "Calculation of Nonequilibrium Hydrogen-Air Reactions With Implicit Flux Vector Splitting Method," AIAA Paper 89–1700.

Lehr, H.F., 1972, "Experiments on Shock-Induced Combustion," *Astronautica Acta*, Vol 17, No 4, pp. 589–597.

Lehr, H.F. and Maurer, R., 1969, "Untersuchungen über die Vorgänge beim Einschuss von Projektilen in reagierendes Gasgemisch," Instite Saint-Lous Report 6/69.

LeVeque, R.J. and Yee, H.C., 1990, "A Study of Numerical Methods for Hyperbolic Conservation Laws with Stiff Source Terms," *Journal of Computational Physics*, Vol. 86, pp. 187–210.

Lewis, B. and von Elbe, G., 1961, *Combustion, Flames and Explosions of Gases*, Academic Press, New York.

Libby, P.A. and Williams, F.A., 1994, *Turbulent Reacting Flows*, Academic Press, London.

Liou, M.S., Van Leer, B. and Shuen, J.S., 1990, "Splitting of Inviscid Flues for Real Gases," *Journal of Computational Physics*, Vol. 87, pp. 1–24.

MacCormack, R.W., 1985, "Current Status of Numerical Solutions of the Navier-Stokes Equations," AIAA Paper 85–0032.

Matsuo, A. and Fujii, K., 1995, "Computational Study of Large-Disturbance Oscillations in Unsteady Supersonic Combustion Around Projectiles," *AIAA Journal*, Vol. 33, pp. 1828–1835.

Matsuo, A. and Fujii, K., 1996a, "First Damköhler Parameter for Prediction and Classification of Unsteady Combustions around Hypersonic Projectiles," AIAA Paper 96–3137.

Matsuo, A. and Fujii, K., 1996b, "Detailed Mechanism of the Unsteady Combustion Around Hypersonic Projectiles," *AIAA Journal*, Vol. 34, pp. 2082–2089.

Matsuo, A., Fujii, K. and Fujiwara, T., 1993, "Flow Features of Shock-Induced Combustion Around Projectile Traveling at Hypervelocities," AIAA Paper 93–0451; see also 1995, *AIAA Journal*, Vol. 33, pp. 1056–1063.

Matsuo, A. and Fujiwara, T., 1993, "Numerical Investigation of Oscillatory Instability in Shock-Induced Combustion Around a Blunt Body," *AIAA Journal*, Vol. 31, pp. 1835–1841.

May, I.W. and Einstein, S.I., 1980, "Prediction of Gun Muzzle Flash," ARBRL–TR–02229.

Mizobuchi, Y., Matsuo, Y. and Ogawa, S., 1997, "Numerical Estimation of Turbulence Temperature Fluctuation Effect on Hydrogen-Oxygen Reaction Process," AIAA Paper 97–0910.

McKenna, J.T., 1996, "ValuJet Hearing Presages U.S. Safety Overhaul," *Aviation Week and Space Technology*, Vol. 145, pp. 37–40.

McVey, J.B. and Toong, T.Y., 1971, "Mechanism of Instabilities of Exothermic Hypersonic Blunt-Body Flows," *Combustion Science and Technology*, Vol. 3, pp. 63–76.

Milton, B. E. and Keck, J. C., 1984, "Laminar Burning Velocities in Stoichiometric Hydrogen and Hydrogen-Hydrocarbon Gas Mixtures," *Combustion and Flame*, Vol. 58, pp. 13–22.

Molvik, G.A. and Merkle, C.L., 1989, "A Set of Strongly Coupled, Upwind Algorithms for Computing Flows in Chemical Nonequilibrium," AIAA Paper 89–0199.

Montagne, J.L., Yee, H.C. and Vinokur, M., 1987, "Comparitive Study of High-Resolution Shock-Capturing Schemes for a Real Gas," NASA TM–100004.

Moretti, G., 1965, "A New Technique for the Numerical Analysis of Nonequilibrium Flows," *AIAA Journal*, Vol. 3., pp. 223–229.

Nagano, Y. and Shimada, M., 1996, "Development of a two-equation heat transfer model based on direct simulations of turbulent flows with different Prandtl numbers," *Physics of Fluids*, Vol. 8, pp. 3379–3402.

Oldenborg, R., Chinitz, W., Friedman, M., Jaffe, R., Jachimowski, C., Rabinowitz, M. and Shott, G., NASP Rate Constant Committee, 1988, "Hypersonic Combustion Kinetics; Status Report of the Rate Constant Committee, NASP High Speed Propulsion Technology Team," NASA TP–2791.

Oldenborg, R., Chinitz, W., Friedman, M., Jaffe, R., Jachimowski, C., Rabinowitz, M. and Shott, G., NASP Rate Constant Committee, 1990, "Hypersonic Combustion Kinetics; Status Report of the Rate Constant Committee, NASP High Speed Propulsion Technology Team," NASP TM–1107.

Papamoschou, D. and Roshko, A., 1988, "The Compressible Turbulent Shear Layer: An Experimental Study," *Journal of Fluid Mechanics*, Vol. 197, pp. 453–477.

Ramshaw, J.D. and Chang, C.H., 1995, "Iteration Scheme for Implicit Calculations of Kinetic and Equilibrium Chemical Reactions in Fluid Dynamics," *Journal of Computational Physics*, Vol. 116, pp. 359–364.

Rhie, C.M., Stowers, S.T. and Ebrahium, H.B., 1993, "Numerical Analysis of Reacting Flows Using Finite Rate Chemistry Models," *Journal of Propulsion and Power*, Vol. 9, pp. 119–126.

Rogers, R.C. and Chinitz, W., 1983, "Using a Global Hydrogen-Air Combustion Model in Turbulent Reacting Flow Calculations," *AIAA Journal*, Vol. 21, pp. 586–592.

Ruegg, F.W. and Dorsey, W., 1962, "A Missile Technique for the Study of Detonation Wave," *Journal of Research of the National Bureau of Standard, Section C: Engineering and Instrumentation*, Vol. 66, pp. 51–58.

Sagara, K. and Tsugé, S., 1970, "A Bimodal Maxwellian Distribution as the Equilibrium Solution of the Two-Particle Regime," *Physics of Fluids*, Vol. 25, pp. 1970–1977.

Shang, H.M., Chen, Y.S., Liaw, P., Chen, C.P. and Wang, T.S., 1995, "Investigation of Chemical Kinetics Integration Algorithms for Reacting Flows," AIAA Paper 95–0806.

Shuen, J.S., 1992, "Upwind Differencing and LU Factorization for Chemical Non-equilibrium Navier-Stokes Equations," *Journal of Computational Physics*, Vol. 99, pp. 233–250.

Shuen, J.S., Liou, M.S. and Van Leer, B., 1990, "Inviscid Flux-Splitting Algorithms for Real Gases with Non-equilibrium Chemistry," *Journal of Computational Physics*, Vol. 90, pp. 371–395.

Shuen, J.S. and Yoon, S., 1989, "Numerical Study of Chemically Reacting Flows Using a Lower-Upper Symmetric Successive Overrelaxation Scheme," *AIAA Journal*, Vol. 27, pp. 1752–1760.

Shyy, W., 1994, *Computational Modeling For Fluid Flow and Interfacial Transport*, Elsevier.

Shyy, W., Thakur, S. and Udaykumar, H.S., 1993, "A High Accuracy Sequential Solver for Simulation and Active Control of a Longitudinal Combustion Instability," *Computing Systems in Engineering*, pp. 27–41.

Slack, M. W., 1977, "Rate Coefficient for $H + O_2 + M = HO_2 + M$ Evaluated From Shock Tube Measurements of Induction Times," *Combustion and Flame*, Vol. 28, pp. 241–249.

Steger, J.L and Warming, R.F., 1981, "Flux-Vector Splitting of the Inviscid Gasdynamic Equations with Application to Finite Difference Methods," Journal of Computational Physics, Vol. 40, pp. 263–293.
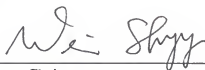
Stiefel, L., Editor, 1988, *Gun Propulsion Technology*, AIAA, Washington D.C.

Stull, D.R. and Prophet, H., 1971, "JANAF Thermochemical Tables," NSRDS–NBS 37.

Sussman, M.A., 1993, "Source Term Evaluation for Combustion Modeling," AIAA Paper 93–0239.

Sussman, M.A., 1994, "A Computational Study of Unsteady Shock-Induced Combustion of Hydrogen-Air Mixtures," AIAA Paper 94–3101.

Sussman, M.A. and Wilson, G.J., 1991, "Computation of Chemically Reacting Flow Using a Logarithmic Form of the Species Conservation Equations," *Proceedings of the 4th International Symposium on Computational Fluid Dynamics*, Vol. 1, pp. 1113–1118.

Tennekes, H. and Lumley, J.L., 1972, *A First Course in Turbulence*, Cambridge: MIT Press.

Thakur, S.S., Wright, J.F., Shyy, W., Liu, J., Ouyang, H. and Vu, T., 1996, "Development of Pressure-based Composite Multigrid Methods for Complex Fluid Flows," *Progress in Aerospace Sciences*, Vol. 32, pp. 313–375.

Warnatz, J., 1981, "Concentration-, Pressure-, and Temperature-Dependence of the Flame Velocity in Hydrogen-Oxygen-Nitrogen Mixtures," *Combustion Science and Technology*, Vol. 26, pp. 203–213.

Warnatz, J., 1984, "Rate Coefficients in the C/H/O System," *Combustion Chemistry*, edited by W.C. Gardiner, Jr., Springer-Verlag, New York, pp. 197–360.

White, F.M., 1974, *Viscous Fluid Flow*, McGraw-Hill, New York.

Wilcox, D.C., 1992, *Turbulence Modelling for CFD*, CDW Industries, Inc.

Wilson, G.J. and MacCormack, R.W., 1990, "Modeling Supersonic Combustion Using a Fully-Implicit Numerical Method," AIAA Paper 90–2307; see also 1992, *AIAA Journal*, Vol. 30, pp. 1008–1015.

Wilson, G.J. and Sussman, M.A., 1993, "Computation of Unsteady Shock-Induced Combustion Using Logarithmic Species Conservation Equations," *AIAA Journal*, Vol. 31, pp. 294–301.

Wolfram, S., 1988, *Mathematica : A System for Doing Mathematics by Computer*, Addison-Wesley, Redwood City, CA.

Yee, H.C., 1989, "A Class of High-Resolution Explicit and Implicit Shock-Capturing Methods," NASA TM 101088.

Yee, H.C. and Shinn, J.L., 1989, "Semi-Implicit and Fully Implicit Shock-Capturing Methods for Nonequilibrium Flows," *AIAA Journal*, Vol. 27, pp. 299–307.

Ying, S.X., 1986, *Three-Dimensional Implicit Approximately Factored Schemes for the Equations of Gasdynamics*, Ph. D Thesis, Stanford University.

Yousefian, V., 1982, "Muzzle Flash Onset," ARBRL–CR–00477.

Yungster, S., Eberhardt, S. and Bruckner, A.P., 1989, "Numerical Simulation of Hypervelocity Projectiles in Detonable Gases," AIAA Paper 89–0673; see also 1991, *AIAA Journal*, Vol. 29, pp. 187–199

Yungster, S. and Radhakrishnan, K., 1994, "A Fully Implicit Time Accurate Method for Hypersonic Combustion: Application to Shock-Induced Combustion Instability," NASA TM 106707; see also 1994, AIAA Paper 94–2965.

BIOGRAPHICAL SKETCH

Keith was born, July 5, 1966, along with his twin sister Sherry. After a childhood which consisted of brief stops in Maryland, Louisiana, Alabama, and somewhat longer stays in Florida and Mississippi, Keith obtained his B.S. and M.S. in Aerospace Engineering from Mississippi State University in 1988, and 1989 respectively. From 1990 to 1995, Keith served on active duty with the US Air Force at Eglin AFB, FL. During his tenure, he worked as a Program Manager on the AGM–130 Air–to–Surface Weapon and as a Project Engineer on various munition research projects. In 1995, Keith separated from the Air Force at the rank of Captain to pursue his Ph. D. in Aerospace Engineering at the University of Florida. Keith is married to Capt. Paula Clutter, USAF, and has two children, Courtney and Cooper.

I certify that I have read this study and that in my opinion it conforms to acceptable standards of scholarly presentation and is fully adequate, in scope and quality, as a dissertation for the degree of Doctor of Philosophy.

Wei Shyy, Chairperson
Professor of Aerospace Engineering,
    Mechanics and Engineering Science

I certify that I have read this study and that in my opinion it conforms to acceptable standards of scholarly presentation and is fully adequate, in scope and quality, as a dissertation for the degree of Doctor of Philosophy.
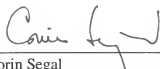
Dave Belk
Adjunct, Assistant Professor of Aerospace
    Engineering, Mechanics and Engineering
    Science

I certify that I have read this study and that in my opinion it conforms to acceptable standards of scholarly presentation and is fully adequate, in scope and quality, as a dissertation for the degree of Doctor of Philosophy.

Renwei Mei
Associate Professor of Aerospace Engineering,
    Mechanics and Engineering Science

I certify that I have read this study and that in my opinion it conforms to acceptable standards of scholarly presentation and is fully adequate, in scope and quality, as a dissertation for the degree of Doctor of Philosophy.

Corin Segal
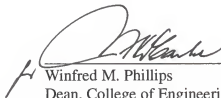Assistant Professor of Aerospace Engineering,
Mechanics and Engineering Science

I certify that I have read this study and that in my opinion it conforms to acceptable standards of scholarly presentation and is fully adequate, in scope and quality, as a dissertation for the degree of Doctor of Philosophy.

James Klausner
Associate Professor of Mechanical Engineering

This dissertation was submitted to the Graduate Faculty of the College of Engineering and to the Graduate School and was accepted as partial fulfillment of the requirements for the degree of Doctor of Philosophy.

May 1997

Winfred M. Phillips
Dean, College of Engineering

Karen A. Holbrook
Dean, Graduate School

LD
1780
1997
.C b 49 ?